LATTICE BOLTZMANN SIMULATION OF CELL ADHESION IN MICROCIRCULATION

YAN WEI-WEI

Ph. D.

THE HONG KONG POLYTECHNIC UNIVERSITY

2011

The Hong Kong Polytechnic University

Department of Mechanical Engineering

Lattice Boltzmann Simulation of Cell Adhesion in Microcirculation

by

YAN Wei-Wei

A thesis submitted in partial fulfilment of the requirements

for the Degree of Doctor of Philosophy

December 2010

Certificate of Originality

I hereby declare that this thesis is my own work and that, to the best of my knowledge and belief, it reproduces no material previously published or written, nor material that has been accepted for the award of any other degree or diploma, except where due acknowledgement has been made in the text.

_____ （Signed）

___YAN WEI WEI____ （Name of student）

Abstract

Cell adhesion under blood flow conditions is a common and very important phenomenon in microcirculation. In this thesis, the fluid dynamics was solved by the lattice Boltzmann method (LBM), the cells dynamics was implemented by the Newton's law of translation and rotation, and the adhesive dynamics models were involved to take into account the effect of receptor-ligand bonds on cell adhesion.

Firstly, the effects of vessel curvature and cell-cell interaction on cell adhesion in both the straight and curved micro-vessels were numerically studied. The results indicated that the curved vessels would increase the simultaneous bonds number, and the probability of cell adhesion is increased consequently. In addition, the cell-cell interactions would also affect the cell adhesion greatly. For two-cell case, the simultaneous bonds number of the rear cell is increased significantly in both the straight and curved vessels. The results would be helpful to explain the mechanical mechanism of the strange biological phenomena why the circulating blood cells and tumor cells are more easily gathering near the bent of vessels.

Secondly, the effects of wall shear stress/gradient on tumor cell adhesion in the curved micro-vessels were investigated both experimentally and numerically. Our in vivo experiments revealed that the tumor cells preferred to adhere to the curved vessels and initiated at the inner side of the curved vessels. In simulation cases, two refined adhesive dynamics models were developed to consider the effects of wall shear stress/gradient on receptor-ligand bindings. The numerical

results indicated that the wall shear stress/gradient, over a threshold, had significant contribution to tumor cell adhesion by activating or inactivating cell adhesion molecules. This work not only would help us to understand the quantitative relationship between wall shear stress and tumor cell adhesion, but also elucidate why the tumor cell adhesion always occurs at the inner side of the curved vessels.

Finally, the effects of divalent cations on neutrophil adhesion in both the straight and curved micro-vessels were computationally investigated. The LFA-1/ICAM-1 adhesion in Mg^{2+} plus EGTA and the VLA-4/VCAM-1 adhesion in Mg^{2+} plus EGTA, Mn^{2+} and Ca^{2+} were simulated under flow conditions. The results suggested that the LFA-1/ICAM-1 adhesion acted as a primary role in neutrophils adhesion. For VLA-4/VCAM-1 adhesion, it was found the affinity state of VLA-4 for endothelial ligand VCAM-1 was highest in Mn^{2+}, higher in Ca^{2+}, and lowest in Mg^{2+} plus EGTA. This would help us to understand the mechanical mechanisms of integrin-mediated neutrophils adhesion in the presence of different divalent cations under dynamic flow conditions.

Key Words: cell adhesion, lattice Boltzmann method, vessel curvature, cell-cell interaction, wall shear stress/gradient, divalent cations

Publications Arising from This Thesis

Weiwei Yan, Bin Cai, Yang Liu and Bingmei Fu. Effects of Wall Shear Stress and its Gradient on Cell Adhesion in Curved Micro-vessels, ***Biomechanics and Modeling in Mechanobiology***, (revision submitted)

Weiwei Yan, Yang Liu and Bingmei Fu. Effects of Curvature and Cell-Cell Interaction on Cell Adhesion in Microvessels, ***Biomechanics and Modeling in Mechanobiology***, vol. 9, no. 5, pp. 629-640 (2010)

Weiwei Yan, Yang Liu and Bingmei Fu. Effects of Divalent Cations on Cell Adhesion between Human Neutrophil and Endothelial Ligand VCAM-1: A Lattice Boltzmann Analysis, ***Procedia Computer Science***, vol. 4, no. 110, pp. 1039-1047 (2011)

Liu Yang, **Weiwei Yan** and Bingmei Fu. Mechanical Mechanism of Circadian Fluctuations Regulated Haematopoietic Stems Cell (HSC) Release, *ASME 2011 Summer Bioengineering Conference*, 22-25 June 2011, Pennsylvania USA (accepted)

Weiwei Yan, Yang Liu and Bingmei Fu. Effect of Wall Shear Stress Variation on Tumor Cell Adhesion, *15th Annual Conference (2010-2011) of HKSTAM* incorporating with *7th Jiangsu-Hong Kong Forum on Mechanics and Its Application* and *2nd Symposium on the Development of Mechanics in Macau*, pp. 6, 11-12 March 2011, Macau

Weiwei Yan, Yang Liu and Bingmei Fu. Wall Shear Stress Gradient Regulated Cell Adhesion in a Curved Microvessel: a Lattice Boltzmann Analysis, *2nd*

Annual International Conference on Computational and Systems Biology, pp. 22-23, 22-24 October 2010, HangZhou

Weiwei Yan, Yang Liu and Bingmei Fu. Effect of Shear Stress Gradient on Cell Adhesion in Curved Micro-vessels, *6th World Congress on Biomechanics*, pp. 470, 1-6 August 2010, Singapore

Weiwei Yan, Yang Liu and Bingmei Fu. Effect of Adhesive Dynamics Models on Cell Adhesion in a Straight Capillary Vessel–A LBM Study, *4th International Conference from Scientific Computing to Computational Engineering*, pp. 214-221, 7-10 July 2010, Athens, Greece

Weiwei Yan, Yang Liu and Bingmei Fu. Effect of Curvature and Cell-Cell Interaction on Cells Adhesion in Curved Micro-vessels, *14th Annual Conference (2009-2010) of HKSTAM* in conjunction with *7th Shanghai-Hong Kong Forum on Mechanics and Its Application*, pp. 38, 13 March 2010, Hong Kong

Weiwei Yan, Yang Liu and Bingmei Fu. Effect of Channel Curvature on Cell Adhesion in Micro-circulation, *World Congress on Bioengineering 2009*, pp. 229, 26-29 July 2009, Hong Kong

Li Huabing, **Weiwei Yan**, Yang Liu and Bingmei Fu. Lattice Boltzmann Simulations of Cells Moving in a Siphon, *World Congress on Bioengineering 2009*, pp. 228, 26-29 July 2009, Hong Kong

Acknowledgement

I am glad to announce that I have completed my Ph.D thesis here, and sincerely appreciate those who helped me in my academic life. First of all, I would like to acknowledge my academic supervisor, Dr. Y. Liu, for his great encouragement, continuous support, and invaluable guidance throughout my whole Ph.D study. Dr. Y. Liu is an excellent scholar, his precise manner and great perseverance in research set a good example for me and has a strong influence on my future career.

Secondly, I would like to acknowledge Prof. B.M. Fu, who is from the Department of Biomedical Engineering, The City College of the City University of New York, for her enthusiastic guidance and inspiring academic advice. She actually acts as a role of my second academic supervisor.

I would like to thank Prof. Y.S. Xu for his encouragement and support. He helps me to face the difficulties optimistically.

I would like to thank Dr. H.B. Li for his helpful discussion in lattice Boltzamnn simulation.

I would like to thank all of my friends for their warm friendship.

I am thankful to my parents and my brother for their endless love.

Finally, the financial support given by the Hong Kong Polytechnic University through a Research Scholarship to me is gratefully acknowledged.

Table of Content

List of Tables

List of Figures

Chapter 1 Introduction to Cell Adhesion

Cell adhesion under blood flow conditions is a very common and important phenomenon in the microcirculation, such as leukocytes adhesion for the immune functions, platelets adhesion for the wound-healing functions, and tumor cells adhesion during cancer metastasis. Cell adhesion is also a fascinating process in many biological systems. Firstly, it plays a pivotal role in many situations of biological and medical interest. Secondly, it is likely the best cell function to be considered for biophysical modeling from the micrometer down to the molecular level. Thirdly, studying the biophysical aspects of cell adhesion leads to face many important problems of physics, physical chemistry and cell physiology. Therefore, it is of significant importance to study the mechanical mechanisms of cell adhesion under hydrodynamic conditions. In this chapter, the backgrounds of leukocytes adhesion, neutrophils adhesion and tumor cells adhesion in the microcirculation are introduced in detail. Besides, the objectives and the organization of the present thesis are also arranged in this chapter.

1.1 Leukocytes Adhesion

The leukocytes (also known as the white blood cells) are the cells of immune system which defend the body against both infectious disease and foreign materials. They are usually made by bone marrow and found throughout the body, including the blood system and lymphatic system. The appearance of a leukocyte is shown in Fig. 1.1. Normally, the leukocytes circulate in the blood vessel

unattached. But if the body is suffered a disease, the inflammatory stimuli will trigger the leukocytes to move into tissue towards the foreign invader. This process is very interesting and really complex.

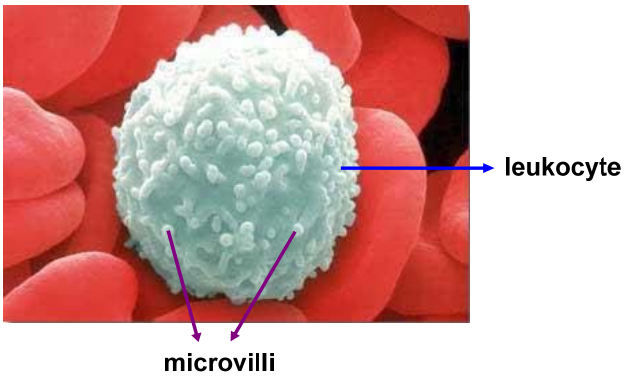

Figure 1.1 Appearance of the leukocyte

(http://healthinfoispower.files.wordpress.com/2008/07/leukocyte1.jpg)

It has been reported that leukocytes adhesion to the surface of endothelial cells (ECs) plays a crucial role in the inflammatory response (King and Hammer 2001a). This process has been intensively studied and referred to as the leukocyte adhesion cascade (Butcher 1991; Springer 1994). Figure 1.2 shows the schematic view of leukocyte adhesion cascade. It is a sequence of adhesion and activation events that ends with the extravasation of leukocyte into tissue, whereby the leukocyte exerts its effects on the inflamed sites. At least five steps are involved in this immune response, which has been defined as capture, rolling, slow rolling, firm adhesion and transmigration. Each of these steps appears to be necessary for the effective leukocyte recruitment, because blocking any of the steps can severely reduce leukocyte accumulation in the inflamed tissues. These five steps are not phases of inflammation, but represent the sequence of events from the

perspective of each leukocyte. At any given moment, these five steps all happen in parallel, involving different leukocytes in the same micro-vessels.

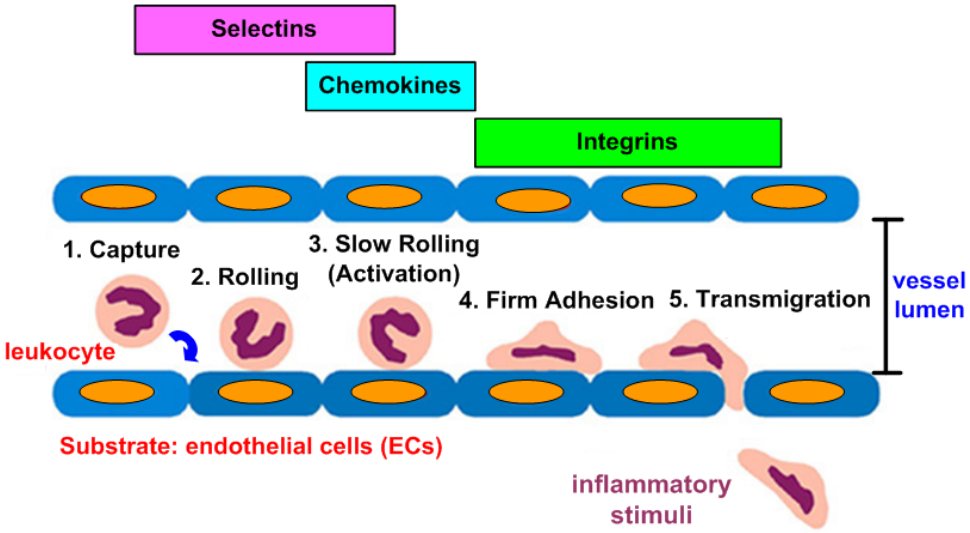

Figure 1.2 Leukocyte adhesion cascade

(http://www.mpi-muenster.mpg.de/nvz/wilde.shtml)

Leukocytes adhesion is primary caused by the strong interactions between leukocytes and ECs. Figure 1.3 shows the structure of ECs. An individual EC has a central nucleus, and it is very flat. A large number of ECs make up the lining of blood vessels. The intercellular junctions between ECs overlap helps to make a tight seal in the vessel wall. Recently, significant advances have been made in cell adhesion, with which a major conceptual development is the recognition that cell adhesion is often mediated via a surprisingly small number of receptor-ligand bonds (Zhu et al. 2000). The receptors and ligands are various cell adhesion molecules on the tips of microvilli that located on the surfaces of ECs and leukocytes. Usually, the adhesion molecules on the ECs surface play roles as ligands and these on the leukocyte surface act as receptors. The strong interactions

between receptors and ligands provide a chance to form receptor-ligand bonds by a stochastic process. The formed bonds enable the leukocyte to overcome the shear forces of the surrounding blood and firmly adhere to the ECs surface.

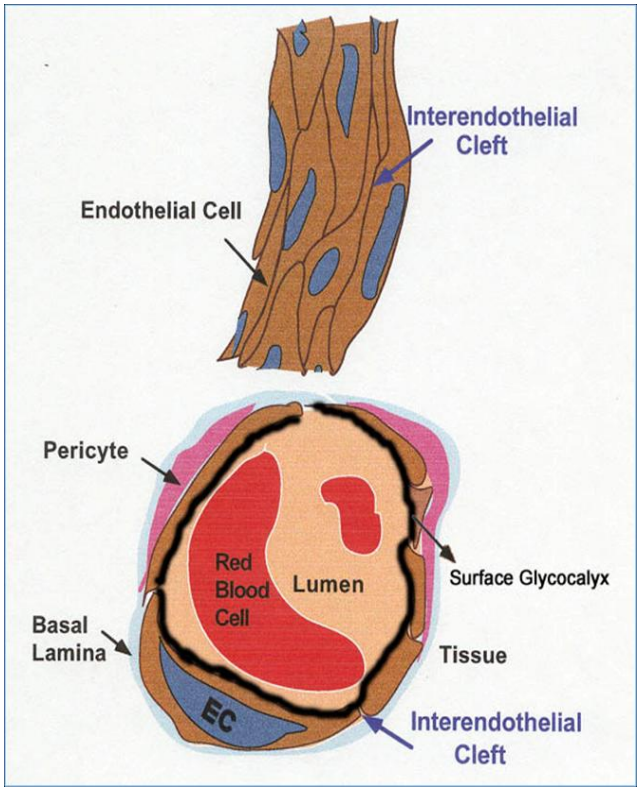

Figure 1.3 Structure of the endothelial cells

(Fu B.M., "Micro-vessel permeability", Encyclopedia of Biomedical Engineering, Editor: Metin Akay, Wiley-Interscience, 2006, ISBN0-471-24967-X)

Leukocyte adhesion is mediated by different adhesion molecules. The types of adhesion molecules and their functioning range have been sketched in Fig. 1.2. Firstly, the leukocyte is captured to the blood vessel wall and rolling on the activated endothelium by selectins. The selectins are thought to serve at least two purposes, one being to reduce the velocity of leukocyte, and the second to bring leukocyte and ECs into close proximity to allow for chemical mediators to be

picked up by the leukocyte. Secondly, the chemical mediators that called 'chemokines' on the ECs surface lead to the activation of leukocytes and leukocyte integrins. Finally, the leukocyte integrins bind tightly with their endothelial ligands, whereby the leukocyte migrates through the EC layer and basal lamina to reach the underlying tissue.

Up to date, many in vitro experimental studies have been performed on leukocyte adhesion by using dilute cell suspension in flow chambers formed by two parallel plates (King and Hammer 2001b). These experiments identified that the adhesion molecules on the leukocytes and endothelium govern leukocytes adhesion and migration under flow conditions. Dong et al. (1999) investigated the mechanics of leukocyte deformation and adhesion to the ECs in shear flow by in vivo measurement and a 2-D model which consists of an elastic ring adhered to a surface under fluid stresses. Several computational studies of leukocyte adhesion and erythrocyte-leukocyte interactions have also been implemented. Migliorini et al. (2002) quantified the forces that exerted on rolling leukocyte by flowing erythrocytes, they reported that the erythrocytes would augment leukocyte binding in a virtual blood vessel. Sun et al. (2003) & Sun and Munn (2006) analyzed the interactions of erythrocytes and leukocytes as the cells all flowed from a capillary into a post-capillary venule by a lattice Boltzmann approach. Caputo and Hammer (2005) explored the effect of microvillus deformability on leukocyte adhesion by using the adhesive dynamics simulations and found four leukocyte adhesion states, such as no adhesion, rolling, landing and firm adhesion. Most of the

previous researches on leukocyte adhesion were carried out in the straight chambers or micro-vessels due to the simplicity in these situations. Despite significant studies have been carried out in leukocytes adhesion, the precise mechanical mechanism by which cells are recruited into adhesive interactions with the blood vessel wall is not yet well understood, owing to the complexities of blood dynamics, micro-vessel structures, and cell-surface interactions involved.

1.2 Neutrophils Adhesion

Neutrophils are the most common and abundant type of leukocytes in humans, comprising about 50-70% of all the leukocytes. They are the first immune cells to arrive at a site of infection and form an essential part of the innate immune system. The mature neutrophil has a segmented nucleus while the immature neutrophil has band-shape nucleus, as shown in Fig. 1.4. Neutrophils are the main component of pus and responsible for its whitish color. They are present in the bloodstream until signaled to a site of infection by chemical cues in the body. Usually, they mediate the inflammatory response by phagocytosing pathogens like bacteria.

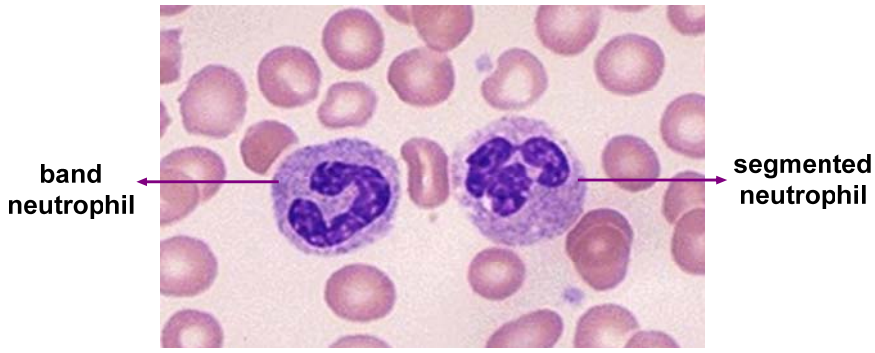

Figure 1.4 Immature neutrophil (left) and mature neutrophil (right).
(http://www.nku.edu/~dempseyd/BLOOD_GOOD.jpg)

Neutrophils adhesion to the ECs surfaces is a crucial, regulated step in the body's response to infection. This interaction is primary mediated concomitantly or sequentially by the adhesion molecules in the integrins family. There are many types of integrin and many cells have multiple types of integrins. The integrins are of vital importance to all animals and have been found in all animals, from sponges to mammals. They are obligate heterodimers containing two distinct chains called α and β subunits, which have been extensively studied and characterized as eighteen α and eight β subunits in humans (Lawrence et al. 1990; Darrell 2005). Figure 1.5 shows the integrin subunits and their heterodimeric pairings in humans. The integrins form several subfamilies sharing common β subunits that associate with different α subunits. α and β subunits each contain two separate tails, both of which penetrate the plasma membrane and possess small cytoplasmic domains.

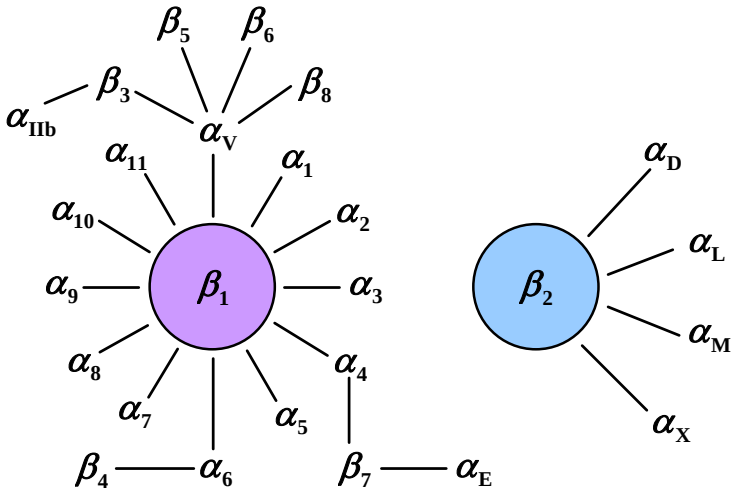

Figure 1.5 Eighteen α and eight β integrin subunits and their heterodimeric pairings in humans

The integrin-mediated neutrophils adhesion has been proved to play a significant role in embryonic development, inflammation, thrombosis, and cancer metastasis (Ruoslahti et al. 1994). To date, most studies of neutrophils adhesion have focused on the β_2 integrins family (Lawrence et al. 1990; Lum et al. 2002), because this subgroup of integrins is exclusively expressed on the neutrophils surface. An important member of the β_2 integrins family is the leukocyte function-associated antigen-1 (LFA-1, $\alpha_L\beta_2$), whose principal endothelial ligands are the intercellular cell adhesion molecules-1 (ICAM-1). The interactions between LFA-1 and ICAM-1 are of great interest in the studies of neutrophils adhesion.

In recent years, the role that members in the β_1 integrins family play in neutrophils adhesion has also received great attention (Osborn et al. 1989; Rice and Bevilacqua 1989). The most important member of the β_1 integrins family on the neutrophils surface is the very late antigen-4 (VLA-4, $\alpha_4\beta_1$), whose principal counter-receptor is the vascular cell adhesion molecule-1 (VCAM-1). VLA-4 binds to VCAM-1 and is chiefly responsible for lymphocyte and monocyte adhesions to vascular endothelium as well as neutrophils recruitment to the inflamed tissue sites (Luscinskas et al. 1994; Alon et al. 1995; Darrell 2005). However, the role of VLA-4/VCAM-1 bonds in mediating neutrophils adhesion under blood flow conditions has not been clearly understood, although there is obvious evidence that these bonds can regulate neutrophils adhesion to endothelium in the microcirculation (Reinhardt et al. 1997; Reinhardt and Kubes 1998).

An important step for integrin-mediated neutrophils adhesion is the activation of integrins to their high affinity for their endothelial ligands (Lollo et al. 1993; Woodside et al. 2001). In the natural state, this integrins activation is caused by the intracellular signaling events in response to inflammatory stimuli (Hogg et al. 1993). The integrins contain binding sites for different divalent cations, which are necessary for their adhesive functions. It has been reported that the affinity conformation of many integrins can be influenced by different divalent cations in extracelluar medium (Masumoto and Hemler 1993; Bazzoni et al. 1998). This feature provides an opportunity to explore the particular importance of integrins activation for neutrophils adhesion in the absence of general activation of the cells (Lomakina and Waugh 2004).

The response to divalent cations is different among integrins. It has been reported that Mg^{2+} plus calcium chelator EGTA induces a high affinity of LFA-1 for ICAM-1, but this effect is inhibited by the presence of millimolar Ca^{2+} (Dransfield et al. 1992; Labadia et al. 1998). The effect on the affinity state of Mac-1 is also different from that of LFA-1, although they are in the same β_2 integrin family. For examples, Mg^{2+} plus EGTA causes the activation of LFA-1, but it has little effect on Mac-1 ($\alpha_M\beta_2$). On the contrary, Mn^{2+} induces the higher affinity form of Mac-1 than that of LFA-1 (Altieri 1991; Diamond and Springer 1993). In the β_1 integrin-mediated adhesion, it has been reported that the affinity conformation of VLA-4 to VCAM-1 is higher in Mg^{2+} than that in Ca^{2+}, and highest in Mn^{2+} (Chigaev et al. 2003; Lomakina and Waugh 2009). In contrast,

VLA-4 is thought to be unique in the β_1 integrins family in which is active in the presence of Ca^{2+} (Bazzoni et al. 1998) and initiates neutrophils adhesion under physiological conditions without further activation (Yednock et al. 1995).

While aforementioned studies have led to a better understanding of neutrophils adhesion, our understanding is still poor for the roles of LFA-1/ICAM-1 and VLA-4/VCAM-1 bindings in mediating neutrophils adhesion. Therefore, the contribution of LFA-1/ICAM-1 adhesion and VLA-4/VCAM-1 bonds to the neutrophils adhesion in different divalent cations under flow conditions is one of the topics of discussion in this thesis.

1.3 Tumor Cells Adhesion

Cancer is the second leading cause of death in the world, exceeded only by the heart disease. Currently, more than 7 million people now die each year from cancer. The main reason that cancer is difficult to cure is its ability to metastasize to another part of body from where it starts. Indeed, metastasis represents the most significant and elaborate hurdle to overcome in the search for a cure for cancer.

Cancer cells initially group together to form a primary tumor. Once the tumor is formed, the cells may begin to break off from this tumor and invade either the circulatory or the lymph system, which will carry them to a new location, and establish themselves in the new sites. This is a very complicated process by which still has not been completely understood.

A common way for tumor cells metastasis is the bloodstream, since blood vessels are often nearby. Figure 1.6 shows the process of cancer metastasis in the

blood vessel. When the cancer cell spreads through the bloodstream, it first becomes detached from the primary tumor, and then it burrows through the wall of blood vessel to get into the bloodstream. This is the first step called as "intravasation". Once the tumor cell arrives in the bloodstream, it will be swept along by the circulating blood until they get stuck somewhere, usually in a very small blood vessel called a capillary or micro-vessel. This cell adhesion step is realized by the interactions of adhesion molecules on the surfaces of tumor cell and ECs. The interactions between adhesion molecules will accordingly increase the permeability of endothelium, and therefore the tumor cell will burrow through the wall of blood vessel and get into the tissue of the organ where they find themselves in. There they start to multiply to grow a new tumor.

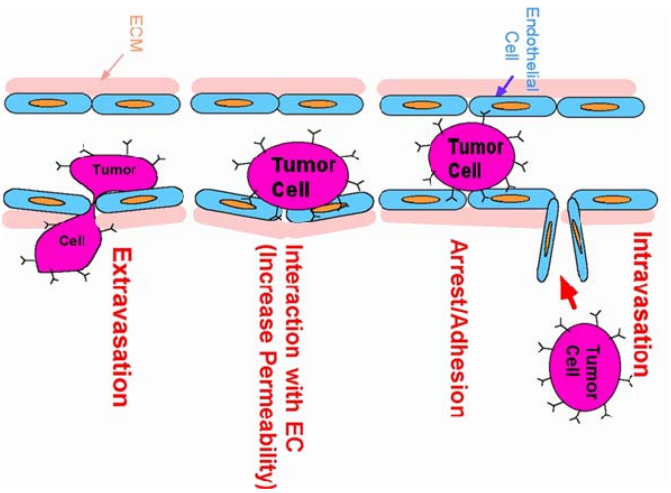

Figure 1.6 The process of cancer metastasis in the blood vessel.
(Unpublished picture, personal communication with Prof. Fu B.M. at the City University of New York)

Generally speaking, the majority of circulating cancer cells delivered to various target organs are trapped and rapidly damaged in the microvasculature,

resulting in cells death and “metastatic inefficiency” (Weiss 1990). It was found that fewer than 1 in 10,000 cancer cells could survive circulation to create a new tumor. To survive the circulating tumor cells must adhere to the vessel walls of distant host organs, and eventually penetrate the vascular wall to avoid blood shear forces and host defense mechanisms.

Tumor cells adhesion to the surfaces of ECs under flow conditions plays a pivotal role in cancer metastasis (Pauli et al. 1990; Rice and Bevilacqua 1989; Hammer and Apte 1992). Many researches have been executed to study tumor cells adhesion under flow conditions. Dong et al. (2005) studied human melanoma cell adhesion and migration under dynamic flow conditions by using a modified Boyden chamber. Haier and Nicolson (2001) reviewed the tumor cell adhesion under conditions of fluid flow, and indicated that tumor cell adhesion to the microvasculature was a complex process involving various types of cell adhesion molecules. Compared to leukocytes adhesion, it is difficult to observe tumor cells adhesion in a straight chamber. However, a recent in vivo study has indicated that the tumor cells would aggregate near the bend of micro-vessels (Lv et al. 2007).

Figure 1.7 shows the experimental observations of tumor cells adhesion in different curvature of micro-vessels. They are in vivo experimental results that used with the permission of Prof. Fu B.M., who is our experimental collaborator from the Department of Biomedical Engineering, The City University of New York. The experiments were performed on rat mesentery that infected by cancer. From Fig. 1.7, we can find that tumor cell adhesion is greatly influenced by the

vessel curvature. At the low curvature sites, one can hardly observes tumor cells accumulation. However, with the increase of vessel curvature, more tumor cells are found at the curved segments. Therefore, we can conclude that tumor cells are easier to be arrested by the curved micro-vessels than the straight ones. The experimental results are clear, but the precise behavior and mechanical mechanism of this phenomenon are not yet completed understood.

In addition to tumor cells, the similar phenomenon has been found for the circulating blood cells in the curved micro-vessels, which is shown in Fig. 1.8. The in vivo experimental results were also used with the permission of Prof. Fu B.M. Figs. 1.8(A)-(C) are the experimental observations for thrombosis of circulating blood cells in the non-injured but curved/stretched micro-vessels of rat mesentery. Figures on the top were images taken in the experiments, and the ones on the bottom were the corresponding sketches. Figure 1.8 (A) shows the vessel was bent/stretched by a restraining glass micropipette (pointed by the arrow) in the nearby tissue at t = 0, Fig. 1.8 (B) shows the circulating blood cells accumulated at two positive curvature sites at about t = 3 min, and Fig. 1.8 (C) illustrates the vessel was completely blocked by the blood cells at about t = 10 min. It was found that the thrombi were formed more than 30% (19 out of 61) at the bent sites. More interestingly, nearly all the thrombi were initiated from the positive curvature segments. Nevertheless, the precise behavior and mechanical mechanism of this strange phenomenon is either not clearly understood yet.

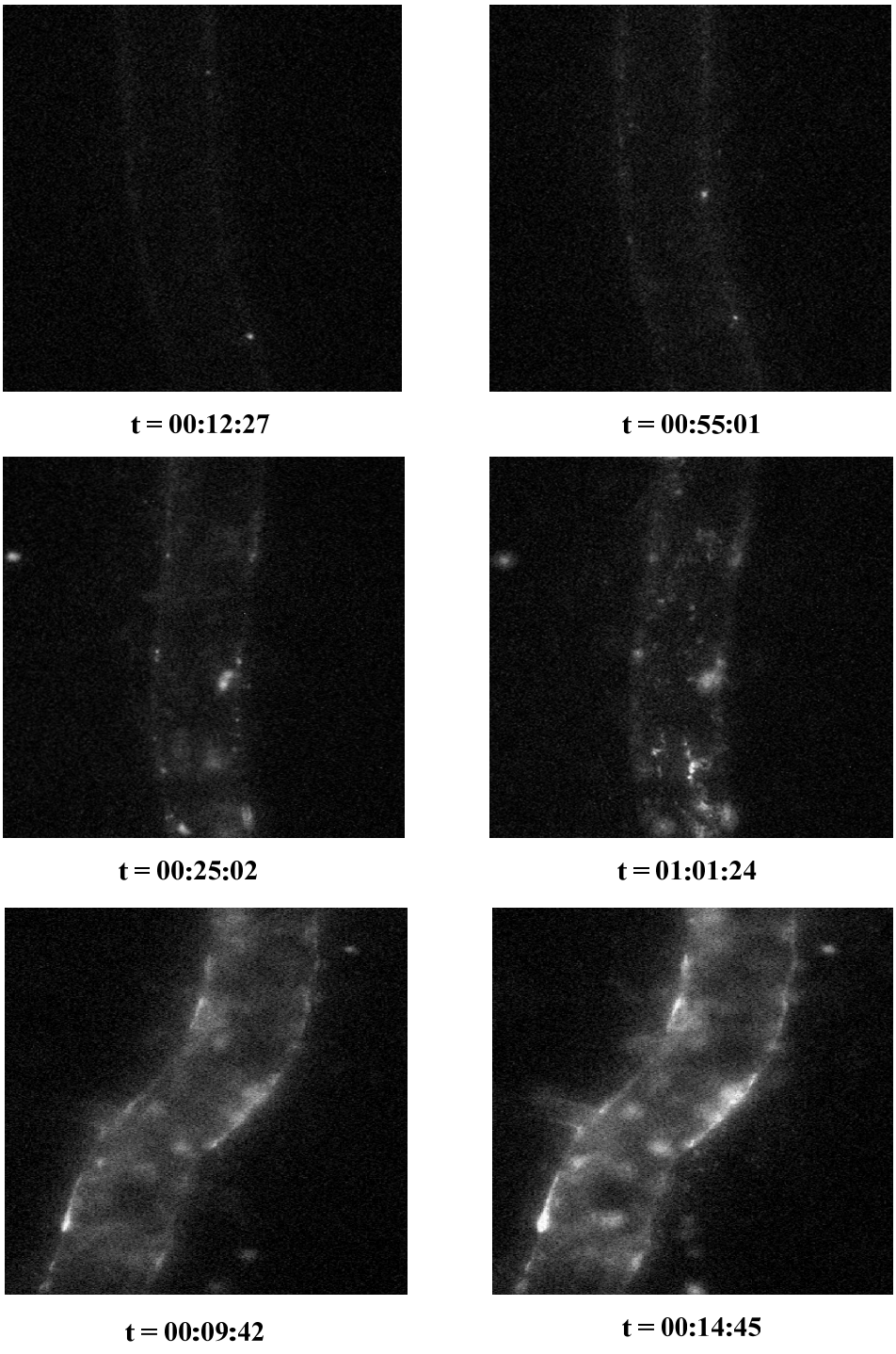

Figure 1.7 Tumor cells adhesion in different curvature micro-vessels.

(Shen et al. 2010, "Vascular endothelial growth factor enhances mammary cancer cell adhesion to endothelium in vivo", J. Exp. Physiology, 95, 369-379)

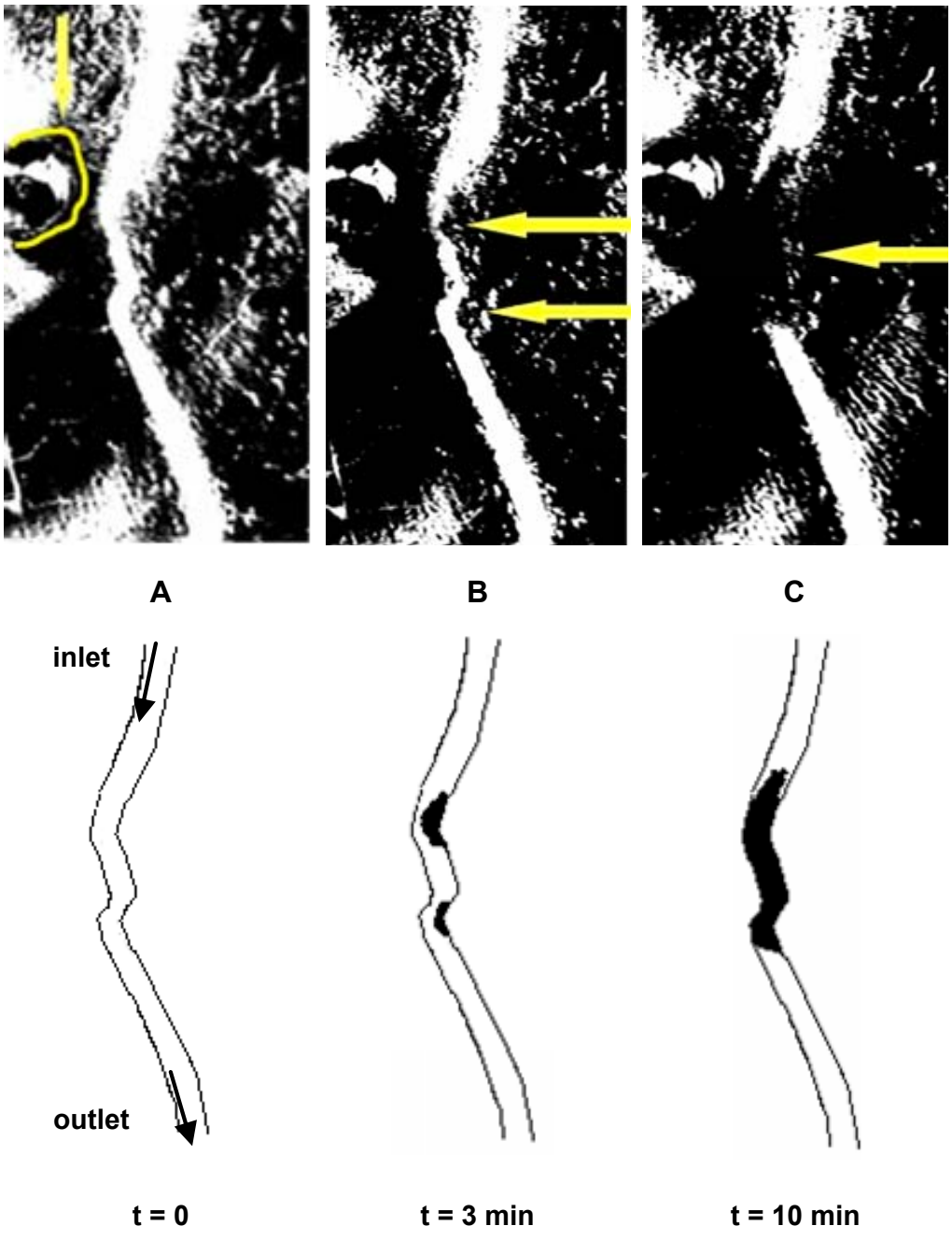

Figure 1.8 Circulating blood cells adhesion in the curved micro-vessels. (Liu et al. 2008, "Mechanical mechanisms of thrombosis in bent micro-vessels of rat mesentery", J. Biomech., 41, 12, 2726-2734)

From the above discussions, one can find that cell adhesion for both the blood cells and tumor cells in the curved micro-vessels is different from that in the straight ones. However, almost all the capillaries/micro-vessels are bent in the real physiological situations. Therefore, it is of great importance to explore the mechanical mechanisms of cell adhesion in the curved micro-vessels. A comprehensive biophysical description of cell adhesion in the microcirculation may eventually provide a rational basis for the development of novel therapeutic strategies for many diseases, such as thrombosis, arthritis, atherosclerosis, and cancer.

1.4 Objectives of This Thesis

Cell adhesion to the surface of ECs has been proved to play a vital role in many biological systems. It is a fascinating biological process and has been received great attention by the researchers. Although previous studies have led to a better understanding of cell adhesion, our knowledge is still limited for the mechanical mechanism of cell adhesion in the curved micro-vessels, such as why the circulating blood cells and tumor cells are prone to be arrested by the curved vessels than the straight ones; what is the quantitative relationship between wall shear stresses and cell adhesion in the curved vessels; and how do the divalent cations affect the affinity conformation of integrins for their endothelial ligands under blood flow conditions in neutrophils adhesion.

Simulation that can explain cell adhesion under complex flow conditions in microcirculation would be of great help in understanding the mechanical

mechanism of these strange biological phenomena. Lattice Boltzmann method (LBM) has been a promising tool to effectively connect macroscopic and microscopic scales, and thereby suitable to solve these multi-scale simulations. The primary objectives of the present thesis research are:

(1) To develop a numerical scheme that is capable of simulating cell adhesion in the complex micro-vessels.

(2) To numerically study the effects of vessel curvature and cell-cell interaction on cell adhesion in both the straight and curved micro-vessels.

(3) To computationally investigate the effects of vessel wall shear stress and its gradient on tumor cell adhesion in the curved micro-vessels.

(4) To numerically study the effects of different divalent cations on neutrophils adhesion in both the straight and curved micro-vessels.

1.5 Organization of This Thesis

The present thesis is organized in the following manner. Chapter 2 introduces the mathematical models of cell adhesion, including three adhesive dynamics models of reaction rates law for receptor-ligand bonds and a stochastic Monte Carlo approach for determining the adhesive bindings. The theory of LBM, which is used to solve the fluid dynamics, is discussed in Chapter 3. In this chapter, the Navier-Stokes equations, the lattice Boltzmann equation, the derivation of lattice Boltzmann equation from the Boltzmann equation, the recovery of Navier-Stokes equations from the lattice Boltzmann equation, and three boundary condition treatments in LBM are all included. Chapter 4 mainly evaluates three forces (i.e.

hydrodynamic force, repulsive van der Waals force, and spring force) that govern cell adhesion and migration under flow conditions. Then, the cell dynamics and the dimensional transformation between real physical quantities and lattice quantities are also presented. In Chapter 5, the effects of vessel curvature and cell-cell interaction on cell adhesion with one cell and double cells in either the straight or curved micro-vessels are discussed in detail. The effect of wall shear stress and its gradient on tumor cell adhesion in the curved micro-vessels is elaborated in Chapter 6. In this chapter, we develop two novel adhesive dynamics models that coupled the effects of wall shear stress and its gradient on tumor cell adhesion in the curved micro-vessels. Both the cases of the cell that released near the upper and bottom walls are detailedly discussed. Chapter 7 presents the effects of three different divalent cations on cell adhesion between human neutrophil and endothelial ligand VCAM-1. Mainly, the LFA-1/ICAM-1 adhesion in the presence of Mg^{2+} plus EGTA and VLA-4/VCAM-1 adhesion under the effects of Mg^{2+} plus EGTA, Ca^{2+}, and Mn^{2+} are analyzed. Chapter 8 summaries the contributions of this thesis with the recommendations for the future work.

Chapter 2 Mathematical Models of Cell Adhesion

Mathematical modeling of cell adhesion provides a powerful tool to quantify experimental observations and to integrate them into a unified sequence of cell adhesion events. Using basic physical, biological, and chemical principles, the mathematical expressions of cell adhesion are derived. These models not only help to include some hypotheses suggested by experimental observations, but also to gain insights about the mechanisms of cell adhesion being investigated. Once the model has been properly validated, it can be used to extrapolate parameters that cannot be measured, and predict the behavior of the system under different physiological conditions, and can even lead to the design of other useful experiments (Agresar 1996). In this chapter, the mathematical models of cell adhesion, including three adhesive dynamics models of the reaction rates law for adhesive receptor-ligand bonds and a stochastic Monte Carlo approach for determining the adhesive bindings, are presented in detail.

2.1 Adhesive Dynamics Models

Mathematical models of cell adhesion were generated from the conceptual developments and experimental improvements in cell adhesion. Up to date, significant advances have been made in cell adhesion, with which a major conceptual development is the recognition that cell adhesion is often mediated via a surprisingly small number of receptor-ligand bonds (Zhu et al. 2000). Many experimental improvements in cell adhesion have been established. It was found

that, when the moving cells interact with a stationary surface in the flow chamber, the cell velocities are highly fluctuated and the cell motions experience “stop-and-go” jerky type (Kaplanski et al. 1993; Alon et al. 1995). Weiss (1992) indicated that successful cell arrest was dependent on the balance between adhesive and anti-adhesive forces as well as the rate at which adhesive interactions were broken. Zhu (2000) and Zhu et al. (2000) presented a detailed review of the progress in the experimental methods that enabled quantification of the relevant kinetic and mechanical parameters, the fundamental concepts that underlaid the physics of the biological phenomena, and the mathematical models that related functions to the intrinsic properties of cell adhesion molecules. Experimental work at the nanoscale level to determine the lifetime, interaction distance and strain responses of adhesion receptor-ligand bonds has been spurred by the advent of atomic force microscopy and biomolecular force probes (Marshall et al. 2003), although our current knowledge in this area is far from complete. Marshall et al. (2005) studied the force history dependence of receptor-ligand dissociation using atomic force microscopy that provided a new paradigm for understanding how force regulated receptor-ligand interactions. By measuring the change in thermal fluctuations of the atomic force microscope cantilever tip, Marshall et al. (2006) demonstrated the new measurement method of the molecular elasticity.

The extensive studies on biophysical experiments of cell adhesion have led to the development of a number of mathematical models. The construction and application of these models have demonstrated that it is possible to analyze certain

cellular processes by highly quantitative approaches (Zhu et al. 2000). Up to date, many mathematical models have been proposed to describe different important events in cell adhesion. Hammer and Apte (1992) firstly proposed a mathematical model to simulate the interaction of a single cell with a ligand-coated surface under flow condition. This model can simulate the effect of many parameters on cell adhesion, such as the number of receptors on microvilli tips, the density of ligand, the rates of reaction between receptor and ligand, the stiffness of receptor-ligand springs, the response of springs to strain, and the magnitude of the bulk hydrodynamic stresses. The model can successfully recreate the entire range of expected and observed adhesive phenomena, from completely unencumbered motion, to rolling, to transient attachment, to firm adhesion. Moreover, this model can generate meaningful statistical measures of adhesion, including the mean and variance in velocity, rate constants for cell attachment and detachment, and the frequency of adhesion. King and Hammer (2001a) used the completed double-layer boundary integral equation method to study the adhesive interactions between multiple rigid particles and a planar boundary in a viscous fluid. The simulation results revealed a mechanism for the capture of free-stream cells once an initial cell has adhered to provide a nucleation site. Wang et al. (2006) developed a population balance model for cell aggregation and adhesion process in a non-uniform shear flow and carried out Monte Carlo simulation based on the model for the heterotypic cell-cell collision and adhesion to a substrate under dynamic shear forces. Shao and Xu (2007) numerically studied the adhesion

between a microvillus-bearing cell and a ligand-coated substrate by using Monte Carlo method. They found that most of the adhesion was mediated by a single bond if the total adhesion frequency was less than 20%.

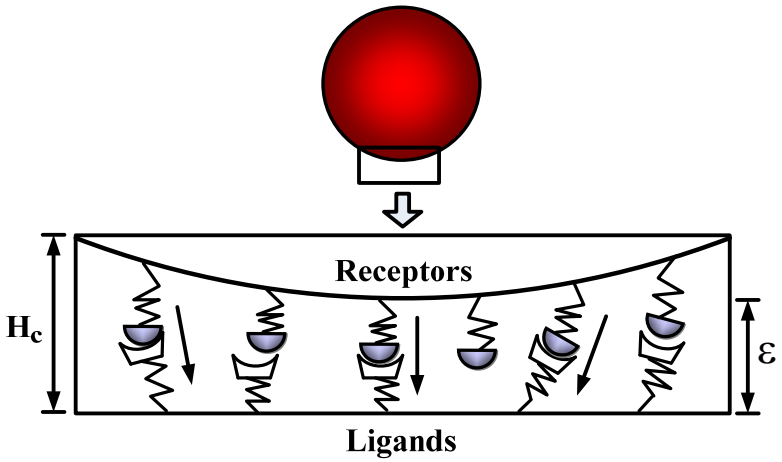

Figure 2.1 Adhesive dynamics model

Mathematical models of cell adhesion relate the forward and reverse reaction rates for receptor-ligand bonds. These reaction rates laws have been defined as 'adhesive dynamics models', which can be used to couple the effect of receptor-ligand bonds on cell adhesion. Fig. 2.1 shows the schematic view of adhesive dynamics model for the cell. In this model, the cell adhesion molecules on the surface of circulating cell are defined as receptors, and these on the surface of ECs are defined as ligands. Once the distance between a receptor and a ligand is smaller than a critical length H_c, it has the chance to form receptor-ligand bonds. Interactions between receptors and ligands are realized by the ideal adhesive springs, and the spring forces are calculated via the compression or expansion of these springs. This dynamic process relates the bond association and dissociation rate of adhesive dynamics models. In the next sections, three typical adhesive dynamics models will be discussed among various models.

2.1.1 Bell's Model

It is intuitively expected that the receptor-ligand bonds are usually subjected to a dislodging force that tends to alter the rate of dissociation. A variety of reverse reaction rate laws are available to characterize the coupling of applied force and bond dissociation. Among them, a seminal work was done by Bell (1978), which was validated to be a good approximation for different states of cell adhesion in the straight micro-vessels, such as no adhesion, rolling, landing, and firm adhesion (Caputo and Hammer 2005).

Generally speaking, the association rate of the bond is 84 s^{-1}, which is a reasonable value that extensive simulations have shown can properly recreate experimental values for velocity and dynamics of rolling in the straight micro-vessels (Chang et al. 2000). As to the bond dissociation rate, Bell (1978) adapted the kinetic theory of the strength of solids and proposed a constitutive relation between dissociation rate and force. Therefore, the bond association rate k_f and bond dissociation rate k_r can be expressed as,

$$k_f = 84 \tag{2.1}$$

$$k_r = k_r^0 \exp\left(\frac{\gamma f}{k_b T}\right) \tag{2.2}$$

where k_b is the Boltzmann constant, T the is temperature, k_r^0 is the unstressed dissociation rate, γ is the reactive compliance that describes the degree to which force facilitates bond breakage, both k_r^0 and γ are the functional properties of cell adhesion molecules. f is the spring force of each bond which can be obtained according to the Hooke's law:

$$f = \sigma(\chi - \lambda) \tag{2.3}$$

where σ is the spring constant, χ is the distance between the end points of receptor and ligand, and λ is the equilibrium bond length.

2.1.2 Dembo et al.'s Model

Dembo et al. (1988) modeled a piece of membrane with immobile discrete bonds and allowed the membrane to detach. They did this by letting the applied tension exceed the bond stress. This model can be used to predict the critical membrane tension required for detachment, and the resulting peeling velocities of the membrane. The main contribution of the model is the expression for the rate constants as a function of distance between the membranes. Dembo et al. (1988) demonstrated the reasonable, thermodynamically consistent rate expressions relating the bond association rate k_f and bond dissociation rate k_r to χ as,

$$k_f = k_f^0 \exp\left(-\frac{\sigma_{ts}(\chi - \lambda)^2}{2k_b T} \right) \tag{2.4}$$

$$k_r = k_r^0 \exp\left(-\frac{(\sigma - \sigma_{ts})(\chi - \lambda)^2}{2k_b T} \right) \tag{2.5}$$

where k_f^0 and k_r^0 are the reaction rate constants when the spring is at its equilibrium length, and σ and σ_{ts} is the spring constant and "transition state" spring constant, respectively.

Once the forward/reverse association rates of the bond are known, the appropriate expressions for the probability of formation and breakage of the bond tethers in a time step *dt* can be obtained by (Chang and Hammer 1996),

$$P_f = 1 - \exp\left(-k_f \cdot dt\right) \tag{2.6}$$

$$P_r = 1 - \exp\left(-k_r \cdot dt\right) \tag{2.7}$$

where P_f is the probability of forming a bond, and P_r is the probability of breaking a bond in a time interval *dt*.

2.1.3 Waugh and Lomakina's Model

In neutrophil adhesion, the chemical reaction between LFA-1 and ICAM-1 involves a single step reversible reaction of receptors binding to ligands (Chesla et al. 1998; Lomakina and Waugh 2004). Therefore, forming or breaking a LFA-1/ICAM-1 bond is the same as the general models, such as the Bell's model and the Dembo et al.'s model. As to the VLA-4/VCAM-1 adhesion, there exist two steps leading to the formation of bonds (Waugh and Lomakina 2009; Lomakina and Waugh 2009). The first step involves the formation of a reaction zone, and the second step is the binding reaction itself. The chemical reaction process for VLA-4/VCAM-1 adhesion is much more complex than that of the general models. The adhesive dynamics model for VLA-4/VCAM-1 adhesion and the chemical reaction equations for both the LFA-1/ICAM-1 and VLA-4/VCAM-1 adhesions are displayed in Fig. 2.2.

The novel adhesive dynamics model involves three zones: potential reaction zone (PRZ), reaction zone (RZ), and bonded zone (ZB). The RZ is defined to be a region where the neutrophil membrane is in proximity to the substrate and contain an unbound VLA-4 in its high affinity state. The ZB is defined as a region when

the VLA-4 binds to its ligand VCAM-1 on the substrate. The PRZ is thought to be not forming bonds but can become RZ by one or a combination of three mechanisms which are also illustrated in Fig. 2.2. Figure 2.2 (a) shows a region containing a high affinity that is not in close contact can move into close contact, Fig. 2.2 (b) shows an integrin in close contact which is in a low affinity state can undergo a conformational change to a high affinity state, and Fig. 2.2 (c) indicates an integrin in the high affinity state can diffuse into a region of close contact that does not initially contain one. This novel model does not distinguish between these different mechanisms but treats the transition from PRZ to RZ as a single kinetic step.

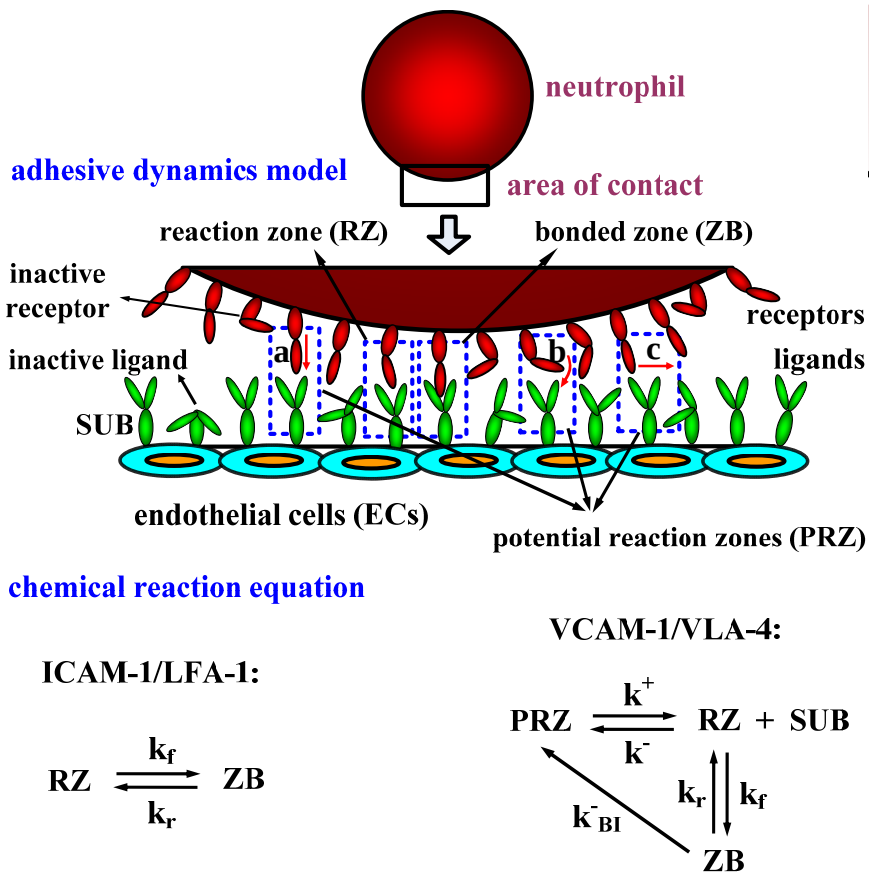

Figure 2.2 Adhesive dynamics model for VLA-4/VCAM-1 adhesion

In this novel model, the kinetics of binding involves five coefficients: k^+ and k^- govern the formation of RZ from PRZ; k_f and k_r represent the kinetics of forming or breaking a bond with a RZ; and k^-_{BI} characterizes the transition of a bond to the inactive zone. Here, SUB represents the density of ligand on the ECs surfaces. Like the general models, the probabilities of formation and breakage a VLA-4/VCAM-1 bond from RZ to ZB in a time step *dt* are calculated by equations (2.6)-(2.7). The probabilities of other three coefficients are governed by,

$$P^+ = 1 - \exp\left(-k^+ \cdot dt\right) \tag{2.8}$$

$$P^- = 1 - \exp\left(-k^- \cdot dt\right) \tag{2.9}$$

$$P_{BI}^- = 1 - \exp\left(-k_{BI}^- \cdot dt\right) \tag{2.10}$$

where P^+ and P^- are the probability of forming or breaking a RZ from PRZ in a time interval *dt*, respectively. P_{BI}^- is the probability of breaking a bound binding from ZB to be an inactive zone in a time interval *dt*.

2.2 Stochastic Monte Carlo Approach

In the simulations, the bonds are checked for formation and breakage according to their respective probabilities given by equations (2.6)-(2.7). When checking for bond formation, only the receptors of a reasonable proximity to the reactive surface are considered. For the receptors outside of the contact area, the probability of bond formation is vanishingly small, so it is assumed to be zero and not checked. At each time step, the unbound receptors on all microvilli in the contact area are tested for bond formation. Any free receptors on bound microvilli,

which may be outside of the contact area, are checked as well. Also, all the bound receptor-ligand bindings are tested for bond breakage. The positions of only the bound microvilli are stored from step to step, saving memory and computational time. The positions of unbound microvilli in contact area are randomly assigned to check for bond formation at each time step.

The stochastic Monte Carlo technique is used to determine the formation and breakage of each free and binding molecule during each time step. The procedure for updating the status of receptor-ligand bonds is as follows: the bond status at time t is checked first for each receptor on the circulating cell. If the receptor is bound to a ligand on the endothelial substrate at time t, a random number is generated between 0 and 1. If the random number is inferior to P_r determined by equation (2.7), the receptor will disengage at the next time step; otherwise, it will remain bound. If the receptor is free at time t and the receptor distance from the wall is inferior to H_c, a random number is also generated between 0 and 1. If the random number is inferior to P_f determined by equation (2.6), the receptor will bind to a ligand on the endothelial wall at the next time step; otherwise, it will remain free. In checking for bond formation and breakage, the time step dt required for accuracy in the results is 10^{-6} s.

As to the VLA-4/VCAM-1 adhesion, the probabilities of transitions follow equations (2.6)-(2.10). The stochastic Monte Carlo approaches for the transitions from PRZ to RZ, from RZ to ZB, and from ZB to PRZ are very similar to that of the general models that discussed above. The procedures for updating the status of

these three zones are carried out by comparing the probabilities of forward and reverse reactions rates given by equations (2.6)-(2.10) with the chosen random numbers between 0 and 1. If the random numbers are less than the probabilities, then the events will happen at the next time step; otherwise, the zones will keep the old state at the next time step. By these steps, the Monte Carlo approach simulates the stochastic process of cell adhesion in microcirculation.

2.3 Summary

In this chapter, the mathematical models of cell adhesion are introduced in detail. Two typical adhesive dynamics models for general cell adhesion are the Bell's model and Dembo et al.'s model, and a special adhesive dynamics model for VLA-4/VCAM-1 adhesion is the Waugh and Lomakina's model. All of the three models are respectively coupled in the simulations to calculate the effect of receptor-ligand bindings on cell adhesion under different physiological situations. Cell adhesion in microcirculation is actually a stochastic process, and therefore the stochastic Monte Carlo technique should be applied. The stochastic Monte Carlo approach is used to determine which receptor will bind to endothelial ligand or still keep free, and which bound binding will break at the next time step or still remain its bound state. The applications of these three adhesive dynamics models and the stochastic Monte Carlo approach will be embodied in Chapter 5, Chapter 6 and Chapter 7, respectively.

Chapter 3 Lattice Boltzmann Method

In this chapter, the research methodology is discussed in detail. The lattice Boltzmann method (LBM) is used to simulate the fluid dynamics. First of all, the Navier-Stokes equations and the lattice Boltzmann equation (LBE) are introduced. Secondly, the relationship between LBE and Boltzmann equation, and the relationship between LBE and Navier-Stokes equations are both derived. At last, three different boundary condition treatments in LBM are presented.

3.1 Navier-Stokes Equations

The Navier-Stokes equations are the governing equations for describing the motion of fluid substances. They are derived by invoking the continuum hypothesis, where the various fluid properties such as the density and velocity are assumed to be continuous functions of position with characteristic volume scale of 10^{-9} cm^3 (Batchelor 1970). Therefore, when given a specified volume, the fluid should follow the conservation of mass and momentum equations since all the scale quantities should be continuous. The conservation equations for an incompressible flow of Newtonian fluid can be expressed as,

$$\nabla \cdot \vec{u} = 0 \tag{3.1}$$

$$\rho(\frac{\partial \vec{u}}{\partial t} + \vec{u} \cdot \nabla \vec{u}) = -\nabla p + \mu \nabla^2 \vec{u} \tag{3.2}$$

where $\vec{u}$ is the fluid velocity, ρ is the fluid density, p is the pressure, μ is the fluid viscosity, and t is the time. The blood is a concentrated suspension of formed elements that includes red blood cells, leukocytes and platelets. The two-phase

nature of blood and the interactions between blood cells result in non-Newtonian dynamics for blood and the nonlinear relationship between stress and strain for blood flow. However, the plasma is Newtonian fluid, and the cellular components are suspended in plasma which also generally follows Newtonian dynamics (Sun and Munn 2005). Consequently, the Navier-Stokes equations (3.1)-(3.2) are still valid for our simulation system which describes few cells suspended in plasma. In order to simulate the fluid dynamics, an important work is that we should find an effective numerical method to solve these rigorous Navier-Stokes equations.

3.2 Lattice Boltzmann Equation

The LBM has been a promising numerical tool to effectively model complex physics in computational fluid dynamics (CFD). To date, the LBM has been successfully applied to various complex fluid flow systems, such as multiphase flows, magnetic fluids, fluid flows in porous media, reaction-diffusion systems, particles suspension flows, blood flows and other flow systems. A comprehensive review can be found in the paper of Chen and Doolen (1998).

The most distinctive feature of LBM is that it is based on a discretization of the Boltzmann equation, rather than on a discretization of the Navier-Stokes equations, like the conventional or traditional CFD methods. Compared to the conventional CFD solvers, the LBM has simple formulations, efficient parallel computing and can be easily to introduce complex boundary conditions. The fundamental idea of LBM is to construct simplified kinetic models that incorporate the essential physics of microscopic or mesoscopic processes so that

the macroscopic averaged properties obey the desired macroscopic equations. In this method, the fluid is described by the evolution of microscopic fluid particles or the particle distribution functions. The particle populations conserve mass and momentum during the collision and streaming, and the interactions between particles only depend on local information.

LBM was historically originated from the lattice gas cellular automata (LGCA) method, a discrete particle kinetics utilizing a discrete lattice and discrete time. The evolution equation of LGCA method is,

$$N_i(\vec{x}+\vec{e}_i, t+1) = N_i(\vec{x}, t) + \Omega_i\left[N(\vec{x}, t)\right] \tag{3.3}$$

where $\vec{e}_i$ is the local particle velocity, $N_i(\vec{x}, t)$ is a set of Boolean variables describing the particle occupation, and $\Omega_i\left[N(\vec{x}, t)\right]$ is the collision function.

McNamara and Zametti (1988) proposed the first LBE based on the LGCA method. They replaced the Boolean variables N_i in the LGCA by a single particle distribution function f_i, which is continuous variable ranging in the interval [0, 1]. Then, equation (3.3) can be written as,

$$f_i(\vec{x}+\vec{e}_i \cdot \delta t, t+\delta t) - f_i(\vec{x}, t) = \Omega_i\left[f_i(\vec{x}, t)\right] \tag{3.4}$$

where $f_i(\vec{x}, t)$ is the distribution function for the particle with velocity $\vec{e}_i$ at position $\vec{x}$ and time t, and δt is the time increment. $\Omega_i\left[f_i(\vec{x}, t)\right]$ is the collision operator that represents the rate of change of f_i resulting from collision. The collision term should be true to conserve mass and momentum at each lattice,

$$\sum \Omega_i\left(f_i(\vec{x}, t)\right) = 0 \tag{3.5}$$

$$\sum \vec{e}_i \cdot \Omega_i \left(f_i(\vec{x},t) \right) = 0 \tag{3.6}$$

The LBE retains the advantages of locality in the kinetic approach, which is essential to parallelism in the LGCA method. Moreover, it successfully eliminates statistical noise and accurately predicts the behavior of sound waves.

Since the usual aim of the LBM is to simulate macroscopic dynamics, the "exact" collision operator is unnecessarily complex and therefore numerically inefficient. At the beginning of 90th, Qian (1990) and Chen et al. (1991) did revolutionary work in the term of collision operator. Two groups nearly simultaneously suggested that the collision operator should be approximated by a single time relaxation in which relaxation towards some local equilibrium distribution function occurs at some constant rate, and the simplified collision term is expressed as,

$$\Omega_i \left[f_i(\vec{x},t) \right] = -\frac{1}{\tau} \left[f_i(\vec{x},t) - f_i^{eq}(\vec{x},t) \right] \tag{3.7}$$

where τ is the relaxation time, and $f_i^{eq}(\vec{x},t)$ is the equilibrium distribution function. $f_i^{eq}(\vec{x},t)$ depends on the local fluid variables and should be chosen appropriately to recover the macroscopic Navier-Stokes equations (Qian et al. 1992; Chen et al. 1992). The simplified LBE can be written as,

$$f_i(\vec{x} + \vec{e}_i \cdot \delta t, t + \delta t) - f_i(\vec{x},t) = -\frac{1}{\tau} \left[f_i(\vec{x},t) - f_i^{eq}(\vec{x},t) \right] \tag{3.8}$$

Equation (3.8) makes the computations more efficient and allows flexibility of the transport coefficients.

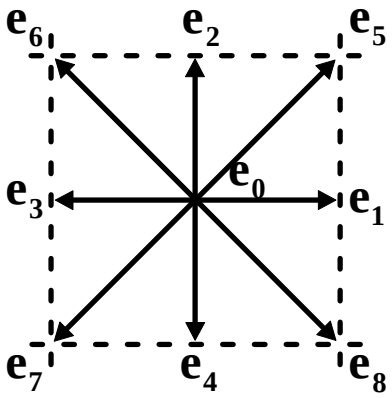

Figure 3.1 D2Q9 lattice Boltzmann model

Without losing generality, we take the D2Q9 model as an example, and the D2Q9 lattice Boltzmann model is shown in Fig. 3.1. To derive the macroscopic Navier-Stokes equations, an appropriate form of equilibrium distribution function can be chosen in a polynomial form as (Qian et al. 1992),

$$f_i^{eq}(\vec{x},t) = \rho w_i \left[1 + \frac{3}{c^2}(\vec{e}_i \cdot \vec{u}) + \frac{9}{2c^4}(\vec{e}_i \cdot \vec{u})^2 - \frac{3}{2c^2}u^2 \right] \tag{3.9}$$

where c is the lattice speed which is defined as $c = \delta x / \delta t$. δx is the length of lattice, and w_i is the weight coefficients that obtained by,

$$w_i = \begin{cases} 4/9, & i = 0. \\ 1/9, & i = 1,2,3,4. \\ 1/36, & i = 5,6,7,8. \end{cases} \tag{3.10}$$

Once the particle distribution function is known, the macroscopic fluid density ρ and velocity $\vec{u}$ are calculated by,

$$\rho = \sum f_i(\vec{x},t) = \sum f_i^{eq}(\vec{x},t) \tag{3.11}$$

$$\rho\vec{u} = \sum \vec{e}_i \cdot f_i(\vec{x},t) = \sum \vec{e}_i \cdot f_i^{eq}(\vec{x},t) \tag{3.12}$$

The evolution of LBM can be divided into two steps: (1) Collision, which occurs when particles arriving at a node interact and change their velocity directions according to scattering rules.

$$\tilde{f}_i(\vec{x},t) - f_i(\vec{x},t) = -\frac{1}{\tau}\left[f_i(\vec{x},t) - f_i^{(eq)}(\vec{x},t) \right] \tag{3.13}$$

(2) Streaming, in which each particle moves to the nearest node in the direction of its velocity.

$$f_i(\vec{x} + \vec{e}_i \cdot \delta t, t + \delta t) = \tilde{f}_i(\vec{x},t) \tag{3.14}$$

where $f_i(\vec{x},t)$ and $\tilde{f}_i(\vec{x},t)$ are the particle distribution function before and after collision, relatively.

3.3 Derivation of Lattice Boltzmann Equation from Boltzmann Equation

There are several ways to obtain the LBE from either discrete velocity models or the Boltzmann equation. The LBM is a derivation of the LGCA method, and we have introduced the LBE from the discrete kinetic equation of LGCA in Section 3.2. However, He and Luo (1997) demonstrated that the LBE is theoretically independent of LGCA, and they directly derived the LBE from the continuous Boltzmann equation. In this section, we briefly derive the LBE from the Boltzmann equation.

Based on the non-equilibrium statistics mechanics, the Boltzmann kinetic equation that considered the influence of collision on particle distribution function can be written as,

$$\frac{\partial f(\vec{x},\vec{v},t)}{\partial t} + \vec{v} \cdot \nabla f(\vec{x},\vec{v},t) = \iint \left[f(\vec{x},\vec{v}',t) f(\vec{x},\vec{v}_1',t) - f(\vec{x},\vec{v},t) f(\vec{x},\vec{v}_1,t) \right] d\varpi_1 \Lambda d\Omega \tag{3.15}$$

where $f(\vec{x},\vec{v},t)$ is the single particle distribution function, $\vec{v}$, $\vec{v}_1$ and $\vec{v}'$, $\vec{v}_1'$ are the velocities before and after collision, respectively, and $d\varpi_1$ is the velocity interval. $\Lambda d\Omega = d^2(\vec{v}-\vec{v}_1)\cdot\vec{n}d\Omega$, where d is the particle diameter, $\vec{n}$ is the direction along exterior normal, and $d\Omega$ is the solid angle. The velocities $\vec{v}'$ and $\vec{v}_1'$ are totally determined by the elastic collision. The Boltzmann equation can be simplified as,

$$\frac{\partial f(\vec{x},\vec{v},t)}{\partial t} + \vec{v}\cdot\nabla f(\vec{x},\vec{v},t) = \Omega(f) \tag{3.16}$$

where $\Omega(f)$ is the collision operator.

Bhathager, Gross and Krook (1954) firstly introduced a relaxation time approximation to simplify the collision operator. They indicated that when the particle distribution function f deviates from the local equilibrium distribution function $f^{(eq)}$ with $f - f^{(eq)}$, the rate of change of particle distribution function $\partial f/\partial t$ resulting from particles collision varies directly with $f - f^{(eq)}$, that is,

$$\Omega(f) = -\frac{1}{\tau}(f - f^{(eq)}) \tag{3.17}$$

This equation is also known as the BGK collision operator. Here, τ is the relaxation time and usually is the function of velocity. In most situations, τ is a constant by which approximately applying its average value. Now, the Boltzmann equation can be rewritten as,

$$\frac{\partial f}{\partial t} + \vec{v}\cdot\nabla f = -\frac{1}{\tau}(f - f^{(eq)}) \tag{3.18}$$

where $f_i^{(eq)}$ is the Maxwell-Boltzmann equilibrium distribution function which can be expressed as,

$$f^{(eq)} = \frac{\rho}{(2\pi RT)^{D/2}}\exp\left(-\frac{(\vec{v}-\vec{u})^2}{2RT}\right) \tag{3.19}$$

where T is the temperature, R is the ordinary gas constant, D is the spatial dimension, and $\vec{u}$ is the flow velocity. The macroscopic variables are obtained by taking various moments of the particle distribution function,

$$\rho = \int f d\vec{v} \tag{3.20}$$

$$\rho\vec{u} = \int f\vec{v} d\vec{v} \tag{3.21}$$

It is noticed that equation (3.18) is a partial differential equation, so we can use any known numerical methods to solve it. Discretizing the velocity in equation (3.18), then the Boltzmann equation can be expressed as,

$$\frac{\partial f_i}{\partial t} + \vec{e}_i \cdot \nabla f_i = -\frac{1}{\tau}(f_i - f_i^{(eq)}) \tag{3.22}$$

where $\vec{e}_i$ is the microscopic particle velocity in the i^{th} direction. In the D2Q9 lattice Boltzmann model, the nine-bit velocities set are,

$$\vec{e}_i = \begin{cases} 0, \ i = 0. \\ \left[\cos\left(\frac{i-1}{2}\pi\right), \sin\left(\frac{i-1}{2}\pi\right)\right], \ i = 1,2,3,4. \\ \sqrt{2}\left[\cos\left(\frac{2i-1}{4}\pi\right), \sin\left(\frac{2i-1}{4}\pi\right)\right], \ i = 5,6,7,8. \end{cases} \tag{3.23}$$

We continue to discretize equation (3.22) in both time and space. If we apply the first order finite difference scheme in time, then the first order upwind discretization for the convective term can be given as,

$$\begin{aligned} &\left[f_i(\vec{x}, t+\delta t) - f_i(\vec{x}, t)\right] + \frac{\delta t}{\delta x}\left[f_i(\vec{x} + \vec{e}_i \cdot \delta t, t+\delta t) - f_i(\vec{x}, t+\delta t)\right] \\ &= -\frac{1}{\tau}\left[f_i(\vec{x}, t) - f_i^{(eq)}(\vec{x}, t)\right] \end{aligned} \tag{3.24}$$

where δx and δt are the length of lattice and time increment, respectively. If choosing $\delta t/\delta x = 1$, equation (3.24) becomes the standard LBE (3.8), which gives the second order accuracy for the macroscopic variable in both time and space.

Up to now, we have derived the LBE from the Boltzmann equation by using a relaxation time approximation proposed by Bhathager, Gross and Krook (1954). Therefore, the single relaxation time lattice Boltzmann model is also called as the BGK model. The BGK model is the simplest LBM model. Due to its extreme simplicity, the BGK has become the most popular LBM model.

3.4 Recovery of Navier-Stokes Equations from Lattice Boltzmann Equation

There are also many methods to derive the macroscopic Navier-Stokes equations from the LBE (He and Luo 1997; Chen and Doolen 1998). The main technique applied in the derivation is the Chapman-Enskog multiscale expansion (Frish et al. 1987). In this section, we will briefly present the recovery of the macroscopic Navier-Stokes equations for incompressible flows from the discrete LBE via an example of D2Q9 lattice Boltzmann model.

Introducing the Taylor expansion,

$$f_i(\vec{x} + \vec{e}_i \cdot \delta t, t + \delta t) = \sum_{n=0}^{\infty} \frac{\varepsilon^n}{n!} D_t^n f_i(\vec{x}, t) \tag{3.25}$$

where ε is the Knudsen number, and $D_t = (\partial t + \vec{e}_i \cdot \nabla)$.

From equation (3.8), we can easily get,

$$f_i(\vec{x} + \vec{e}_i \cdot \delta t, t + \delta t) - f_i(\vec{x}, t) = \sum_{n=1}^{\infty} \frac{\varepsilon^n}{n!} \left[\frac{\partial}{\partial t} + \vec{e}_i \frac{\partial}{\partial x_k} \right]^n f_i(\vec{x}, t) \tag{3.26}$$

where k =1 and 2, which represents the x, y direction, respectively.

Preserving equation (3.26) with second order $O(\varepsilon^2)$, and we can obtain the following equation from equation (3.8),

$$\begin{aligned}\varepsilon\left(\frac{\partial}{\partial t}+\vec{e}_i\frac{\partial}{\partial x_k}\right)f_i(\vec{x},t)+\frac{\varepsilon^2}{2}\left(\frac{\partial}{\partial t}+\vec{e}_i\frac{\partial}{\partial x_k}\right)^2 f_i(\vec{x},t)+O(\varepsilon^3)\\ =-\frac{1}{\tau}\left[f_i(\vec{x},t)-f_i^{(eq)}(\vec{x},t)\right]\end{aligned} \tag{3.27}$$

Introducing two time scales, t_0 and t_1, where $t_0 = t$ and $t_1 = \varepsilon t$. Employing the Chapman-Enskog multiscale expansion technique (Frish et al. 1987) gives,

$$\frac{\partial}{\partial t}=\frac{\partial}{\partial t_0}+\varepsilon\frac{\partial}{\partial t_1}+\cdots \tag{3.28}$$

Equation (3.28) assumes that time scale t_1 is much smaller than the time scale t_0. Likewise, the particle distribution function f_i can be expanded by the local equilibrium distribution function $f_i^{(eq)}$,

$$f_i(\vec{x},t)=f_i^{(eq)}(\vec{x},t)+\varepsilon\cdot f_i^{(neq)}(\vec{x},t) \tag{3.29}$$

where $f_i^{(neq)}(\vec{x},t)$ depends on the local macroscopic variables (ρ and $\rho\vec{u}$) and should satisfy the equations (3.11)-(3.12), and $f_i^{(neq)}(\vec{x},t)=f_i^{(1)}(\vec{x},t)+f_i^{(1)}(\vec{x},t)$ $+\varepsilon\cdot f_i^{(2)}(\vec{x},t)+O(\varepsilon^2)$ is the non-equilibrium distribution function which has the following constrains,

$$\sum_i f_i^{(k)}(\vec{x},t)=0,\ k=1,\ 2. \tag{3.30}$$

$$\sum_i \vec{e}_i\cdot f_i^{(k)}(\vec{x},t)=0,\ k=1,\ 2. \tag{3.31}$$

Substituting equations (3.28) and (3.29) into equation (3.27) gives,

$$\varepsilon\left(\frac{\partial}{\partial t_0}+\varepsilon\frac{\partial}{\partial t_1}+\vec{e}_i\frac{\partial}{\partial x_k}\right)\left(f_i^{(eq)}(\vec{x},t)+\varepsilon f_i^{(1)}(\vec{x},t)+\varepsilon^2 f_i^{(2)}(\vec{x},t)\right)$$
$$+\frac{\varepsilon^2}{2}\left(\frac{\partial}{\partial t_0}+\varepsilon\frac{\partial}{\partial t_1}+\vec{e}_i\frac{\partial}{\partial x_k}\right)^2\left(f_i^{(eq)}(\vec{x},t)+\varepsilon f_i^{(1)}(\vec{x},t)+\varepsilon^2 f_i^{(2)}(\vec{x},t)\right) \tag{3.32}$$
$$=-\frac{1}{\tau}\varepsilon f_i^{(1)}(\vec{x},t)-\frac{1}{\tau}\varepsilon^2 f_i^{(2)}(\vec{x},t)$$

From equation (3.32), we can obtain the following equation,

$$\left(\frac{\partial}{\partial t_0}+\vec{e}_i\frac{\partial}{\partial x_k}\right)f_i^{(eq)}(\vec{x},t)=-\frac{1}{\tau}f_i^{(1)}(\vec{x},t) \tag{3.33}$$

to the first order ε, and

$$\frac{\partial}{\partial t_1}f_i^{(eq)}(\vec{x},t)+\left(\frac{\partial}{\partial t_0}+\vec{e}_i\frac{\partial}{\partial x_k}\right)f_i^{(1)}(\vec{x},t)+\frac{1}{2}\left(\frac{\partial}{\partial t_0}+\vec{e}_i\frac{\partial}{\partial x_k}\right)^2 f_i^{(eq)}(\vec{x},t)$$
$$=-\frac{1}{\tau}f_i^{(1)}(\vec{x},t) \tag{3.34}$$

to the second order ε^2. Using equation (3.33) and some algebra, we can rewrite the second order ε^2 of equation (3.34) as,

$$\frac{\partial}{\partial t_1}f_i^{(eq)}(\vec{x},t)+\left(1-\frac{1}{2\tau}\right)\cdot\left(\frac{\partial}{\partial t_0}+\vec{e}_i\frac{\partial}{\partial x_k}\right)f_i^{(1)}(\vec{x},t)=-\frac{1}{\tau}f_i^{(2)}(\vec{x},t) \tag{3.35}$$

Combining with equations (3.11)-(3.12) and (3.30)-(3.31), we can derive the following equations from equation (3.33) and (3.35),

$$\frac{\partial}{\partial t}\rho+\nabla\cdot\rho\vec{u}=0 \tag{3.36}$$

$$\frac{\partial}{\partial t}\rho\vec{u}+\nabla\cdot\Pi=0 \tag{3.37}$$

Equations (3.36)-(3.37) are the continuity equation and momentum equation in fluid mechanics, which are also accurate to second order in ε for equation (3.8). Here, the momentum flux tensor Π is defined as,

$$\Pi_{\alpha\beta} = \sum_i (\vec{e}_i)_\alpha (\vec{e}_i)_\beta \left(f_i^{(eq)} + \left(1 - \frac{1}{2\tau}\right) \varepsilon f_i^{(1)}(\vec{x}, t) \right) \tag{3.38}$$

where $(\vec{e}_i)_\alpha$ is the component of velocity vector $\vec{e}_i$ in the α-coordinate direction.

To specify the detailed form of $\Pi_{\alpha\beta}$, the lattice structure and corresponding equilibrium distribution function have to be specified. For simplicity and without losing generality, we also consider the D2Q9 lattice Boltzmann model. Noting that the Navier-Stokes equations have a second order nonlinearity, an appropriate form of equilibrium distribution function with a second order approximation has been obtained analytically (Qian et al. 1992) and has been given in equation (3.9), which is valid only for small velocities or small Mach number u/C_s, where $C_s = 1/\sqrt{3}$ is the sound speed. Inserting equation (3.9) into equation (3.38) yields,

$$\Pi_{\alpha\beta}{}^{(eq)} = \sum_{\alpha\beta} (\vec{e}_i)_\alpha (\vec{e}_i)_\beta f_i^{(eq)}(\vec{x}, t) = p\delta_{\alpha\beta} + \rho u_\alpha u_\beta \tag{3.39}$$

$$\Pi_{\alpha\beta}{}^{(1)} = \sum_i (\vec{e}_i)_\alpha (\vec{e}_i)_\beta \left(1 - \frac{1}{2\tau}\right) \varepsilon f_i^{(1)}(\vec{x}, t) = \upsilon \left(\nabla_\alpha (\rho \vec{u}_\beta) + \nabla_\beta (\rho \vec{u}_\alpha) \right) \tag{3.40}$$

where $p = \rho C_s{}^2 = \rho / 3$ is the pressure, and υ is the kinematic viscosity which is defined as,

$$\upsilon = \frac{1}{6}(2\tau - 1) \tag{3.41}$$

The resulting momentum equation is,

$$\rho\left(\frac{\partial u_\alpha}{\partial t} + \nabla_\beta \cdot \vec{u}_\alpha \vec{u}_\beta\right) = -\nabla_\alpha p + \upsilon \nabla_\beta \cdot (\nabla_\alpha \rho \vec{u}_\beta + \nabla_\beta \rho \vec{u}_\alpha) \tag{3.42}$$

Equation (3.42) is exactly the same as the Navier-Stokes equation (3.2) if the density variation $\delta\rho$ is small enough.

From the above discussion, it can be easily concluded that the Navier-Stokes

equations can be recovered from the LBE under the incompressible limitation. Therefore, we can use the LBM to study the fluid behavior in both time and space. It should be noted that the LBM must be carried out under three constrains: (1) Mach number: Ma<<1; (2) density variation: $\delta\rho$<<1; and (3) Knudsen number ε is small enough. Otherwise, the calculation will be diverging, and cannot obtain reliable results.

3.5 Boundary Conditions in Lattice Boltzmann Method

Boundary condition plays an extremely important role in the lattice Boltzmann simulations. It will greatly influence the accuracy and stability of the numerical results. Achieving self-consistent boundary conditions with a given accuracy and stability is as important as developing the lattice Boltzmann models themselves. In recent years, many researchers have proposed various boundary conditions to improve the accuracy and stability in LBM simulations. In this section, we will introduce several frequently used boundary conditions treatments, i.e., bounce back boundary scheme, pressure and velocity boundary scheme, and curved moving boundary scheme, all of which will be adopted in our simulations.

3.5.1 Bounce Back Boundary Scheme

The most popular boundary condition for LBM is the bounce back scheme. The so-called standard bounce back scheme means that when a particle reaches a wall node, the particle will reflect back to the fluid nodes along its incoming direction in the next streaming step.

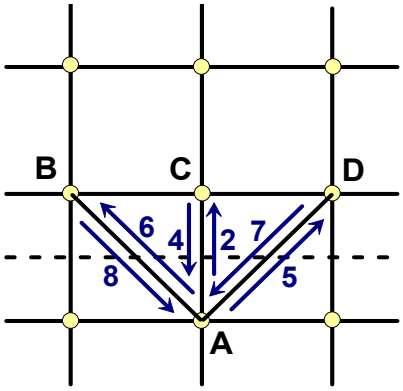

Figure 3.2 Bounce back and half-way bounce back boundary scheme

As shown in Fig. 3.2, assuming A is in the physical boundary, B, C and D are the nearest interior fluid nodes, and the fluid particle can flow from B, C, and D to A. When a particle moves from B to A with velocity 8, there will be a corresponding particle flows from A to B with velocity 6 in the next streaming step. The particle moving from C and D to A is the same as that from B to A. Therefore, the bounce back scheme can lead to a mass conservation and "zero" velocity condition on the wall. It may be a preferable method for modeling no-slip boundaries, which also supports the idea that the LBM is ideal for modeling fluid flows in complicated geometries. Up to now, the bounce back boundary condition has been widely used in the LBM simulations (Ziegler 1993; Noble et al. 1995; Gallivan et al. 1997).

However, it was noticed that the bounce back scheme is only first order in numerical accuracy of boundary that degrades the LBM, since the accuracy of LBM in the interior nodes is second order (Cornubert et al. 1991; Ginzbourg and Adler 1994). This motivated the researchers to develop new boundary treatments to achieve second order accuracy for no-slip velocity boundary condition. Among

them, a typical work was reported by Ziegler (1993). Ziegler noticed that if the boundary was shifted into fluid by a half mesh unit, i.e. placing the non-slip condition between nodes (half-way bounce back scheme), then the bounce back scheme will give second order accuracy. The half-way bounce back rule inherits the advantage of bounce back rule that is very easy to be implemented in computer codes. When the boundary is in parallel with lattices, and locates in the middle of nodes, the no-slip boundary condition can be easily carried out. However, it cannot realize the no-slip boundary condition in the inclined or curved boundaries. Therefore, the half-way bounce back scheme is usually applied in LBM to solve the flat boundary conditions.

3.5.2 Pressure and Velocity Boundary Scheme

In many practical flow systems, a flow is always driven by pressure difference or pressure gradient. In this situation, the boundary conditions such as prescribed pressure or velocity on flow boundaries are needed. Zou and He (1997) proposed a new way to specify pressure or velocity on flow boundaries based on the idea of bounce back rule of the non-equilibrium distribution function.

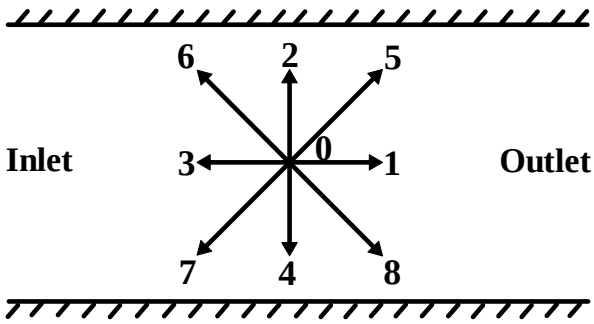

Figure 3.3 Pressure and velocity boundary scheme

The schematic view of pressure and velocity boundary scheme is shown in Fig. 3.3. In the inlet, the distribution functions f_1, f_5 and f_8 are unknown after streaming. Similarly, in the outlet, the distribution functions f_3, f_6 and f_7 are unknown after streaming. Our objective is to get their values under a specific pressure or velocity. According to the mass and velocity definition equations (3.11)-(3.12), we can easily get

$$f_0 + f_1 + f_2 + f_3 + f_4 + f_5 + f_6 + f_7 + f_8 = \rho \tag{3.43}$$

$$f_1 - f_3 + f_8 - f_6 + f_5 - f_7 = \rho u_x \tag{3.44}$$

$$f_2 - f_4 + f_5 - f_7 + f_6 - f_8 = \rho u_y \tag{3.45}$$

(1) Pressure boundary scheme

In the LBM, the specification of pressure difference amounts to the specification of a density difference, since there is a formula describing the relationship between pressure and density as $p = \rho C_s^{\,2} = \rho / 3$. That is to say, the pressure in the boundary can be specified if the density is given.

In the inlet, assuming the density is $\rho = \rho_{in}$, and the *y* direction velocity u_y is specified as 0, but the *x*-direction velocity u_x is unknown. After streaming, f_0, f_2, f_3, f_4, f_6 and f_7 are known in addition to $\rho = \rho_{in}$ and u_y =0, but f_1, f_5 and f_8 are still unknown. So we need to determine f_1, f_5, f_8 and u_x four unknowns. Consistent with equations (3.43)-(3.45), we can get u_x as follows,

$$u_x = 1 - \frac{f_0 + f_2 + f_4 + 2(f_3 + f_6 + f_7)}{\rho_{in}} \tag{3.46}$$

There are only three equations for four unknowns, so we need to find one more

equation. We assume that the bounce back rule is still valid for the non-equilibrium part of distribution function which is normal to the boundary. Here, since f_1 is normal to the inlet boundary, then

$$f_1 - f_1^{(eq)} = f_3 - f_3^{(eq)} \tag{3.47}$$

Substituting the local equilibrium distribution function into equation (3.47) gives,

$$f_1 = f_3 + (f_1^{(eq)} - f_3^{(eq)}) = f_3 + 6\rho_{in} w_1 u_x \tag{3.48}$$

Inserting equation (3.48) into equations (3.44) and (3.45) yields,

$$f_5 = f_7 - \frac{1}{2}(f_2 - f_4) + (\frac{1}{2} - 3w_1)\rho_{in} u_x \tag{3.49}$$

$$f_8 = f_6 + \frac{1}{2}(f_2 - f_4) + (\frac{1}{2} - 3w_1)\rho_{in} u_x \tag{3.50}$$

In the outlet, assuming that the density is $\rho = \rho_{out}$, and the velocity u_y is specified as 0, but the velocity u_x is still unknown. After streaming, f_0, f_1, f_2, f_4, f_5 and f_8 are known in addition to $\rho = \rho_{out}$ and $u_y = 0$, but f_3, f_6 and f_7 are still unknown. So we need to determine f_3, f_6, f_7 and u_x four unknowns. From equations (3.43)-(3.45), we can also get u_x,

$$u_x = -1 + \frac{f_0 + f_2 + f_4 + 2(f_1 + f_5 + f_8)}{\rho_{out}} \tag{3.51}$$

Similarly, the left three unknown distribution functions are calculated by,

$$f_3 = f_1 - 6\rho_{out} w_1 u_x \tag{3.52}$$

$$f_6 = f_8 - \frac{1}{2}(f_2 - f_4) - (\frac{1}{2} - 3w_1)\rho_{out} u_x \tag{3.53}$$

$$f_7 = f_5 - \frac{1}{2}(f_2 - f_4) - (\frac{1}{2} - 3w_1)\rho_{out} u_x \tag{3.54}$$

(2) Velocity boundary scheme

Now, let us turn to the velocity flow boundary condition. Actually, the derivation of unknowns here is very similar with the pressure boundary condition mentioned above. Firstly, we get the density from equations (3.43)-(3.45). Secondly, we calculate the distribution function which is normal to the boundary. Finally, we obtain the left unknown distribution functions.

In the inlet, assuming the velocity at the inlet is (u_x, u_y), but the density ρ here is unknown. After streaming, f_0, f_1, f_2, f_4, f_5 and f_8 are known, and f_3, f_6 and f_7 are unknown. Firstly, we get the density,

$$\rho = 1 - \frac{f_0 + f_2 + f_4 + 2(f_3 + f_6 + f_7)}{1 - u_x} \tag{3.55}$$

Secondly, we get the normal distribution function,

$$f_1 = f_3 + 6\rho w_1 u_x \tag{3.56}$$

Finally, the left unknown distribution functions are obtained by,

$$f_5 = f_7 - \frac{1}{2}(f_2 - f_4) + \frac{1}{2}\rho u_y + (\frac{1}{2} - 3w_1)\rho u_x \tag{3.57}$$

$$f_8 = f_6 + \frac{1}{2}(f_2 - f_4) + \frac{1}{2}\rho u_y + (\frac{1}{2} - 3w_1)\rho u_x \tag{3.58}$$

Similarly, in the outlet, all the unknowns can be obtained by,

$$\rho = \frac{f_0 + f_2 + f_4 + 2(f_1 + f_5 + f_8)}{1 + u_x} \tag{3.59}$$

$$f_3 = f_1 - 6\rho w_1 u_x \tag{3.60}$$

$$f_6 = f_8 - \frac{1}{2}(f_2 - f_4) + \frac{1}{2}\rho u_y - (\frac{1}{2} - 3w_1)\rho u_x \tag{3.61}$$

$$f_7 = f_5 + \frac{1}{2}(f_2 - f_4) - \frac{1}{2}\rho u_y - (\frac{1}{2} - 3w_1)\rho u_x \tag{3.62}$$

3.5.3 Curved Moving Boundary Scheme

The above treatments of boundary are fully competent for the flat stationary boundaries. However, the boundaries of many fluid systems are not only curved but also mobile. A usual and typical example is the boundary of a moving particle. Many researchers have done important work in developing the curved moving boundary conditions. Filippova and Hänel (1997) proposed a boundary fitting conditions based on the fictitious equilibrium distribution function. However, it was found the numerical results are strongly instable when the relaxation time τ is close to 0.5. To overcome this shortcoming, Mei et al. (1999) improved an alternative scheme, which is second order accuracy in boundary condition. However, the instability is still in existence due to the dependence of weighting factor that controls the linear interpolation on the relaxation time. Bouzidi et al. (2001) put forward another treatment for arbitrary geometry moving boundaries according to the intuitive notion of "bounce back" and interpolations. Lallemand and Luo (2003) applied the interpolations differently for before and after collision. The method inherits the advantage of the bounce back scheme which is very easy to be implemented. Besides, an extrapolation method for curved and moving boundary condition was developed by Guo et al. (2002). This treatment of boundary condition is very easy in code and has been proved to be of second order accuracy and has well-behaved stability characteristics. In the next, we present this extrapolation method, which is also applied in our simulations for solving the boundaries of stationary curved micro-vessel wall and moving cells.

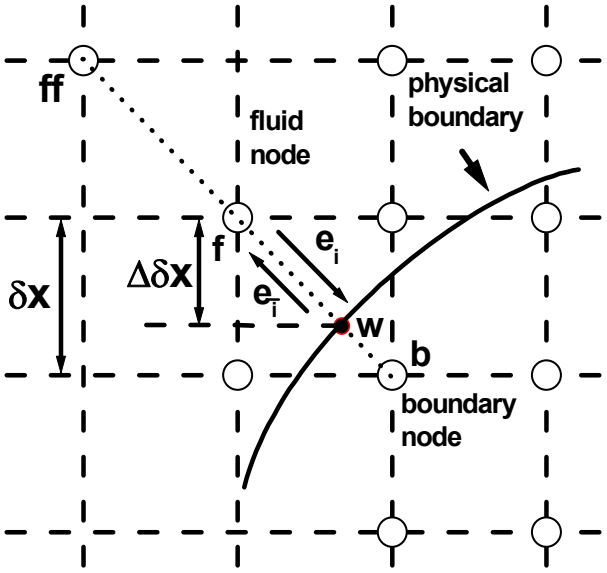

Figure 3.4 Curved moving boundary scheme.

Fig. 3.4 shows the schematic view of the curved moving boundary scheme. δx is the length of lattice, $\vec{x}_f$ is the fluid node, $\vec{x}_b$ is the boundary node, a physical boundary $\vec{x}_w$ is intersected between the fluid node $\vec{x}_f$ and boundary node $\vec{x}_b$. Here, $\vec{x}_f = \vec{x}_b + \vec{e}_i\delta_x$, $\vec{x}_{ff} = \vec{x}_f + \vec{e}_i\delta_x$, and $\vec{e}_{\bar{i}} = -\vec{e}_i$. The fraction of intersected link in the fluid region is:

$$\Delta = \frac{\left|\vec{x}_f - \vec{x}_w\right|}{\left|\vec{x}_f - \vec{x}_b\right|}, \quad 0 \le \Delta \le 1 \tag{3.63}$$

After collision, the distribution function $\tilde{f}_i(\vec{x}_f, t)$ at the node $\vec{x}_f$ is known. However, we should know the distribution function $\tilde{f}_{\bar{i}}(\vec{x}_b, t)$ that moves from the boundary node $\vec{x}_b$ to the fluid node $\vec{x}_f$ in the streaming step. The so-called boundary condition here is to calculate $\tilde{f}_{\bar{i}}(\vec{x}_b, t)$.

The basic idea of the extrapolation method is to decompose the distribution at the boundary node into two parts, i.e., the equilibrium part and the non-equilibrium part. The equilibrium part is determined by a fictitious equilibrium

distribution, and the non-equilibrium part is approximated by that of the neighboring fluid node along the link. So the distribution function at $\vec{x}_b$ is,

$$\tilde{f}_{\bar{i}}(\vec{x}_b,t) = f_{\bar{i}}^{eq}(\vec{x}_b,t) + (1-\frac{1}{\tau}) f_{\bar{i}}^{ne}(\vec{x}_b,t) \tag{3.64}$$

where the equilibrium distribution function $f_{\bar{i}}^{eq}(x_b,t) = f_{\bar{i}}^{eq}(\rho_b,\vec{u}_b,t)$ and is approximated by,

$$f_{\bar{i}}^{eq}(\vec{x}_b,t) = w_{\bar{i}} \left\{ \overline{\rho}_b + \rho_0 \left[\frac{3}{c^2}(\vec{e}_{\bar{i}} \cdot \overline{\vec{u}}_b) + \frac{9}{2c^4}(\vec{e}_{\bar{i}} \cdot \overline{\vec{u}}_b)^2 - \frac{3}{2c^2}\overline{u}_b^{\,2} \right] \right\} \tag{3.65}$$

where $\overline{\rho}_b = \rho(\vec{x}_f)$ is an approximation of $\overline{\rho}_b = \rho(\vec{x}_b)$, $\overline{\vec{u}}_b$ is an approximation of $\vec{u}_b = \vec{u}(\vec{x}_b)$, and they are chosen as,

$$\rho_b = \rho_f \tag{3.66}$$

$$\vec{u}_b = \begin{cases} \dfrac{\vec{u}_w + (\Delta-1)\vec{u}_f}{\Delta}, & \Delta \geq \mathrm{A} \\ \dfrac{2\vec{u}_w + (\Delta-1)\vec{u}_{ff}}{1+\Delta}, & \Delta < \mathrm{A} \end{cases} \tag{3.67}$$

where $\vec{u}_w$ is the velocity of the wall. $\vec{u}_w$ is zero for the stationary boundary and non-zero for the moving boundary. The non-equilibrium part $f_{\bar{i}}^{ne}(\vec{x}_b,t)$ can be approximated by the non-equilibrium part of distribution function at the fluid node $\vec{x}_f$ and $\vec{x}_{ff}$ with second order accuracy,

$$f_{\bar{i}}^{ne}(\vec{x}_b,t) = \begin{cases} f_{\bar{i}}(\vec{x}_f,t) - f_i^{eq}(\vec{x}_f,t), \Delta \geq A \\ \Delta\left(f_{\bar{i}}(\vec{x}_f,t) - f_{\bar{i}}^{eq}(\vec{x}_f,t)\right) + (1-\Delta)\left(f_{\bar{i}}(\vec{x}_{ff},t) - f_{\bar{i}}^{eq}(\vec{x}_{ff},t)\right), \Delta < A \end{cases} \tag{3.68}$$

Now, $f_{\bar{i}}^{eq}(\vec{x}_b,t)$ and $f_{\bar{i}}^{ne}(\vec{x}_b,t)$ are known, so the $\tilde{f}_{\bar{i}}(\vec{x}_b,t)$ can be also obtained by equation (3.64), where $A \in (0,1)$.

Chapter 4 Forces Evaluation

In this thesis, the cell dynamics is governed by the Newton's law of translation and rotation. In order to solve the cell dynamics, we should know how many forces acting on the cell. There are mainly three forces governing the cell adhesion and migration under flow condition. They are hydrodynamic force which is induced by the surrounding blood, repulsive van der Waals force which is provided by the endothelial wall, and spring force that caused by the stochastic receptor-ligand bindings. The accurate evaluation of these three forces plays a key role on the analysis of cell adhesion behavior. In this chapter, we mainly focus on the derivation and computation of these three forces, and then we carry out the cell dynamics under the governing of these forces.

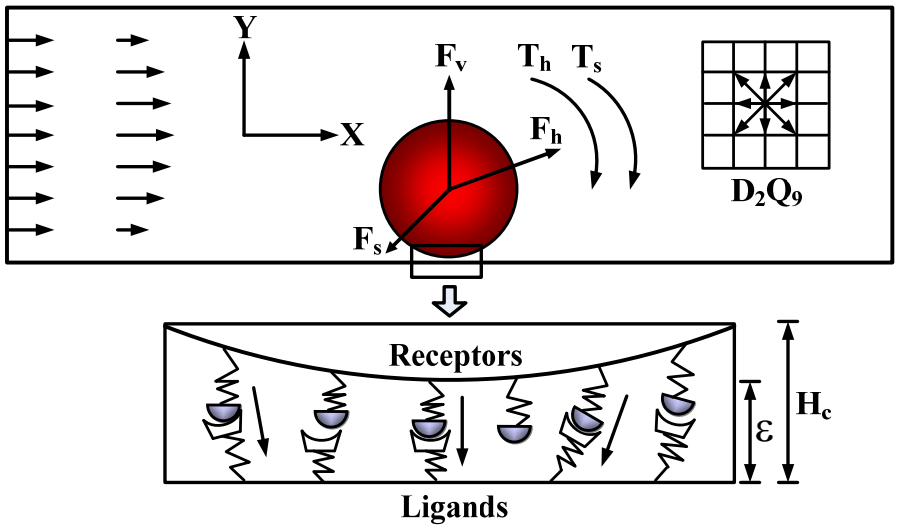

Figure 4.1 Force analysis in cell adhesion

The schematic view of forces analysis during cell adhesion is illustrated in Fig. 4.1. $\vec{F}_h$ is the hydrodynamic force, $\vec{F}_v$ is the repulsive van der Waals force,

and $\vec{F}_s$ is the spring force. T_h and T_s are the torques that provided by hydrodynamic force and spring force, respectively. Since $\vec{F}_v$ is normal to the interaction interface, there is no torque induced by the repulsive van der Waals force. In the next, we will discuss the evaluation of these three forces.

4.1 Hydrodynamic Force

The accurate evaluation of the fluid dynamic force involving curved boundaries is crucial to the study of fluid-structure interaction. There are mainly two methods can be used to determine the hydrodynamic force on a curved body in the context of LBM: (1) stress integration, and (2) momentum exchange. Many researches carried out studies on both two methods. He and Doolen (1997) evaluated the fluid force by integrating the total stress on the surface of cylinder, and the components of the stress tensor were obtained by taking respective velocity gradients. Ladd (1994) proposed the momentum exchange method to compute the fluid force on a sphere in particles suspension flow by the LBM. Aidun et al. (1998) continued to extend the Ladd's approach to any solid-to-fluid density ratio, which also adopted the momentum exchange method to evaluate fluid force. A comprehensive review of these two methods can be found in the paper of Mei et al. (2002). Compared to the stress integration method, the momentum exchange method is much easier to be implemented computationally. Therefore, it has been widely applied in solving the curved moving boundary in the LBM simulations. In this thesis, we also adopt the momentum exchange method to calculate the hydrodynamic force.

4.1.1 Momentum Exchange Method

As shown in Fig. 3.4, after the collision step, the particle distribution function $\tilde{f}_i(\vec{x}_f,t)$ at the fluid node $\vec{x}_f$ will move along $\vec{e}_i$ to the boundary node $\vec{x}_b$ in the streaming step. So the momentum increment at the boundary node $\vec{x}_b$ is $\vec{e}_i\tilde{f}_i(\vec{x}_f,t)$. On the other hand, the calculated particle distribution function $\tilde{f}_{\bar{i}}(\vec{x}_b,t)$ at the boundary node $\vec{x}_b$ will stream along $\vec{e}_{\bar{i}}$ to the fluid node $\vec{x}_f$ in the streaming step. So the momentum decrement at the boundary node $\vec{x}_b$ is $\vec{e}_{\bar{i}}\tilde{f}_{\bar{i}}(\vec{x}_b,t)$. So the force that acted by the fluid node $\vec{x}_f$ on the boundary node $\vec{x}_b$ can be obtained by the net momentum increment at the boundary node $\vec{x}_b$,

$$\vec{F}(\vec{x}_b)=\vec{e}_i\cdot\tilde{f}_i(\vec{x}_f,t)-\vec{e}_{\bar{i}}\cdot\tilde{f}_{\bar{i}}(\vec{x}_b,t) \tag{4.1}$$

Because of $\vec{e}_i=-\vec{e}_{\bar{i}}$, then

$$\vec{F}(\vec{x}_b)=\vec{e}_i\cdot\left[\tilde{f}_i(\vec{x}_f,t)+\tilde{f}_{\bar{i}}(\vec{x}_b,t)\right] \tag{4.2}$$

So the total fluid dynamic force is the sum of $\vec{F}(\vec{x}_b)$, that is

$$\vec{F}_T=\sum\vec{F}(\vec{x}_b)=\sum\vec{e}_i\cdot\left[\tilde{f}_i(\vec{x}_f,t)+\tilde{f}_{\bar{i}}(\vec{x}_b,t)\right] \tag{4.3}$$

Then, the total torque can be obtained by,

$$\vec{T}_T=\sum(\vec{x}_b-\vec{x}_0)\times\vec{F}(\vec{x}_b)=\sum(\vec{x}_b-\vec{x}_0)\cdot\vec{e}_i\cdot\left[\tilde{f}_i(\vec{x}_f,t)+\tilde{f}_{\bar{i}}(\vec{x}_b,t)\right] \tag{4.4}$$

where $\vec{x}_0$ generally is the center of mass of the solid particle.

4.1.2 Lubrication Theory

When the distance between circulating cells or between a circulating cell and endothelial wall is superior to one lattice spacing, the momentum exchange method are completely competent for the calculation of hydrodynamic force.

However, when two surfaces come within one lattice spacing, the fluid nodes are excluded from the regions between solid surfaces, leading to a loss of mass conservation. In our simulations, three cases of losing lattice nodes should be considered, which are all shown in Fig. 4.2. Case 1: surfaces between a circulating cell and a straight vessel wall; Case 2: surfaces between two circulating cells or between a circulating cell and a stationary positive curvature vessel wall; and Case 3: surfaces between a circulating cell and a stationary negative curvature vessel wall. In the next, we should find an approach to calculate the losing forces, and add them to the hydrodynamic forces.

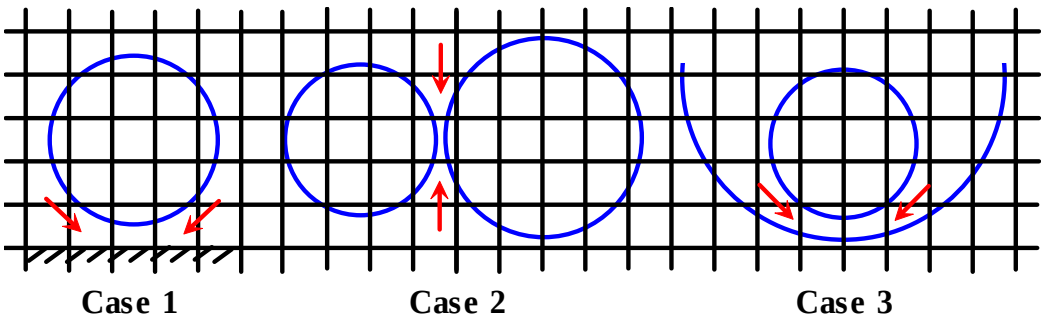

Figure 4.2 Three cases of losing lattice nodes

According to the lubrication theory (Durlofsky et al. 1987), when two solid surfaces approach each other, there will be a strong repulsive force caused by fluid being squeezed out of the gap between solid surfaces. Moreover, this kind of lubrication flow will generate very high pressure in the gap. However, the pressure will reduce to be much smaller due to the loss of lattices nodes between two solid surfaces, which is in contradiction with the lubrication theory. To our best knowledge, there are two methods can be used to resolve this problem: (1)

using adaptive meshes technique; and (2) adding normal lubrication force between two surfaces. Compared to the adaptive meshes technique, the second approach is much tractable in computer code. When the distance between two solid surfaces is within a critical value (i.e., the distance is within one lattice spacing), we should introduce a lubrication force to compensate the loss of fluid pressure. The lubrication theory has been widely employed in the LBM simulations since it was firstly incorporated into LBM in simulating particles suspensions (Ladd 1997).

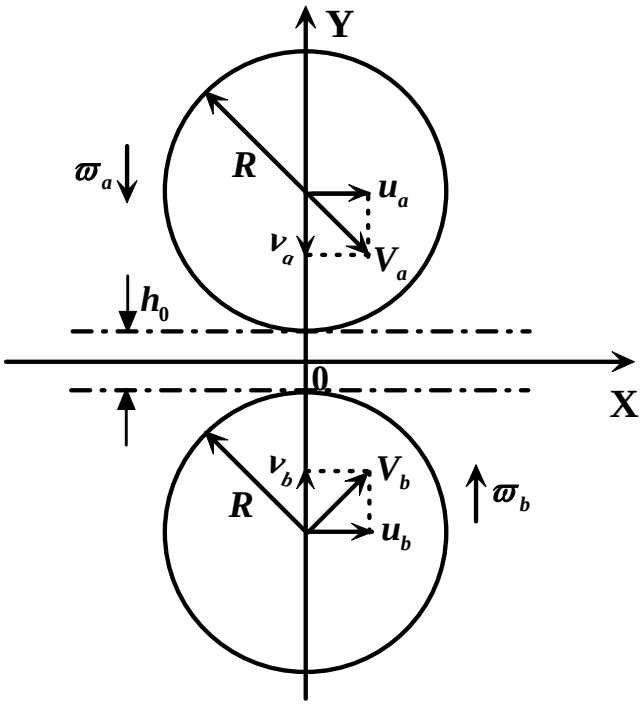

Figure 4.3 Geometry of two equal disks at near distance

As shown in Fig. 4.3, an analytical solution of lubrication force between two same disks was firstly obtained by Yuan and Ball (1994). They found that the normal squeezing force could be given by,

$$F_N^{\text{lub}} = -\frac{3}{2}\pi\mu\frac{R_a}{h_0}\sqrt{\frac{R_a}{h_0}}\left(v_a - v_b\right) \tag{4.5}$$

where R_a is the radius of disk, h_0 is the fringe-to-fringe gap between two disks, μ is kinetic viscosity, v_a and v_b are the velocities along the normal direction of the two disks, respectively.

An extension of lubrication force for two non-equal disks was derived by Li et al. (2004), and they gave the formula of lubrication force as,

$$F_N^{\text{lub}} = -\frac{3}{2}\pi\mu\frac{1}{h_0}\frac{2R_aR_b}{R_a+R_b}\sqrt{\frac{1}{h_0}\frac{2R_aR_b}{R_a+R_b}}\left(v_a - v_b\right) \tag{4.6}$$

where R_a and R_b are the radii of two non-equal disks, respectively. If one of the solid surfaces is stationary (assuming disk "b" is stationary), then its velocity should be set as zero, and equation (4.6) becomes,

$$F_N^{\text{lub}} = -\frac{3}{2}\pi\mu v_a\frac{1}{h_0}\frac{2R_aR_b}{R_a+R_b}\sqrt{\frac{1}{h_0}\frac{2R_aR_b}{R_a+R_b}} \tag{4.7}$$

Equations (4.6) and (4.7) are available for dealing with the lubrication force for case 2. If we set $R_b \to \infty$, then equation (4.7) reduces to,

$$F_N^{\text{lub}} = -\frac{3}{2}\pi\mu v_a\frac{2R_a}{h_0}\sqrt{\frac{2R_a}{h_0}} \tag{4.8}$$

It is the lubrication force between a moving disk and a straight stationary wall, which is suitable for solving case 1. Now, we know the expression of lubrication force for case 1 and case 2. However, there is no available formula of lubrication force for case 3. In the next, we will derive the lubrication force for case 3.

The geometry of two non-equal disks at near distance for case 3 is shown in Fig. 4.4. We assume $h_0 << R_a < R_b$, the Reynolds number here is negligible, and the flow between two disks may be approximated as a Stokes flow. In a Stokes

flow, the analytical solution of lubrication force may be obtained by solving a simple Stokes equation,

$$\frac{dp}{dx} = \mu \frac{\partial^2 u}{\partial y^2} \tag{4.9}$$

If the velocity is decomposed into (*u, v*), where u is horizontal velocity, v is the vertical velocity, the boundary conditions can be written as,

$$\begin{cases} u = u_a + R_a \varpi_a, \ v = v_a, \ at \ y = h_a \\ u = 0, \ v = 0, \quad at \ y = -h_b \end{cases} \tag{4.10}$$

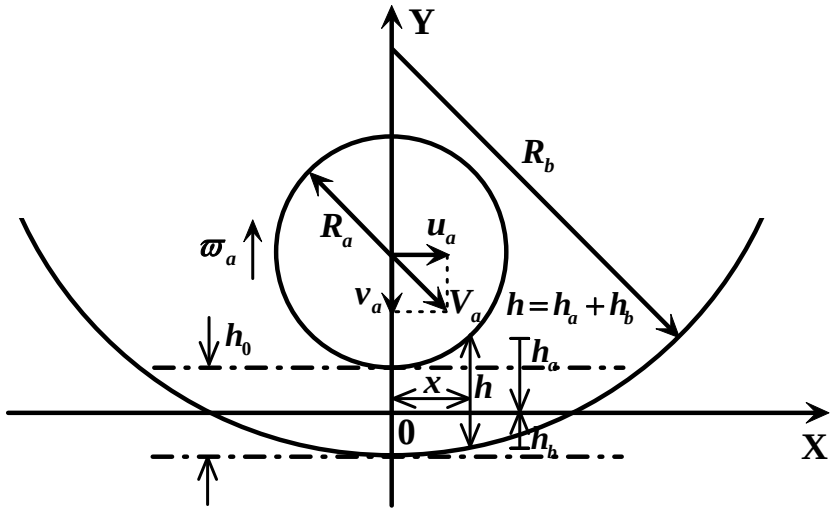

Figure 4.4 Geometry of two non-equal disks at near distance

For the incompressible flow of Newtonian fluid, the energy dissipation rate ϕ is simply defined as,

$$\phi = 2\mu \hat{D} : \hat{D} \tag{4.11}$$

where $\hat{D}$ is the deformation rate tensor of fluid element, and $\hat{D} \equiv \nabla \vec{u}$.

Because $v << u$ and $\partial u/\partial x << \partial u/\partial y$, then

$$\hat{D} : \hat{D} = \frac{\partial v_j}{\partial x_i} \frac{\partial v_j}{\partial x_i} = \left(\frac{\partial u}{\partial y} \right)^2 \tag{4.12}$$

The Rayleigh's dissipation function $\Re$, which is defined as one-half of the rate of energy dissipation in the fluid region V, may be obtained by integration of the local dissipation rate over individual fluid region V',

$$\Re = \frac{1}{2}\int_V \phi dV' = \frac{1}{2}\int_V 2\mu\left(\frac{\partial u}{\partial y}\right)^2 dV' = \frac{1}{2}\mu\int_{-\infty}^{\infty} dx\int_{-h_b}^{h_a}\left(\frac{\partial u}{\partial y}\right)^2 dy \tag{4.13}$$

The lubrication force may be obtained by the straightforward derivative of Rayleigh's dissipation function,

$$F_i = -\partial\Re/\partial v_i \tag{4.14}$$

To get the lubrication force, the most important step is to get $\partial u/\partial y$. In the next, we aim at obtaining $\partial u/\partial y$ by equations (4.9)-(4.10). From the geometry, we can get the gap h by using the Taylor's expansion in second order,

$$h = h_b + h_a = h_0 + \left(R_a - \sqrt{R_a^2 - x^2}\right) - \left(R_b - \sqrt{R_b^2 - x^2}\right) \approx h_0\left(1 + \frac{x^2}{h_0}\frac{R_b - R_a}{2R_aR_b}\right) \tag{4.15}$$

By integrating on the Stokes equation (4.9), and substituting the boundary conditions equation (4.10) into the result, we can get the horizontal velocity u as,

$$u = \frac{1}{2\mu}\frac{dp}{dx}\left(y'^2 - \frac{1}{4}h^2\right) - \frac{c_1}{h}y' - \frac{c_1}{2} \tag{4.16}$$

where $y' = y + \dfrac{h_a - h_b}{2}$, and $c_1 = -(u_a + R_a\varpi_a)$.

Then the fluid flux can be calculated by,

$$Q = \int_{-h_b}^{h_a} u dy = \int_{-\frac{h}{2}}^{\frac{h}{2}} u dy' = -\frac{1}{12\mu}\frac{dp}{dx}h^3 - \frac{c_1}{2}h \tag{4.17}$$

On the other hand, since there is a relative velocity between disks, the gap h can also be expressed as a function of time t, that is

$$h = v_a \cdot t + h_0 + \left(R_a - \sqrt{R_a^2 - x^2}\right) - \left(R_b - \sqrt{R_b^2 - x^2}\right) \tag{4.18}$$

Therefore, the volume of fluid between two solid interfaces from 0 to x is,

$$V(t) = \int_0^x h dx = v_a t x + h_0 x + (R_a - R_b)x - \int_0^x \left(\sqrt{R_a^2 - x^2} - \sqrt{R_b^2 - x^2}\right) dx \tag{4.19}$$

The Stokes equation (4.9) is linear, so the relationship between fluid velocity and fluid flux is also linear, and the fluid flux can be obtained by,

$$Q = -\partial V(t)/t = -v_a \cdot x + Q_0(u_a, \varpi_a) \tag{4.20}$$

By comparing equation (4.17) with equation (4.20), we can get dp/dx, and then insert dp/dx into equation (4.16), we can finally get $\partial u/\partial y'$ as follows,

$$\frac{\partial u}{\partial y'} = \left(12 v_a \frac{x}{h^3} - 6c_1 \frac{1}{h^2} - 12 Q_0 \frac{1}{h^3}\right) y' - c_1 \frac{1}{h} \tag{4.21}$$

By inserting equation (4.21) into equation (4.13), we can get

$$\begin{aligned} \Re &= \frac{1}{2}\int_V \phi dv = \frac{1}{2}\mu \int_{-\infty}^{\infty} dx \int_{-\frac{h}{2}}^{\frac{h}{2}} \left(\frac{\partial u}{\partial y'}\right)^2 dy' \\ &= \frac{1}{2}\mu\pi \sqrt{\frac{1}{h_0}\frac{2R_aR_b}{R_b - R_a}} \left(4c_1^2 + 3c_1 Q_0 \frac{1}{h_0} - \frac{9}{2} Q_0^2 \frac{1}{h_0^2} + \frac{3}{2} v_a{}^2 \frac{1}{h_0}\frac{2R_aR_b}{R_b - R_a}\right) \end{aligned} \tag{4.22}$$

From equation (4.14), the normal lubrication force is obtained, that is

$$F_N^{\text{lub}} = -\frac{\partial \Re}{\partial v_a} = -\frac{3}{2}\pi\mu v_a \frac{1}{h_0}\frac{2R_aR_b}{R_b - R_a}\sqrt{\frac{1}{h_0}\frac{2R_aR_b}{R_b - R_a}} \tag{4.23}$$

Equation (4.23) is the formula of lubrication force for disk in case 3. If $R_b \to \infty$, this equation also reduces to the lubrication force for case 1. Up to now, we have known that equations (4.8), (4.5)-(4.7), and (4.23) are the expressions of lubrication force for case 1, case 2, and case 3, respectively. We rearrange these lubrication force equations as follows,

$$F_N^{\text{lub}} = -\frac{3}{2}\pi\mu\left(\frac{2R_{effective}}{\varepsilon}\right)^{3/2} v_{relative} \tag{4.24}$$

where ε is the distance between two surfaces, $R_{effective}$ is the effective radius, and $v_{relative}$ is the relative velocity between two surfaces. Here, for the case between a circulating cell and a stationary flat vessel, $R_{effective} = R_c$ and $v_{relative} = v_c$; for the case between two equal moving cells, $R_{effective} = R_c/2$ and $v_{relative} = v_{c1} - v_{c2}$; for the case between a circulating cell and a stationary positive curvature vessel, $R_{effective} = R_{c1}R_{c2}/(R_{c1} + R_{c2})$ and $v_{relative} = v_c$; and for the case between a moving cell and a stationary negative curvature vessel, $R_{effective} = R_{c1}R_{c2}/(R_{c1} - R_{c2})$ (assuming $R_{c1} > R_{c2}$) and $v_{relative} = v_c$, where R_c is the radius of circulating cell, and v_c is the velocity of cell. "1" refers to cell-1, and "2" refers to cell-2.

Ladd (1994) suggested that $1/\varepsilon$ should be replaced by $\left(1/\varepsilon - 1/\Delta_c\right)$, where Δ_c is the cutoff spacing for the lubrication force. If $\varepsilon \geq \Delta_c$, then $F_N^{\text{lub}} = 0$. If $\varepsilon < \Delta_c$, then the lubrication force should be calculated and added to the hydrodynamic force. Therefore, equation (4.24) can be rewritten as,

$$F_N^{\text{lub}} = -\frac{3}{2}\pi\mu\left[2R_{effective}\left(\frac{1}{\varepsilon} - \frac{1}{\Delta_c}\right)\right]^{3/2} v_{relative} \tag{4.25}$$

where $\Delta_c = 1$ is adopt in our simulations which also suggested by Ladd.

4.2 Repulsive van der Waals Force

There are colloidal nonspecific interactions between particle and substrate. In this thesis, we mainly consider the repulsive van der Waals force, which plays a central role in all phenomena involving intermolecular forces. In our simulations,

the repulsive van der Waals force is applied to prevent the boundaries of cell-cell and cell-substrate from overlapping. To quantitatively incorporate the van der Waals force into our simulations, we use the simple expression for this force that proposed by Bongrand and Bell (1984). In this model, the interaction potentials per area are given as mathematical functions of the separation distance. These expressions were originally derived for the case of two parallel surfaces. In our system, we should apply these expressions for several cases, including a cylinder and a flat surface, two equal cylinders, a cylinder and a positive curvature surface, and a cylinder and a negative curvature surface. We apply the Deryaguin approximation to integrate the potential over the cylinder surface and express these interactions as body forces (Israelachvili 1992). Since the separation distance is smaller than the radius of circulating cell and the interactions decay rapidly with distance, the Deryaguin approximation is valid in our cases.

The repulsive van der Waals interaction free energies between bodies of different geometries were calculated on the basis of Hamaker summation method (Hamaker 1937). A typical case is that the repulsive van der Waals interaction free energy between two parallel cylinders which is sketched in Fig. 4.5. The interaction free energy $W(\varepsilon)$ for two parallel cylinders is,

$$W(\varepsilon) = \frac{AL}{12\varepsilon^{3/2}} \left(\frac{R \cdot R_c}{R + R_c} \right)^{1/2} \tag{4.26}$$

where R and R_c are the radii of two cylinders, L is the height of cylinders, ε is the separation distance between two surfaces, and A is the Hamaker constant.

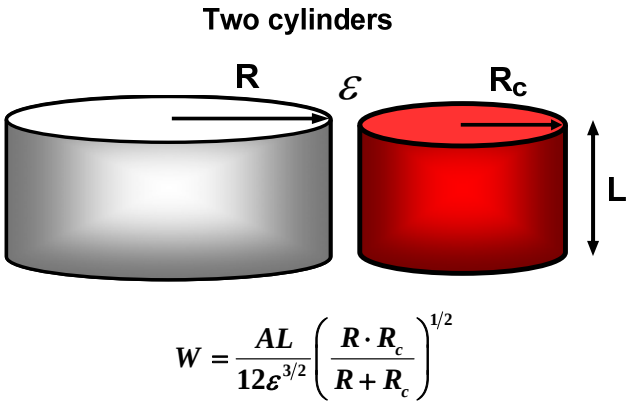

Figure 4.5 Van der Waals interaction energy between two cylinders

So far we have known the interaction free energy between two parallel cylinders. Now, it is desirable to relate the force law between two curved surfaces. From the expression of interaction free energy $W(\varepsilon)$, the force $F(\varepsilon)$ can be obtained by taking the derivative of $W(\varepsilon)$, i.e. $\vec{F}_v = -\partial W(\varepsilon)/\partial\varepsilon$. Therefore, the repulsive van der Waals force can be expressed as,

$$\vec{F}_V = \frac{A \cdot L_{thickness}}{8\sqrt{2}} \sqrt{\frac{R_{effective}}{\varepsilon^5}} \tag{4.27}$$

where $R_{effective}$ is the effective radius, and $L_{thickness}$ is the thickness of the cell. Equation (4.27) can be extended to other geometries: (1) for the case between a circulating cell and a straight vessel, $R_{effective} = R_c$, where R_c is the radius of cell; (2) for the case between two equal cells, $R_{effective} = R_c/2$; (3) for the case between a circulating cell and a positive curvature vessel, $R_{effective} = R \cdot R_c/(R + R_c)$, where R is the radius of curved vessel; and (4) for the case between a circulating cell and a negative curvature vessel, $R_{effective} = R \cdot R_c/(R - R_c)$ (assume $R > R_c$).

Although the formula of repulsive van der Waals force is similar to that of lubrication force, the fundamental principles of these two forces are totally

different. The lubrication force occurs only when the distance between two surfaces is within one lattice spacing. Only in this situation, it should be calculated and added to the hydrodynamic force to make up the lost force. However, the repulsive van der Waals force is always present, and it is the colloidal nonspecific interaction force between solid surfaces.

4.3 Spring Force

The spring force is induced by the adhesive springs which are idealized from the receptor-ligand bonds. In cell adhesion, the adhesive dynamics models and the stochastic Monte Carlo method play important roles in determining whether a bond is formed or not and whether a bond is broken or still keep bound. Once the bound bonds are known, the spring force can be calculated via the compression and expansion of bonds. The adhesive dynamics models and the stochastic Monte Carlo approach have been introduced in chapter 2. In the next, we will present how to get the spring force at each time step based on the knowledge in chapter 2. The following steps should be performed:

Firstly, we calculate the association and dissociation rates of the bond according to equations (2.1) (2.2) or (2.4) (2.5).

Secondly, we compute the probability of forming a bond and the probability of breaking a bond in a time interval based on equations (2.6) (2.7) or equations (2.8) (2.9) (2.10).

Thirdly, we carry out the stochastic Monte Carlo calculation, and compare the random numbers with the formation and breakage probabilities. If the chosen

random numbers are inferior to the probabilities, then the events of forming or breaking a bond will happen at the next time step.

Finally, we calculate the forces of every individual bond according to equation (2.3), and then obtain the total spring force by the summation of all these forces. The formula of the total spring force is expressed as follows,

$$\vec{F}_s = \sum_{i=1}^{n} \sigma\left(\chi_i - \lambda\right) \tag{4.28}$$

where n is the total number of bonds at each time step.

4.4 Cell Dynamics

The technique used for cell dynamics is based on the approach of Aidun et al. (1998) for impermeable particle suspensions with inertia and any solid-to-fluid density ratio, which is an improvement over the original algorithm proposed by Ladd (1994). This method solves the LBE for the fluid phase and couples with the Newtonian rotation and translation of solid particles suspended in the fluid through solid-fluid interactions. In cell adhesion, the circulating cell also follows Newton's law of rotation and translation,

$$\frac{d\vec{u}_c}{dt} = \frac{\vec{F}_c}{m}; \quad \frac{d\omega_c}{dt} = \frac{T_c}{I} \tag{4.29}$$

where $\vec{u}_c$ is the velocity of the cell, ω_c is the angular velocity, $\vec{F}_c$ is the total force, T_c is the total torque, m is the mass, I is the inertia, dt is the time step. $\vec{F}_c = \vec{F}_h + \vec{F}_v + \vec{F}_s$, where $\vec{F}_h$ is the hydrodynamic force, $\vec{F}_v$ is the repulsive van der Waals force, and $\vec{F}_s$ is the total spring force. $T_c = T_h + T_s$, where T_h and T_s are the

torques induced by the hydrodynamic force and spring force, respectively. At each iteration, the position $\vec{x}_c$ and rotational angle θ_c of cell are determined by,

$$\frac{d\vec{x}_c}{dt} = \vec{u}_c \,; \quad \frac{d\theta_c}{dt} = \omega_c \tag{4.30}$$

For the purpose of computation stability, a "leap-frog" algorithm, which has been widely applied in molecular dynamics (MD) and proved to be of second order accuracy (Allen and Tildesley 1987), is adopted to update the position, velocity, angular velocity and angle of the cell with the increment of time,

$$\vec{u}_c(t+\frac{1}{2}\delta t) = \vec{u}_c(t-\frac{1}{2}\delta t) + \frac{\vec{F}(t)}{m}\delta t \tag{4.31}$$

$$\vec{x}_c(t+\delta t) = \vec{x}_c(t) + \vec{u}_c(t-\frac{1}{2}\delta t)\delta t + \frac{\vec{F}(t)}{m}\delta t^2 \tag{4.32}$$

$$\omega_c(t+\frac{1}{2}\delta t) = \omega_c(t-\frac{1}{2}\delta t) + \frac{T(t)}{I}\delta t \tag{4.33}$$

$$\theta_c(t+\delta t) = \theta_c(t) + \omega_c(t-\frac{1}{2}\delta t)\delta t + \frac{T(t)}{I}\delta t^2 \tag{4.34}$$

where δt is the time step in Newtonian motion.

In simulating moving cell, on the one hand, some fluid nodes can be covered by the moving cell (solid nodes), so the fluids at these solid nodes must be removed from the fluid system. On the other hand, when a fluid node previously occupied by a cell (solid node) and now is recovered, the fluid density at this newly created node should be included in the fluid system again. The distribution function at these new fluid nodes is assumed the average of the extrapolated values from a second order extrapolation scheme of all the possible directions to approximately satisfy the mass conservation at boundaries (Chen and Martinez

1996). For example, assuming $\vec{x}_b$ is changed from solid node to fluid node, the distribution function at $\vec{x}_b$ can be calculated by the extrapolation scheme, that is

$$f_i(\vec{x}_b) = \frac{\sum_j \left(2 f_i(\vec{x}_b + \vec{e}_j) - f_i(\vec{x}_b + 2\vec{e}_j)\right)}{N} \tag{4.35}$$

where $(\vec{x}_b + \vec{e}_j)$ and $(\vec{x}_b + 2\vec{e}_j)$ are usually the fluid nodes. In some special situation, i.e., $(\vec{x}_b + \vec{e}_j)$ is the fluid node, but $(\vec{x}_b + 2\vec{e}_j)$ is the solid node, the distribution function at $\vec{x}_b$ is not extrapolated but directly replaced by the distribution function at $(\vec{x}_b + \vec{e}_j)$. Here, N is the number of sum.

4.5 Dimensional Transformation

In lattice Boltzmann simulation, we should know the transformation between the real physical quantities and the discrete lattice quantities, and this process is called as dimensional transformation. Assuming the letters with superscript represent the lattice quantities and these without superscript stands for the real physical quantities. We assume L', T', and G' are the lattice length, evolution time, and mass; and L, T, and G are the real physical length, time, and mass, respectively. If we set the cell diameter as D, the fluid viscosity as υ, and the fluid density as ρ, then we can get,

$$D = D'L; \quad \upsilon = \upsilon' \frac{L^2}{T}; \quad \rho = \rho' \frac{G}{L^3} \tag{4.36}$$

where D' is the lattice cell diameter, υ' is the lattice fluid viscosity, and ρ' is the lattice fluid density. From equation (4.36), we can obtain the basic mechanical quantities in international unit by,

$$L=\frac{D}{D'};\ T=\frac{\upsilon'}{\upsilon}\left(\frac{D}{D'}\right)^2;\ G=\frac{\rho}{\rho'}\left(\frac{D}{D'}\right)^3 \tag{4.37}$$

For example, $D=10\ \mu$m , $D'=20$, $\upsilon=1.2\times10^{-6}$ m^2/s, $\upsilon'=1/12$, $\rho=1.05$ g/cm^3, $\rho'=1$. From equation (4.37), we can get: $L=0.5\times10^{-6}$ m, $T\approx1.74\times10^{-8}$ s, and $G=1.31\times10^{-16}$ kg. It means that the every lattice length is $0.5\times10^{-6}m$, every time step in lattice is $1.74\times10^{-8}s$, and one mass unit in lattice is 1.31×10^{-16} kg. Based on equation (4.37), we can know all the transformations between real physical quantities and lattice quantities, such as,

Time: $$t=t'T \tag{4.38}$$

Length: $$l=l'L \tag{4.39}$$

Velocity: $$v=v'\frac{L}{T}=v'\frac{\upsilon}{\upsilon'}\frac{D'}{D} \tag{4.40}$$

Acceleration: $$a=a'\frac{L}{T^2}=a'\left(\frac{\upsilon}{\upsilon'}\right)^2\left(\frac{D'}{D}\right)^3 \tag{4.41}$$

Mass: $$m=m'G=m'\frac{\rho}{\rho'}\left(\frac{D}{D'}\right)^3 \tag{4.42}$$

Force: $$F=F'G\frac{L}{T^2}=F'\frac{\rho}{\rho'}\left(\frac{\upsilon}{\upsilon'}\right)^2 \tag{4.43}$$

Pressure: $$p=p'\frac{G}{LT^2}=p'\frac{\rho}{\rho'}\left(\frac{D'}{D}\right)^2\left(\frac{\upsilon}{\upsilon'}\right)^2 \tag{4.44}$$

Fluid flux: $$Q=Q'\frac{L^3}{T}=Q'\frac{\upsilon}{\upsilon'}\frac{D}{D'} \tag{4.45}$$

It is worth mentioning that the lattice fluid viscosity υ' in the D2Q9 lattice Boltzmann model is $\upsilon'=\frac{1}{6}(2\tau-1)$, where τ is the non-dimension relaxation time. In our simulations, we choose τ as 0.75.

4.6 Summary

In this chapter, we mainly focus on the evaluation of hydrodynamic force, repulsive van der Waals force, and spring force. These forces act on the cell and govern the cell adhesion and migration under blood flow condition. Once these forces are known, the calculation of cell dynamics can be carried out based on the Newton's law of translation and rotation. We also present the dimensional transformation between the real physical quantities and the lattice quantities in the simulations.

Up to now, the research methodologies, including the adhesive dynamics models (chapter 2), blood dynamics (chapter 3), and cell dynamics (chapter 4), are all introduced in detail. Now, let us briefly summarize the computational steps in performing cell adhesion and motion at each time step.

Step 1. Calculate the external forces that acting on the cell.

Step 2. Check for the formation and breakage of the bonds.

Step 3. Update the position and angle of the cell in blood flow.

Step 4. Update the lengths of the bound microvilli.

With the end of step 4, the time is updated and the process is repeated until the end of the simulation.

Chapter 5

Effects of Curvature and Cell-Cell Interaction on Cell Adhesion in Micro-vessels

It has been found that both the circulating blood cells and tumor cells are more likely adherent to the curved micro-vessels than the straight ones (Liu et al. 2008; Lv et al. 2007). This inspired us that the vessel curvature could influence cell adhesion in the curved vessels. Since the blood flow always involves multiple circulating cells, it is understandable that the interaction of cells would also affect cell adhesion and migration in the blood vessels. In this chapter, we aim at numerically studying the effects of vessel curvature and cell-cell interaction on cell adhesion in micro-vessels. In this study, the fluid dynamics was solved by the LBM, the cells dynamics was governed by the Newton's law of translation and rotation, and the adhesive dynamics model with the Dembo et al.'s model of forward/reverse reaction rates was involved to take into account the effect of receptor-ligand bonds on cell adhesion. Firstly, a single cell suspension in a 2-D symmetric stenotic micro-vessel was carried out to validate the accuracy of numerical scheme, and then both the single cell adhesion and double cells adhesion in either the straight or curved micro-vessels were studied in detail.

5.1 Cell Suspension in the Symmetric Stenotic Micro-vessel

To evaluate the accuracy of present numerical scheme, a cell suspension flow with the curved geometries is firstly carried out in a 2-D stenotic micro-vessel. This

kind of cell suspension flows through stenosis vessels are of great interest in medical science. There are many papers on the study of pulsatile flow in a mildly or severely stenotic vessel. A typical work has been numerically done by Li et al. (2004) by using the LBM.

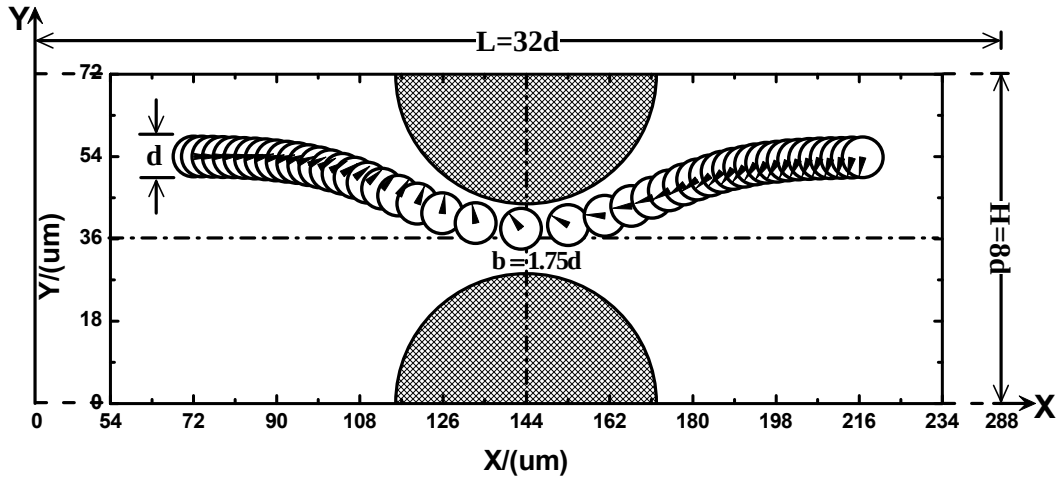

Figure 5.1 The geometry of stenotic vessel and the snapshots of positions and rotation angles of the circulating cell

As shown in Fig. 5.1, the geometry of the stenotic micro-vessel is designed as a 2-D planar blood vessel with the length $L = 32d = 288$ μm and the height $H = 8d = 72$ μm, where $d = 2R_c$ is the diameter of the moving cell. We also use a cell of radius $R_c = 4.5$ μm, a typical size of the circulating leukocytes and tumor cells in the blood vessel. The stenosis is established by adding two symmetric protuberances inside the vessel. The protuberance is a semicircle with the radius determined by the width of stenosis throat *b*, where $b = 1.75d$. The cell is initially placed in the left of stenosis throat at (8*d*, 6*d*), and it will move through the stenosis throat towards the outlet due to the force and torque acting on it. The pressure difference Δp between the inlet and outlet is set as 400 Pa.

The snapshots of positions and rotation angles of the cell with respect to the traveling time and *x*-axis are also illustrated in Fig. 5.1. It can be seen that the cell moves towards the centerline when it gets near and across the protuberance, but it never arrives at the centerline of the vessel. After passing the stenosis, the cell migrates up to the same height of the initial position, of which 2*d* above the centerline. This result is consistent with the Segre´-Silberberg effect (Segre´ and Silberberg 1961) observed in the flat pipe flow that neutrally buoyant cylinders migrate laterally away from both the wall and the centerline and reach a certain lateral equilibrium position.

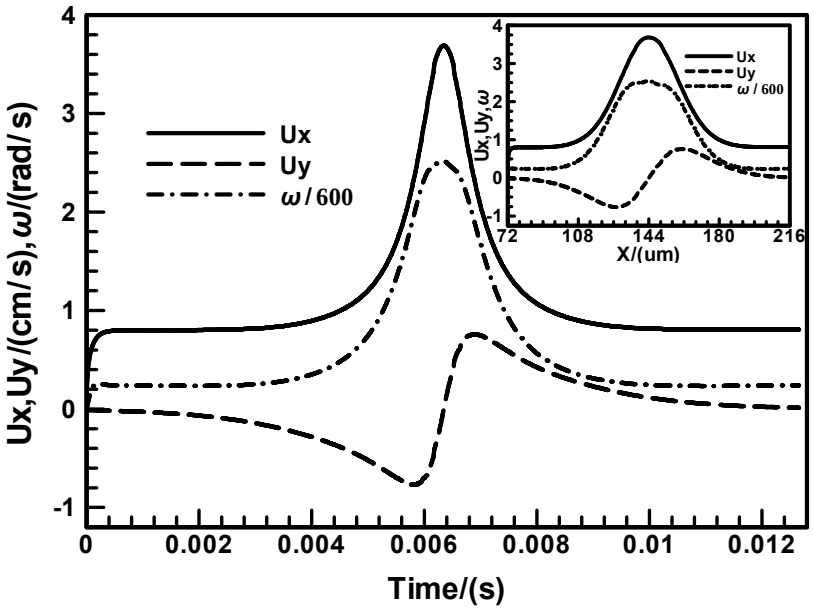

Figure 5.2 The velocity and angular velocity of the circulating cell against the traveling time and x-axis

Fig. 5.2 shows the *x*, *y* component of velocity and angular velocity of the circulating cell with respect to the traveling time and *x*-axis value (inset figure). The *x* component velocity at the stenosis throat reaches a peak, with which the

amplitude is almost five times of that in the straight part of the vessel. The y component velocity changes its direction at the stenosis throat. The trend of angular velocity is similar to that of x component velocity. It shows that the cell rotates more quickly at the stenosis throat than that in the flat vessel. All the observations are the same as that reported by Li et al. (2004).

In this cell suspension flow, the hydrodynamic force and repulsive van der Waals force govern cell motion in the whole journey. Generally speaking, the critical length for bond formation is only 40 nm. Since the distance between the circulating cell and vessel wall is superior to the critical length, there is no spring force involved in this cell migration. Therefore, this cell suspension flow can be used to validate the cell migration without cell adhesion under flow condition.

5.2 Effect of Vessel Curvature on Cell Adhesion in Micro-vessels

To evaluate the effect of vessel curvature on cell adhesion, the adhesion of single cell in both the straight and curved micro-vessels is carried out. The schematic views of the 2-D straight and curved micro-vessels are shown in Fig. 5.3(a)-(b), respectively. The length of the straight micro-vessel is $L = 224\ \mu m$ and the height is $D = 14\ \mu m$. The curved micro-vessel is design as follows: the curved vessel of diameter $D = 14\ \mu$m starts with a straight segment and then a negatively bent segment of $\pi / 3$ bending angle, with the inner curvature radius of $28\ \mu$m and the outer radius of $42\ \mu$m, following with a positively curved segment with the inner and outer radii of $42\ \mu$m and $56\ \mu$m, respectively. The right half of the vessel is symmetric to the left half with the total vessel length of $L = 224\ \mu$m. The radius

of the circulating cell is set as $R_c = 4.5\,\mu\text{m}$. The ratio of the cell diameter to the vessel diameter is about 0.64. The cell is initially placed near the inlet, and driven by a pressure difference Δp between the inlet and the outlet. The parameters and their values are tabulated in Table 5.1. Here, three different time-steps are involved in the simulations: (1) the time-step of 10^{-6}s is applied to check the bond formation and breakage in the adhesive dynamics model; (2) the lattice Boltzmann relaxation time τ is 1, corresponding to a time-step of 3.6×10^{-8}s is used to update the flow filed; and (3) the time-step of 1.2×10^{-9}s is adopted to update the cell migration in the Newtonian motion. The use of these three time-steps maintains the accuracy in the program while also permitting shorter run times. Since the flow speed in the capillaries or micro-vessels is very low (in the order of 1.0 mm/s), the effect of pulsating blood flow on cell adhesion would be very inconspicuous, and therefore it is neglected in our simulations.

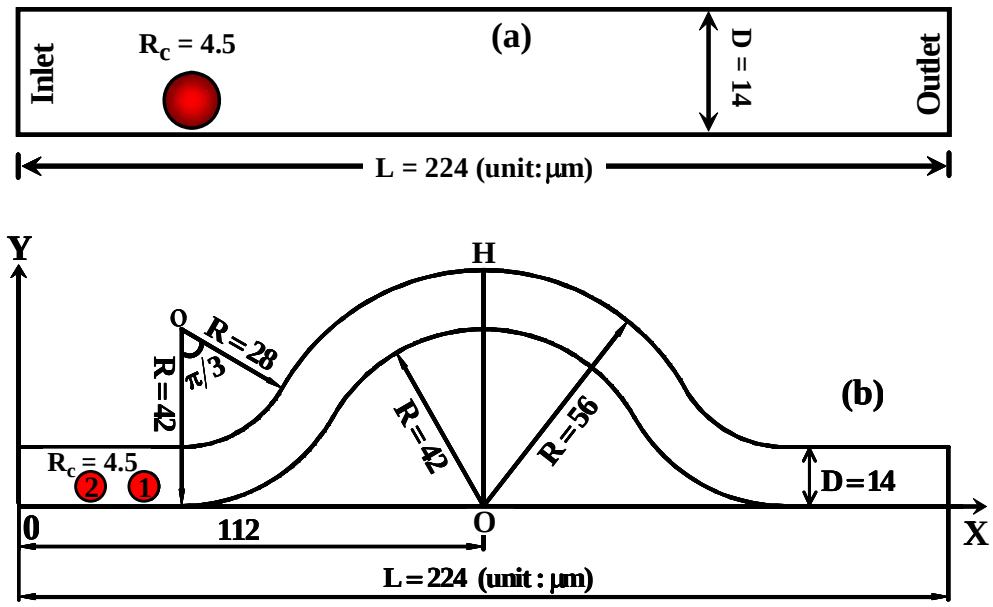

Figure 5.3 Schematic views of the straight vessel (a) and curved vessel (b).

Table 5.1 Simulation parameters and values

Parameter	Definition	Value (Reference)
R_c	cell radius	4.5 μm (Ref.[1])
H_c	critical length for bond formation	40 nm (Ref.[2])
ρ_f	plasma density	1.03 g/cm^3 (Ref. [3])
T	Temperature	310 K (Ref. [2])
λ	equilibrium bond length	20 nm (Ref. [2])
ν	plasma kinetic viscosity	1.2×10^{-6} m^2/s (Ref. [3])
σ	spring constant	47/ μm^2 (Ref. [4])
k_b	Boltzmann constant	1.38×10^{-23} J/K
k_f^0	intrinsic forward reaction rate	10^{-2} /s (Ref. [5])
k_r^0	intrinsic reverse reaction rate	10^{-2} μm^2 / s (Ref. [5])
σ_{ts}	transition state spring constant	10^{-3} N / m (Ref. [5])
N_r	receptor density	2×10^{-3} N / m (Ref. [4])

Ref. [1]: Brunk et al. 1997

Ref. [2]: Chang et al. 2000

Ref. [3]: Skalak and Chien 1987

Ref. [4]: Chang and Hammer 1996

Ref. [5]: Dembo et al. 1988

5.2.1 Single Cell Adhesion in the Straight Micro-vessel

To further validate the accuracy of numerical scheme that coupled the adhesive dynamics model into the LBM, the adhesion of single cell in the straight micro-vessel is firstly examined. The validation problem is similar to that of Migliorini et al. (2002), but the pressure drop is set as 1.5 Pa. Then, the statistics of hydrodynamic normal force, tangential force, torque, and cell rolling velocity between the present result and other available data are tabulated in Table 5.2. From the table, it can be found that our calculation is within the range of other available results.

To study the influence of vessel curvature on cell adhesion, the single cell adhesion is carried out in the straight micro-vessel (as shown in Fig. 5.3(a)). To form receptor-ligand bonds easily, the cell is arranged near the wall of the vessel at the entrance. Once the distance between the end points of a receptor and a ligand is within the critical length H_c, the cell movement would be influenced by the stochastic interactions between receptors and ligands. Here, the pressure difference Δp between the inlet and outlet is set as 11.2 Pa (0.05 Pa / μm).

Fig. 5.4 shows the history of single cell location and movement in the straight vessel with adhesion ($\vec{F}_s \neq 0$) and without adhesion ($\vec{F}_s = 0$). Fig. 5.4(a) shows the trajectory of the cell, which indicates a rolling effect of the cell due to cell adhesion. Figs. 5.4(b)-(c) show the velocity and angular velocity of the circulating cell, respectively. Compared to the velocity of non-adhesion case, the adhesion effect is obvious. At the entrance, the cell moves in the vessel with a

constant velocity at about 940 μm/s, a normal velocity in this type of vessels, indicating that the cell in this period is unattached. Then the velocity suddenly drops down to 800 μm/s, suggesting that the bond is being formed. After that point, the velocity experiences several fluctuations between 800 and 850 μm/s and keeps almost stationary fluctuating. The variation of angular velocity is very similar to that of the velocity. The angular velocity without adhesion is about 8.5 rad/s clockwise. For the adhesion case, it fluctuates between 60 and 80 rad/s clockwise. Therefore, the adhesion enhances the cell rolling.

Figure 5.4(d) shows the history of how many bonds formed during the cell migration process. The higher number of bonds means there is higher opportunity for a cell to be caught by the vessel wall. After off and on interactions between the circulating cell and ECs, the steady bonds are formed throughout the journey, which are represented by the black band in the figure. Most of the bonds number fluctuates between 1 and 8 and very few reaches up to 10. These receptor-ligand bonds result in the velocity and angular velocity oscillation as described in Figs. 5.4(b)-(c).

Table 5.2 Validation results

Physical quantity	**Present result**	**Literature data (reference)**
Normal force/(pN)	0.32	0.27-1.8 (Ref. [1, 2])
Tangential force/(pN)	65.23	45-450 (Ref. [3, 4, 5])
Torque/(pN×μm)	207.9	140-180 (Ref. [2, 3, 5])
Pressure drop/(Pa)	1.5	1.2-4.5 (Ref. [2, 4, 5])
Cell velocity/(μm/s)	163.65	25-225 (Ref. [2, 6])

Ref. [1]: Blackshear et al. 1991

Ref. [2]: Migliorini et al. 2002

Ref. [3]: Goldman et al. 1967

Ref. [4]: Chapman and Cokelet 1997

Ref. [5]: Graver and Kute 1998

Ref. [6]: Munn et al. 1996

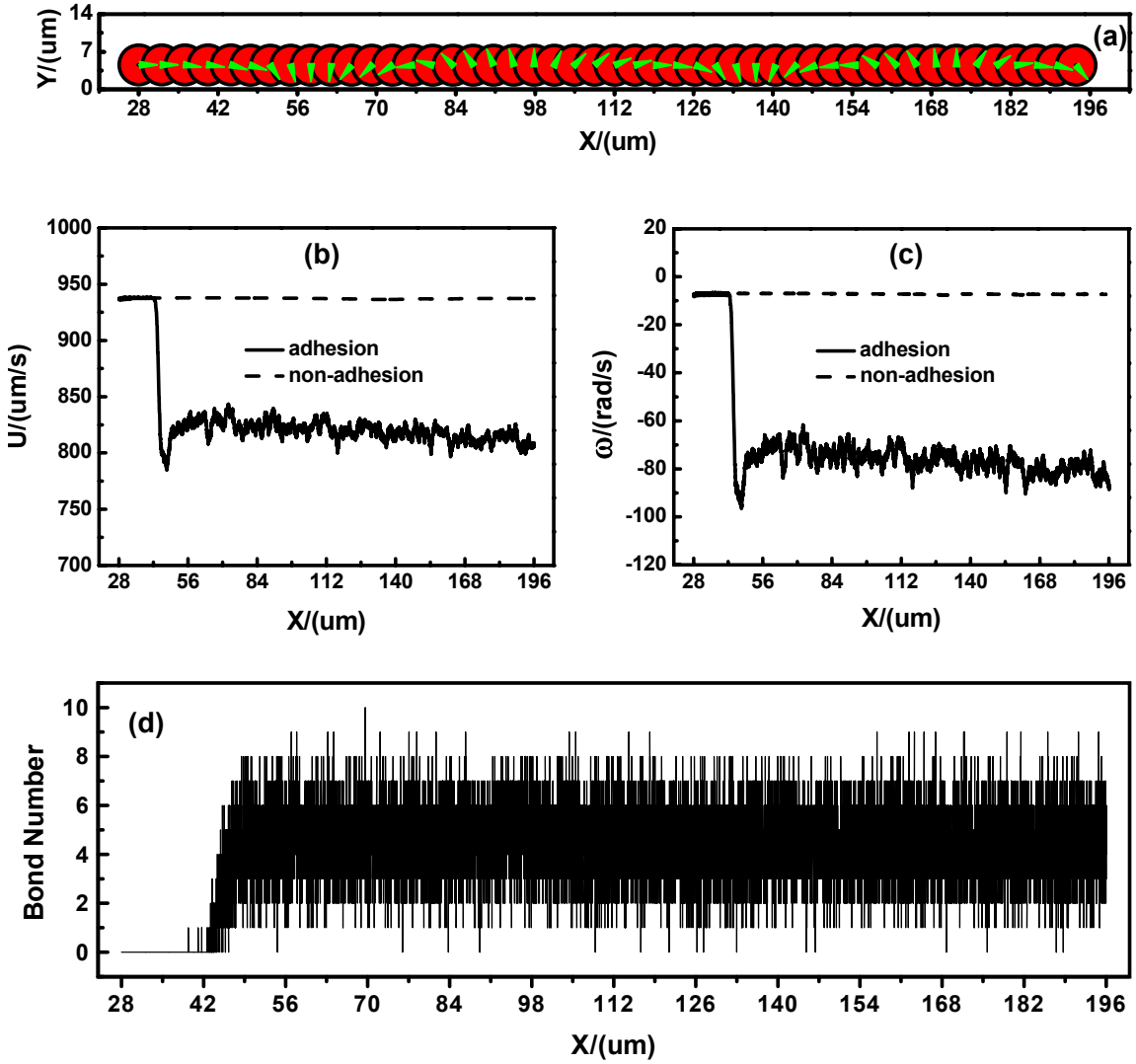

Figure 5.4 The history of single cell with adhesion and non-adhesion in the straight micro-vessel: (a) trajectory, (b) velocity, (c) angular velocity, and (d) number of bonds

5.2.2 Single Cell Adhesion in a Curved Micro-vessel

For a single cell travels in the curved micro-vessel, the initial position of cell is set the same as that in the straight vessel. The pressure drop Δp between the inlet and outlet is set as 12.75 Pa ($0.05\,\text{Pa}/\mu\text{m}$), i.e., the same pressure drop per unit length as that in a straight micro-vessel.

The history of cell motion with both adhesion and non-adhesion in the curved vessel is illustrated in Fig. 5.5. From Fig. 5.5(a), one can find that the cell translates and rotates around the curvature, and the total rotation angle is more than 4π, almost the same as that in the straight vessel. Figs. 5.5(b)-(c) show that the effect of adhesion on velocity and angular velocity is not as significant as that in the straight vessel. The velocity is averaged over $20\,\mu\text{s}$ using a moving average algorithm. Compared to the case of without adhesion, both the velocity and angular velocity profiles with adhesion generally follow that of non-adhesion at the entrance of a curved vessel, but they are lower and fluctuating strongly due to the cell adhesion effect in the negative curvature vessel.

Fig. 5.5(d) shows the history of bonds number in the whole journey. It is clearly shown that the bonds start to form at the entrance of the straight part of curved vessel, and all the bonds are broken up at about $x = 70\,\mu\text{m}$, at which the fluid has brought the cell off the vessel wall. At the same location, the cell velocities of both with and without adhesion jump up as shown in Fig. 5.5(b), indicating that the hydrodynamic force is dominant. During the binding period, the number of bonds fluctuates between 1 and 9, and a few reaches up to 10.

Moreover, the cell adhesion only takes place at the entrance of the straight and negative curvature vessel, once leaving the negative curvature vessel, the cell moves as a free cell, and there is no cell adhesion in the positive curvature vessel at all. Therefore, it can be concluded that the vessel curvature has significant influence on cell adhesion.

To compare the probability of cell adhesion between the straight and curved micro-vessels, the statistics of bonds number are calculated, and the probability of each bond number occurring and the ratio of these two probabilities are presented in Fig. 5.6. It can be found that, for the smaller bonds number, the probability in the straight vessel is larger than that in the curved vessel, and the turning point is at bonds number being 5 with the probability of 25.5%. For the larger bonds number, i.e. the bonds number larger than 5, the probability in the curved vessel is obviously higher than that in the straight vessel, and the larger the bonds number, the higher the probability in the curved vessel. It is understandable that the final cell adhesion depends on the number of bonds, the more the simultaneous bonds form, the higher probability the cell is adhered to the vessel wall.

Since we use the stochastic Monte Carlo method to calculate the receptor-ligand binding to evaluate the statistical significance, we calculate three cases for the curved micro-vessel under the same conditions. It is found that the relative discrepancy is within 5%, as shown in Fig. 5.7.

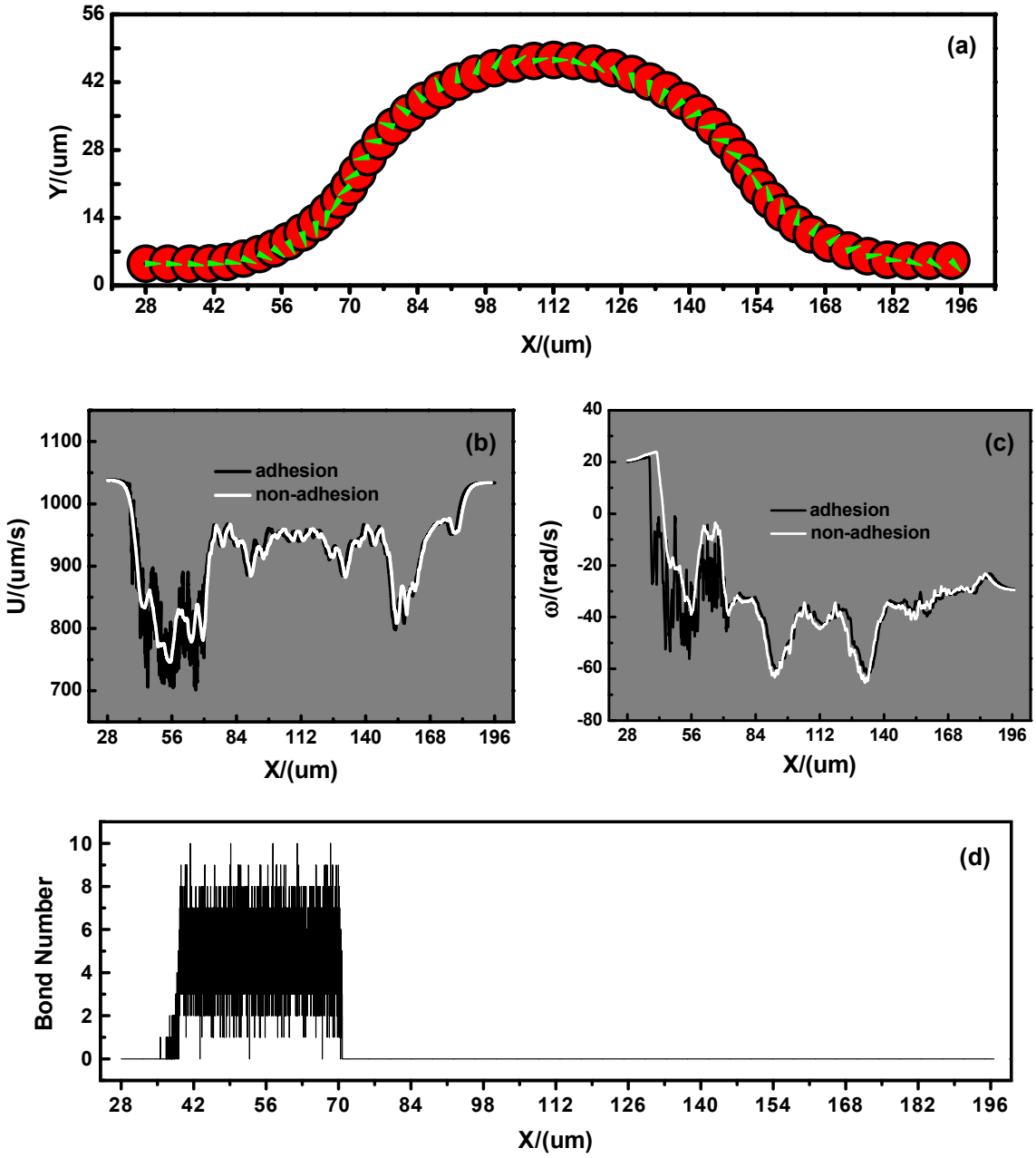

Figure 5.5 The history of single cell with adhesion and non-adhesion in the curved micro-vessel: (a) trajectory, (b) velocity, (c) angular velocity, and (d) number of bonds

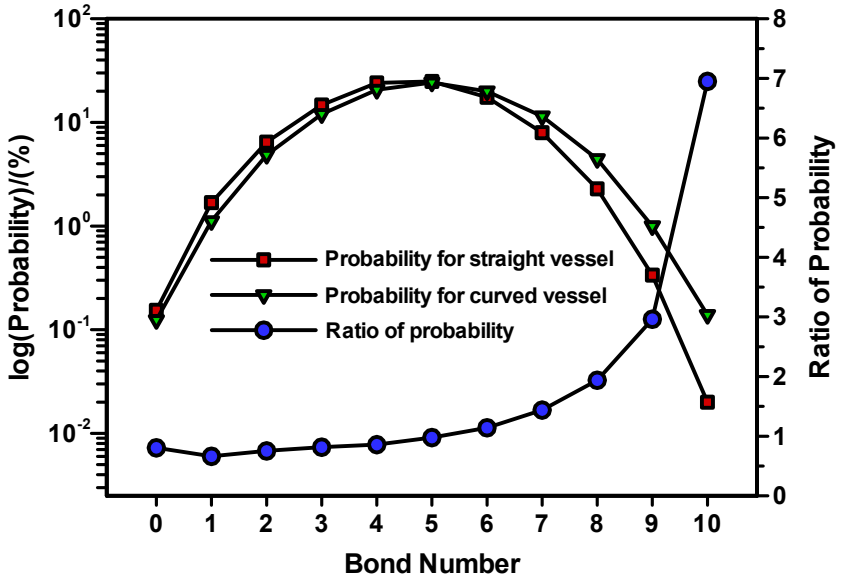

Figure 5.6 Comparison of bond formation probabilities and the ratio of these probabilities between the straight and curved micro-vessel.

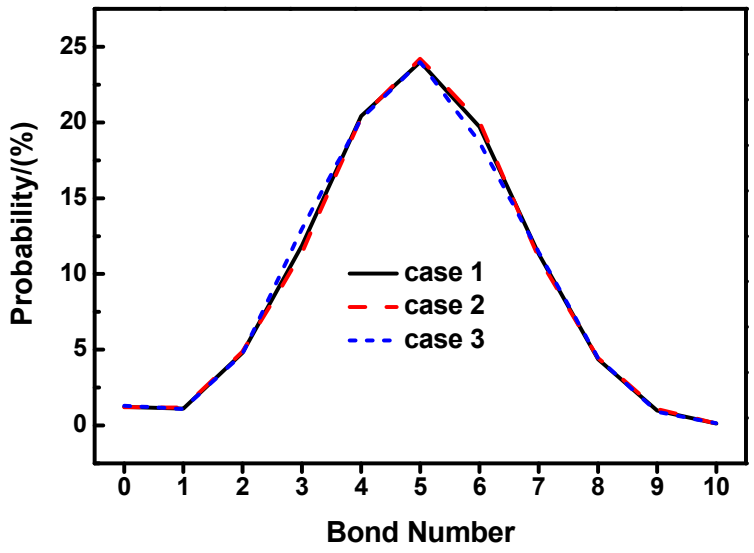

Figure 5.7 Comparison of bond formation probabilities in the curved micro-vessel under the same condition.

5.3 Effect of Cell-Cell Interaction on Cell Adhesion in Micro-vessels

The blood flow always involves multiple cells, and the interaction of the cells would affect the cell adhesion and migration. For simplicity, we investigate two cells motion in both the straight and curved vessels. Here, cell-1 is initially placed in the same position as the single cell, and cell-2 is placed $0.5R_c$ behind the cell-1, both of which have been displayed in Fig. 5.3.

5.3.1 Adhesion and Interaction of Two Cells in the Straight Micro-vessel

First of all, the effect of cell-cell interaction on cell adhesion is implemented in the straight vessel. The pressure drop Δp is set as 11.2 Pa ($0.05\,\mathrm{Pa}/\mu\mathrm{m}$), the same as that of a single cell in the straight vessel.

The history of the two cells' motion in the straight vessel is displayed in Fig. 5.8. The relative position of these two cells at different time is shown in Fig. 5.8(a). The spacing between two cells becomes bigger and bigger, and the variation of the spacing with time is shown in the inset figure. The history of vertical spacing between the center of cell and wall is shown in Fig. 5.8(b). The cell-1 moves away from the critical length, therefore it is difficult for cell-1 to form bonds during the journey. However, the spacing between cell-2 and the wall becomes smaller and smaller, and cell adhesion is expected to occur. Fig. 5.8(c) shows the history of velocity for both cells. The cell-1 moves in an almost constant velocity, but the velocity of cell-2 decreases and fluctuates due to the adhesion effect. Figs. 5.8(d)-(e) clearly show the cell rotations and adhesion effects. The rotation speed of cell-1 is almost flat since there is no adhesion

occurring. For cell-2, the angular velocity fluctuates apparently due to the cell adhesion effect. Generally, the cell-1 would travel away from the wall under the interaction of cell-2, instead, cell-2 would experience significant adhesive processes.

Fig. 5.8(f) shows the history of bonds number of cell-2. Due to the interaction with cell-1, the bonds number of cell-2 is obviously larger than that of a single cell, and the maximum bonds number can reach up to 22, more than twice the number of bond in the single cell case. Unlike that in the single cell adhesion, the bonds number of cell-2 experience an unstable variation, and then reach a steady bonds number state. To further elaborate on this phenomenon, the relative flow vectors around each cell are plotted in Figs. 5.8(g)-(h). The cells not only translate but also rotate, and the relative vectors are actually relative to the translation only. Around cell-2, the fluid moves faster than the cell and the flow vectors are close and clockwise around the cell. In contrast, the relative flow vectors are very small around cell-1, indicating the speed of cell-1 is almost the same as that of surrounding fluid. Fig. 5.8(i) plots the total perpendicular force of each cell along the vessel where the negative sign indicates toward the wall (wallward). The wallward force on cell-2 is much larger than that on cell-1, which pushes cell-2 to the wall, resulting in much more receptor-ligand bindings than cell-1.

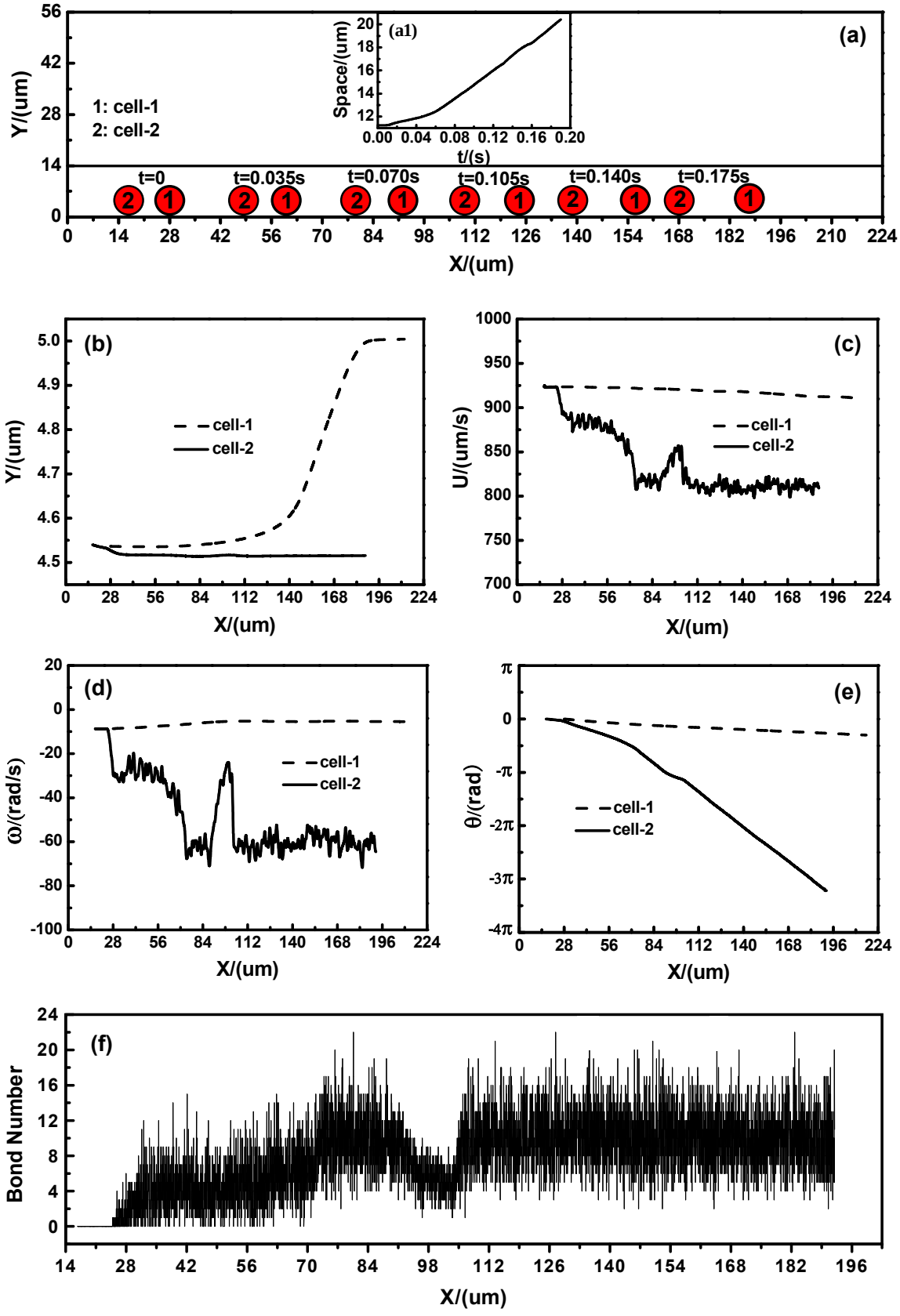
(a)
(a1)
Space/(um)
t/(s)
1: cell-1
2: cell-2
t=0
t=0.035s
t=0.070s
t=0.105s
t=0.140s
t=0.175s
Y/(um)
X/(um)
(b)
cell-1
cell-2
(c)
U/(um/s)
(d)
ω/(rad/s)
(e)
θ/(rad)
(f)
Bond Number

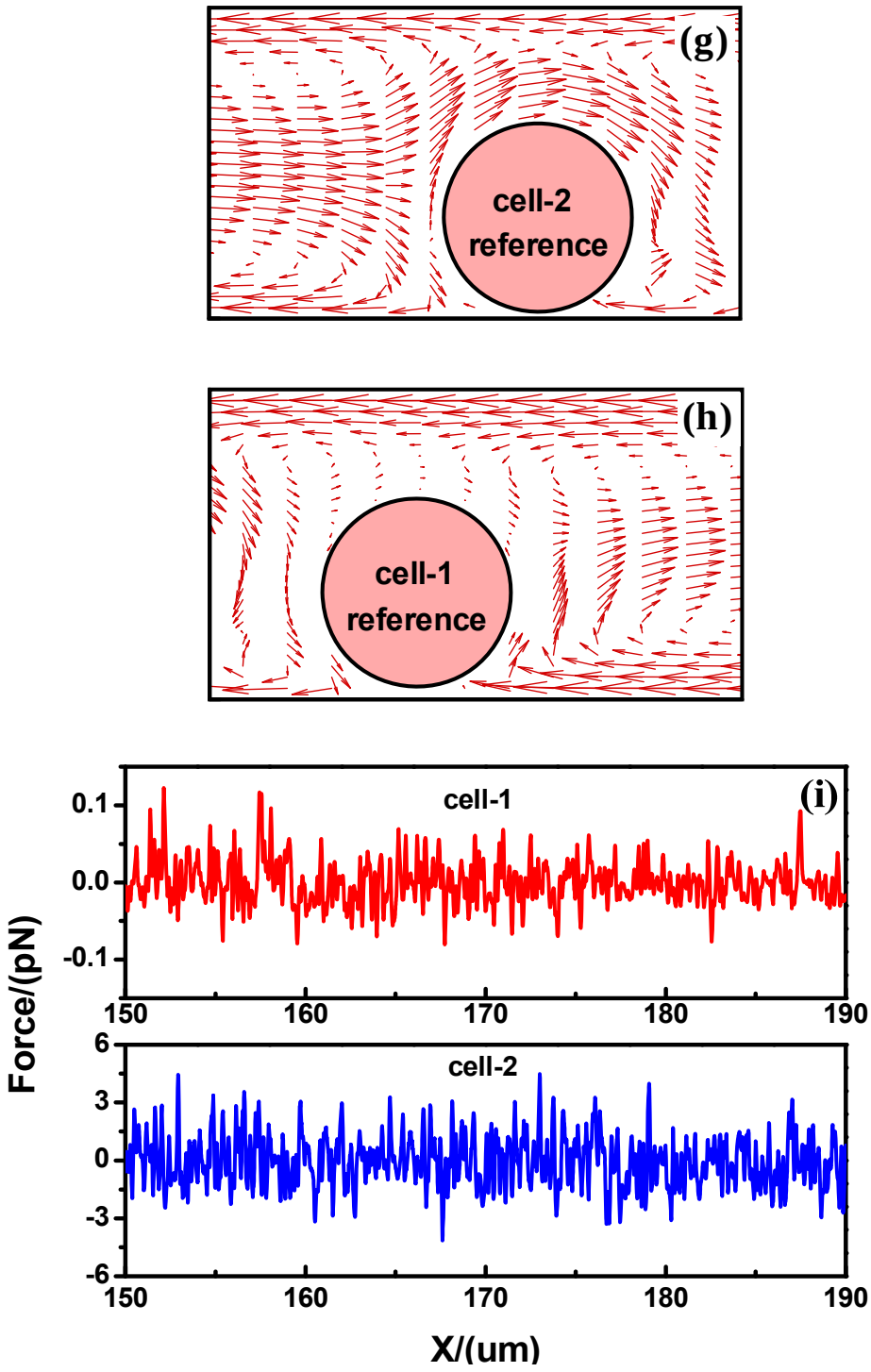

Figure 5.8 The history of two cells adhesion and interaction in the straight micro-vessel: (a) trajectory and spacing, (b) trajectory, (c) velocity, (d) angular velocity, (e) rotation angle, (f) number of bonds for cell-2, (g) relative flow vectors around cell-1 (frame is fixed on cell-1), (h) relative flow vectors around cell-2 (frame is fixed on cell-2), and (i) distribution of total perpendicular force along the vessel wall.

5.3.2 Adhesion and Interaction of Two Cells in the Curved Micro-vessel

Furthermore, we also study two cells adhesion and interaction in a curved vessel. Here, the initial place of both cell-1 and cell-2 is the same as that of two cells in the straight vessel. The pressure drop Δp is also set as 12.75 Pa ($0.05\,\mathrm{Pa}/\mu\mathrm{m}$), the same as that of single cell adhesion in the curved vessel.

Fig. 5.9 shows the history of two-cell adhesion and interaction in the curved vessel. Similar to the single cell case, the cell speed is averaged over 20 μs. Fig. 5.9(a) shows the relative position of the two cells at different times, the spacing between the two cells is almost constant in the bend and becomes larger out of the bend. The speed of both cells experiences significant fluctuations due to the adhesion and curvature effect, as indicated in Fig. 5.9(b). The speed of cell-1 firstly drops from 1,030 to 800 μm/s due to the cell adhesion effect, then the cell-1 moves like a free cell, and its velocity increases and experiences several fluctuations. However, the speed of cell-2 experiences two valleys, the distribution is almost symmetric and follows the curved geometry, indicating that the adhesion occurs at both the entrance and exit of the curved vessel. Fig. 5.9(c) shows a strong oscillation of the angular velocity due to the coupled effect of adhesion and cell-cell interaction. It is interesting to note that the rotating angle of the two cells is almost the same as shown in Fig. 5.9(d), even the adhesion status and the flow field of each cell are quite different.

The number of bonds in cell-1 and cell-2 are illustrated in Figs. 5.9(e) and (f), respectively. Compared to the single cell adhesion in the curved vessel, the

number of bonds of cell-1 is much smaller, and the adhesive length is much shorter. There is nearly no adhesion for cell-1. However, the bonds number of cell-2 increases significantly, the highest bonds number reaches 23, and the adhesion occurs at both the entrance and exit of the curved vessel. The bonds number of cell-2 changes dramatically during the whole process. Firstly, the cell rolls as a free cell, since there is no bond formed from the initial position to about $x = 22\ \mu$m. Then the bonds number increases from 1 to 7 in the straight part of the vessel. Once entering the curved part of the vessel, the bonds number augments quickly. Then there is a sharp drop in the bonds number at about $x = 59\ \mu$m. A possible explanation for this is that, with the increment of bonds formed, the distance between the moving cell and ECs at the wall is so close that the repulsive van der Waals force is big enough to expel the cell always from the vessel wall. When the cell moves into the positive curvature vessel, there is no bond found in that domain at all. In contrast, like the situation in the negative curvature vessel near the inlet, there are many bonds formed with the same peak and similar average value in the negative curvature vessel near the outlet. To further investigate the effect of curvature on receptor-ligand binding, the relative flow vectors around each cell are plotted in Figs. 5.9(g) and (h), respectively.

Figure 5.9(i) shows the distribution of total perpendicular force along the vessel wall. Similar to that in the straight vessel, the perpendicular force also exhibits the oscillatory pattern in the curved vessel; the oscillating amplitude of cell-2 is much larger than that of cell-1. Specifically, the magnitude of the

wallward force on cell-2 in the curved vessel is about 1.6 times of that in the straight mciro-vessel. This explains why cell-2 generates more receptor-ligand bonds in the curved vessel than that in the straight one. From above analysis, we can conclude that cell adhesion is strongly dependent on local geometry of the vessel and the interaction with other cells.

Figure 5.10 shows the statistical comparison of bonds number for cell-2 between the straight and curved vessels. Similar to the single cell case, at lower bond numbers, the straight vessel has higher probability to form the bonds. The turning point is at the bond number of 8. When the bond number is larger than 8, the curved vessel has more chances to form bonds between cell-2 and the endothelial cells at the vessel wall. At higher bonds number, e.g. bonds number of 21 or more, the bond forming probability of the curved vessel can be five times that of the straight vessel. As discussed earlier, the final cell adhesion is actually dependent on the simultaneous bond forming. The higher the bonds number, the more likely cell adhesion occurs. Therefore, the cell, particularly under the interaction of other cells, has higher probability to adhere to the endothelial cells in the curved vessel than in the straight vessel.

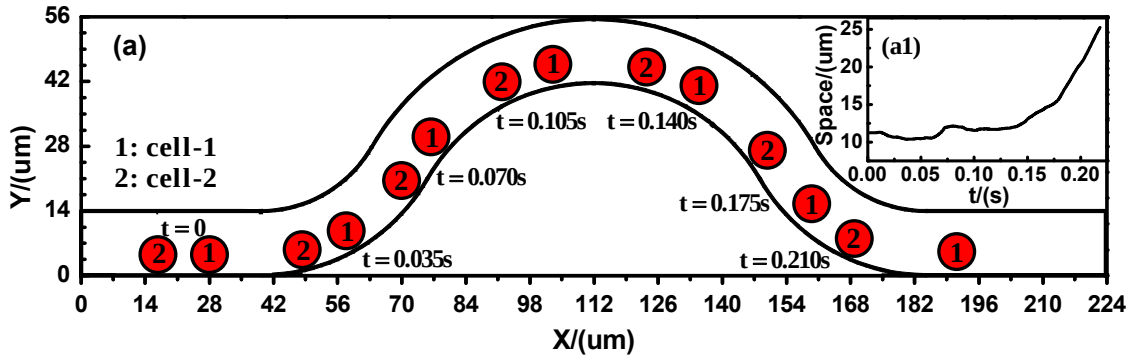
(a)
1: cell-1
2: cell-2
t = 0
t = 0.035s
t = 0.070s
t = 0.105s
t = 0.140s
t = 0.175s
t = 0.210s
Y/(um)
X/(um)
(a1)
Space/(um)
t/(s)

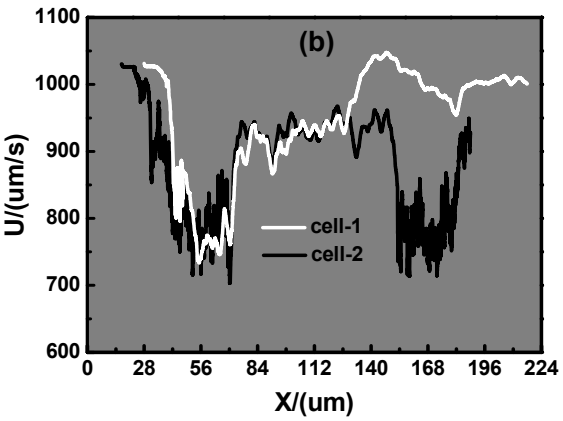
(b)
cell-1
cell-2
U/(um/s)
X/(um)

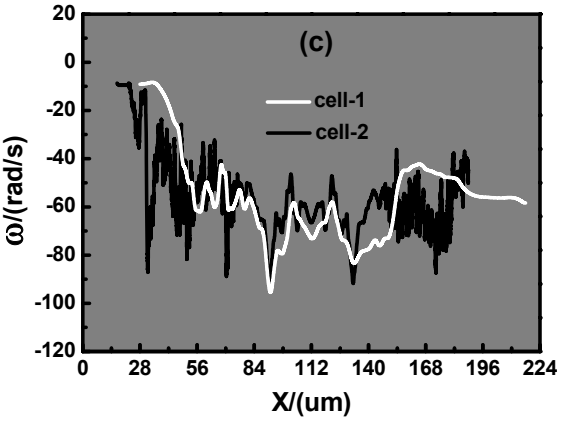
(c)
cell-1
cell-2
ω/(rad/s)
X/(um)

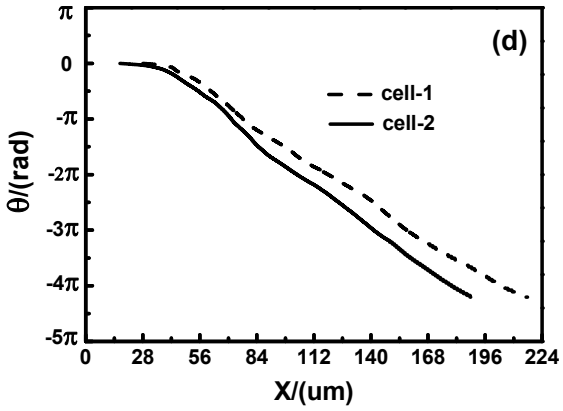
(d)
cell-1
cell-2
θ/(rad)
X/(um)

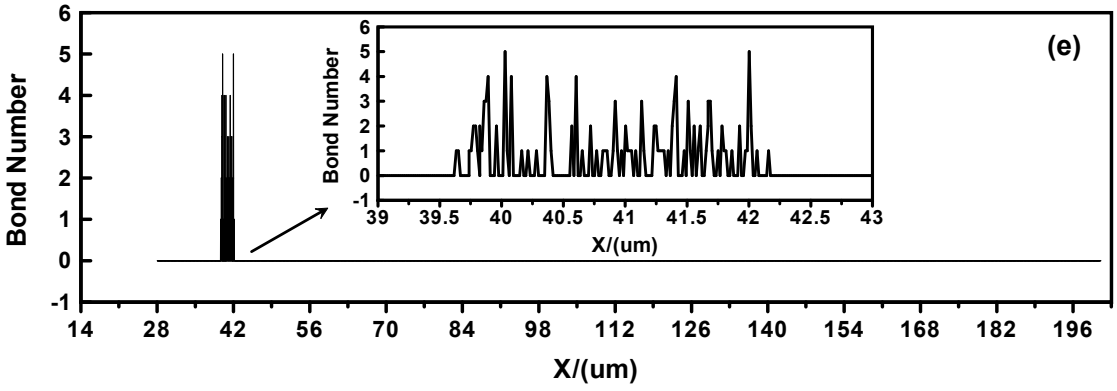
(e)
Bond Number
X/(um)

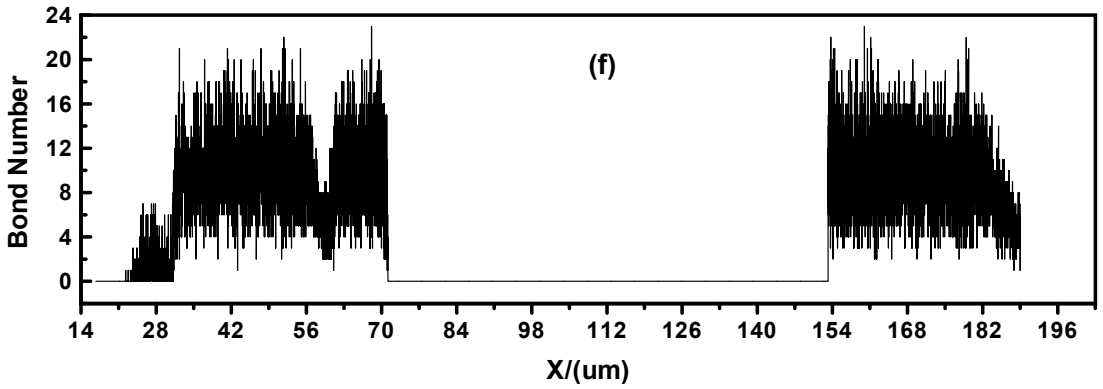
(f)
Bond Number
X/(um)
0
4
8
12
16
20
24
14
28
42
56
70
84
98
112
126
140
154
168
182
196

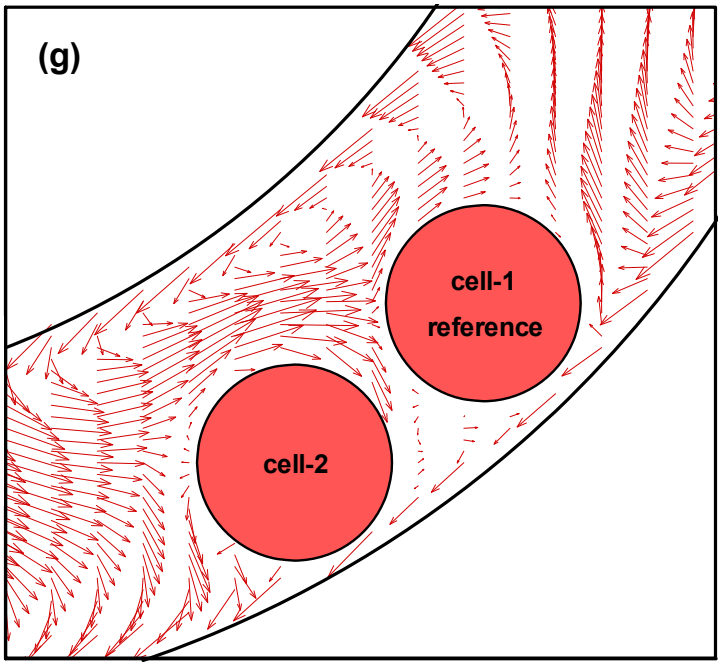
(g)
cell-1
reference
cell-2

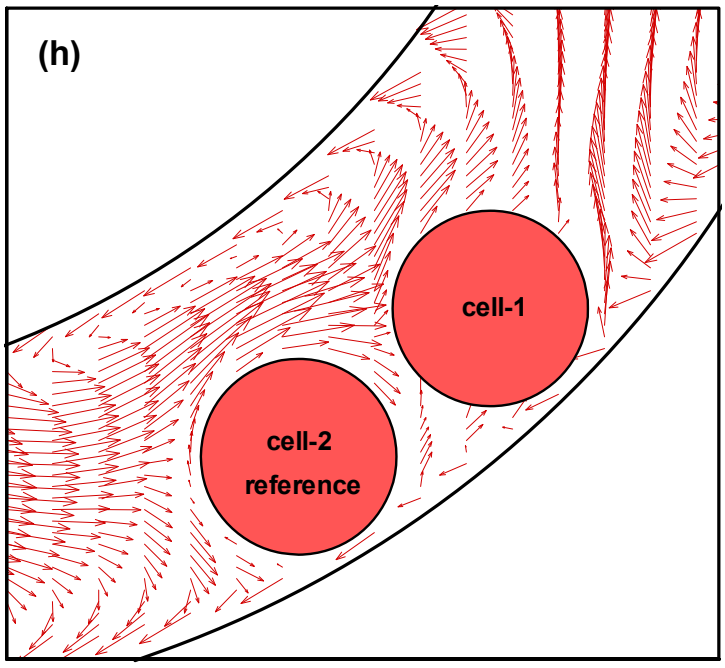
(h)
cell-1
cell-2
reference

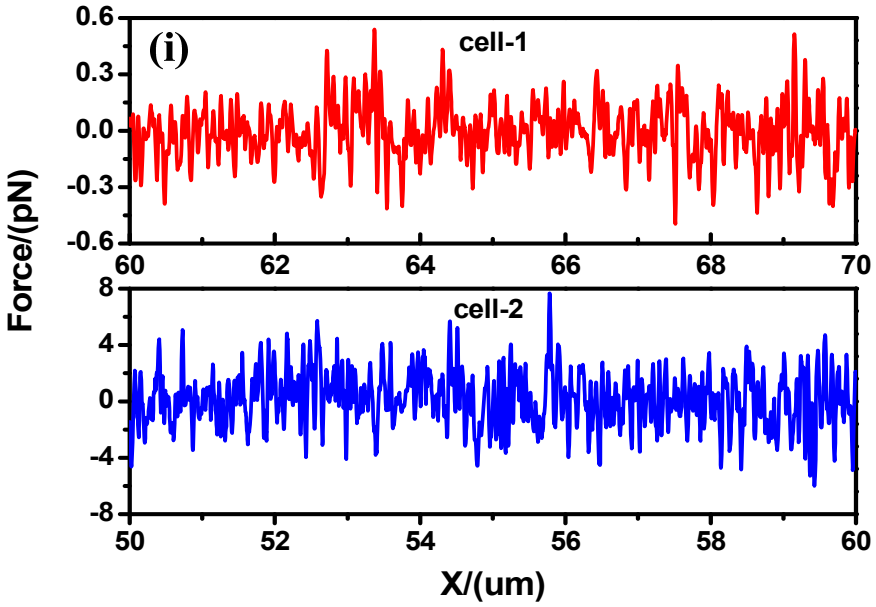

Figure 5.9 The history of two cells adhesion and interaction in the curved micro-vessel: (a) trajectory and spacing, (b) velocity, (c) angular velocity, (d) rotation angle, (e) number of bond for cell-1, (f) number of bond for cell-2, (g) relative flow vectors around cell-1 (frame is fixed on cell-1), (h) relative flow vectors around cell-2 (frame is fixed on cell-2), and (i) distribution of total perpendicular force along the vessel wall.

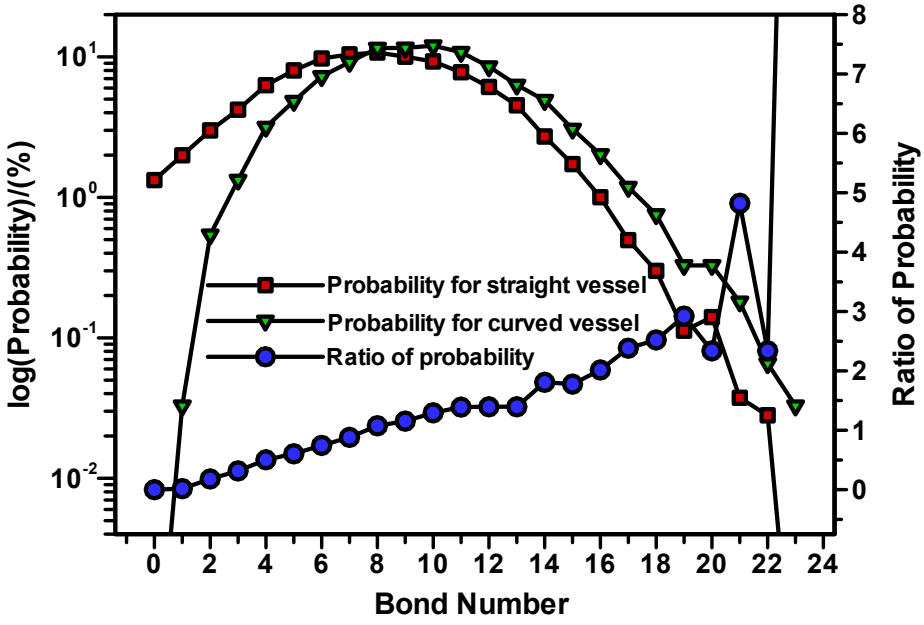

Figure 5.10 Comparison of bond formation probabilities and the ratio of these probabilities between the straight and curved micro-vessels.

5.4 Summary

The effects of the vessel curvature and the cell-cell interaction on cell adhesion in the micro-vessels have been numerically studied by using the LBM. The cell adhesive dynamics is modeled by adhesive receptor-ligand bond which is based on the Dembo et al.'s model of reaction rates law. Both the single cell and double cells in either the straight or the curved micro-vessel have been investigated. The simulation results lead to the following conclusions:

(1) The local geometry or the curvature has significant influence on bond formation between the traveling cells and endothelium at the vessel wall. Usually, the simultaneous number of bond would increase in a curved vessel, and consequently the probability of cell adhesion is increased as well.

(2) The interaction between the traveling cells is significant, and the cell-2 (rear) would experience higher wallward force, which would enhance the receptor-ligand binding, therefore, this interaction would increase the cell adhesion probabilities.

(3) From a physiological point of view, most of the micro-vessels are either curved or bifurcated and there are always multiple cells traveling in the same micro-vessel. The above conclusions indicate that the study of the single cell adhesion in a straight vessel may underestimate the capability of cell adhesion in the micro-vessels under real physiological and pathological conditions.

Chapter 6

Effects of Wall Shear Stress and its Gradient on Tumor Cell Adhesion in Curved Micro-vessels

It has been reported that the blood cells and tumor cells are more easily arrested by the curved micro-vessels than the straight ones (Liu et al. 2008; Lv et al. 2007). Our previous study in chapter 5 indicates that the vessel curvature and cell-cell interaction would significantly enhance this preferential cell adhesion in the curved vessels (Yan et al. 2010a). At the curved sites, there are rather complicated distributions of wall shear stress, which appears to render these sites to be prone to catch cells. However, the mechanical mechanism of the blood cells and tumor cells accumulating at curved sites and the quantitative relationship between the wall shear stress variation and cell adhesion are not yet completely understood. This motivates us to experimentally and computationally study the effects of wall shear stress and its gradient on tumor cell adhesion in the curved micro-vessels.

Our in vivo experiments were performed on the micro-vessels (post-capillary venules, 30-50 μm diameter) of rat mesentery. A straight or curved vessel was cannulated and perfused with tumor cells by a glass micropipette at a velocity of about 1.0 mm/s. At less than 10 minutes after perfusion, there was a significant difference in cell adhesion to the straight and curved vessel walls. In 60 minutes, the averaged adhesion rate in curved vessels was about 1.5 fold of that in straight vessels. In the curved segments, 45% of cell adhesion was initiated at the inner side, 15% at outer side and 30% at both sides of the curved vessels.

We also performed the computational study of tumor cells adhesion in the curved micro-vessels. The numerical methods adopted in this study are the same as those in our previous study (Yan et al. 2010a). The fluid dynamics was carried out by the LBM, and the cell dynamics was solved by the Newton's law of translation and rotation. However, the adhesive dynamics model adopted here was newly modified based on the Bell's model of forward/reverse reaction rates to consider the influence of wall shear stress and its gradient on receptor-ligand bonds, in which the positive shear stress/gradient jump would stimulate cell adhesion while the negative shear stress/gradient jump would weaken cell adhesion. It is found that the wall shear stress/gradient, over a threshold, have significant contribution to the cell adhesion by activating or inactivating cell adhesion molecules. Our results can elucidate why the tumor cell adhesion always occurs at the positive curvature in the curved vessels with very low Reynolds number laminar flow (in the order of 10^{-2}).

6.1 Adhesion Behavior States in the Straight Micro-vessel

To validate the present numerical scheme which coupled with the Bell's model into the LBM, cell adhesion with different values of the Bell's model parameter is implemented first in the straight vessel. The length of the straight vessel is $480\,\mu$m, and the diameter of the vessel is $40\,\mu$m. The pressure difference Δp between the inlet and outlet is set as 10.0 Pa. Except for the unstressed dissociation rate k_r^0 and microvillus reactive compliance γ, the values of the other simulation parameters are listed in Table 6.1.

Table 6.1 Simulation parameters and values

Parameter	Definition	Value (reference)
R_c	cell radius	5.0 μm (Ref. [1])
H_c	cut-off length for bond formation	40 nm (Ref. [2])
ρ_f	plasma density	1.03 g/cm^3 (Ref. [3])
ν	plasma kinetic viscosity	1.2×10^{-6} m^2/s (Ref. [2])
T	temperature	310 K (Ref. [2])
λ	equilibrium bond length	20 nm (Ref. [2])
k_b	Boltzmann constant	1.38×10^{-23} J/K
σ	spring constant	2×10^{-3} N/m (Ref. [4])
$k_f{}^n$	normal association rate	84 s^{-1} (Ref. [2])
k_r^0	unstressed dissociation rate	200 s^{-1} (Ref. [5])
γ	reactive compliance	0.75 Å (Ref. [5])
N_r	receptor density	47 / μm^2 (Ref. [4])

Ref. [1]: Brunk et al. 1997

Ref. [2]: Chang et al. 2000

Ref. [3]: Skalak and Chien 1987

Ref. [4]: Chang and Hammer 1996

Ref. [5]: Bell 1978

By setting the Bell's model parameters: $\gamma = 0.5\,\text{Å}$ and $k_r^0 = 200\,\text{s}^{-1}$, the simultaneous number of bonds for a representative rolling cell is shown in Fig. 6.1. After a short traveling, the total number of bonds of the cell fluctuates from 1 to 15 with an average of about 9, never falling below one bond, so the cell is always bound to the surface of endothelial wall. These stretched bonds, which provides a large component of spring forces to act in a direction to resist the hydrodynamic shear force, would also reduce the instantaneous cell velocity and angular velocity due to adhesion effect, which has been discussed in chapter 5.

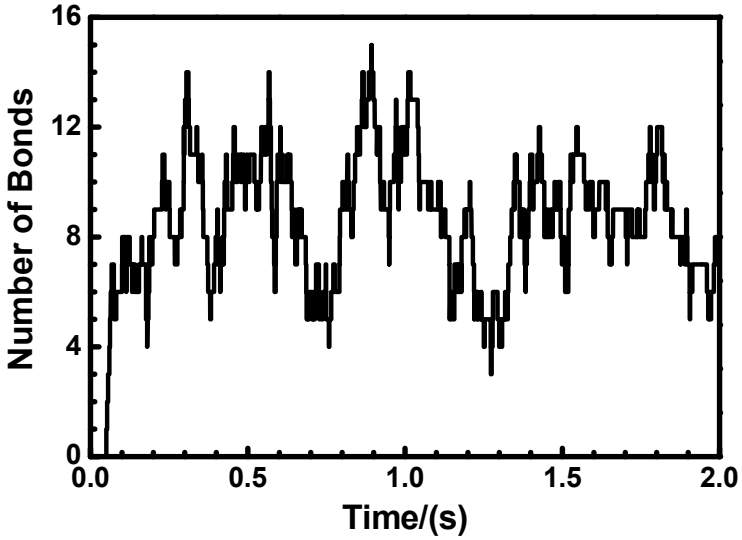

Figure 6.1 Number of bonds of the representative rolling cell.
The Bell's model parameters are $\gamma = 0.5\,\text{Å}$ and $k_r^0 = 200\,\text{s}^{-1}$

It has been reported that these dynamics states of cell adhesion are governed by the Bell's model parameters of dissociation rate and reactive compliance (Chang et al. 2000). By using the parameters that tabulated in Table 6.1, we simulate a series of cells with different unstressed dissociation rates and microvillus reactive compliances. In the simulations, we choose γ and k_r^0 as: (A)

0.5 Å and 1000 s^{-1}, (B) 0.5 Å and 200 s^{-1}, (C) 0.75 Å and 20 s^{-1}, and (D) 0.5 Å and 20 s^{-1}, respectively. The representative trajectories of four adhesion behavior states are shown in Fig. 6.2.

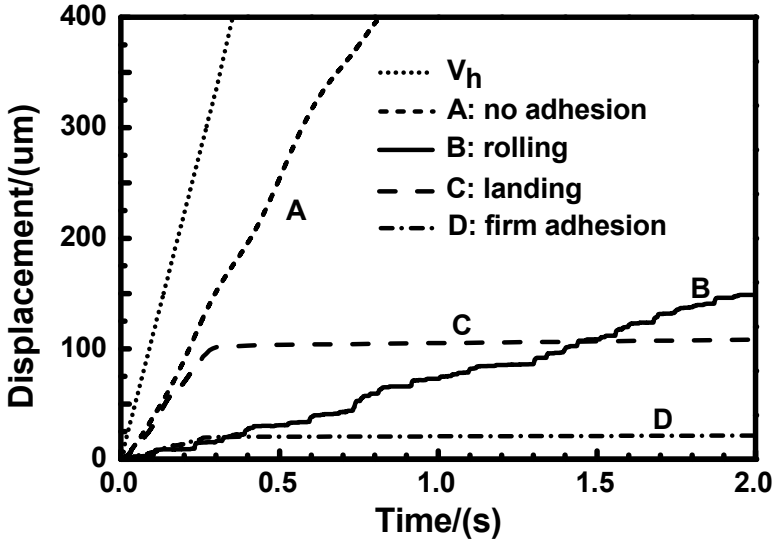

Figure 6.2 Representative trajectories of adhesion behavior states in the straight vessel. The Bell's model parameters γ and k_r^0 are: (A) 0.5 Å and 1000 s^{-1}, (B) 0.5 Å and 200 s^{-1}, (C) 0.75 Å and 20 s^{-1}, and (D) 0.5 Å and 20 s^{-1}

The average velocities of the cells for the no adhesion, cell rolling and firm adhesion case are approximately 40%V_h, 6.5%V_h and 0.9%V_h, respectively. Here, V_h is the hydrodynamic free-stream velocity. For the cell landing case, the cell firstly circulates with a high velocity and suddenly firmly adheres to the vessel wall at about t = 0.3 s. It can be found that our numerical results agree well with the definition of adhesion behavior states (Evans 1997; Caputo and Hammer 2005), suggesting our present numerical scheme is available for simulating different dynamics states of cell adhesion in the straight vessels. Moreover, one can find that the unstressed dissociation rate k_r^0 has greatly influence on cell

adhesion under the same association rate k_f (where k_f = 84 s^{-1}). The larger unstressed dissociation rate the more obvious the cell adhesion effect will be.

6.2 Experimental Study

Before carrying out the numerical studies, the in vivo experimental observation of tumor cells adhesion in the curved micro-vessels is presented. Up to date, the circulating blood cells adhesion in the curved micro-vessels has been studied experimentally by performing on rat mesentery (Liu et al. 2008). These experimental observations suggested that the circulating blood cells were likely to gather together initially from the positive curvature segments (inner curved sites) in the curved micro-vessels. To further explore these strange phenomena of cell adhesion, the circulating tumor cells adhesion is also experimentally carried out in the curved micro-vessels.

6.2.1 Experimental Methods

The experiments were finished by our partners Prof. Fu Bingmei and Dr. Cai Bin, who are both at the Department of Biomedical Engineering, The City College of the City University of New York. Experiments were performed on rat mesentery. All procedures have been approved by the Animal care and Use Committees at the City College of the City University of New York. Female Sprague-Dawley rats (250-300 g) were supplied by Hilltop Laboratory Animals (Scottdale, PA). Rats were anesthetized with pentobarbital sodium given subcutaneously at the initial dosage 65 mg/kg and additional 3 mg/dose as needed. After a rat was

anesthetized, a midline surgical incision (2-3 cm) was made in the abdominal wall. The mesentery was gently taken out from the abdominal cavity and spread on a glass coverslip, which formed the base of the observation platform as previously described (Fu et al. 2005). The gut was gently pinned out against a silicon elastomer barrier to maintain the spread of the mesentery. The upper surface of the mesentery was continuously superfused by a dripper with mammalian Ringer solution at 35-37°C, which was regulated by a controlled water bath and monitored regularly by a thermometer probe (Fu and Shen 2004; He et al. 1998). The micro-vessels chosen for the study were straight or curved post-capillary venules, with diameters of 30-50 μm. All vessels had brisk blood flow immediately before cannulation and had no marginating white cells.

The detailed method for cell adhesion experiment was described in Shen et al. (2010). Briefly, a single post-capillary venule was cannulated with a glass micropipette (~30 μm tip diameter, WPI Inc., Florida) and perfused with the 1% BSA rat Ringer solution with Calcein AM-labeled human breast cancer cells MDA-MB-231 at a mean flow velocity of ~1mm/s, which is the normal blood circulation velocity in this type of vessels. For this perfusion velocity, there were ~50 cells/min out of the micropipette tip if the cell concentration in the pipette was 4 million/ml. A Nikon Eclipse TE-2000 inverted microscope with a 20X objective lens (NA 0.75, super, Nikon) was used to observe the adhesion process and pictured by a high performance digital 12 bit CCD camera (SensiCam QE, Cooke Corp., Romulus, MI) using InCyt Im 1 software. Adherent cells were

counted offline in a vessel segment of 300-400 μm length and expressed as the number of adherent cells per 5000 μm^2 plane area of the vessel segment. The measuring area was set at least 150 μm downstream from the cannulation site of the vessel to avoid entrance flow effects.

6.2.2 Experimental Results

The experimental installation is shown in Fig. 6.3 (a), and Fig. 6.3 (b) shows a typical photomicrograph for tumor cell adhesion in a curved micro-vessel. Figure 6.3(c) summarizes the cell adhesion in 14 curved vessels and 19 straight vessels. Overall, in less than 10 minutes, tumor cells adhered significantly more in the curved vessels than in the straight ones. For a 60 minutes period, the averaged adhering rate of tumor cells in the curved vessels was ~1.5 fold of that in the straight vessels ($p < 0.03$).

Figure 6.3 (d) presents the distribution of adhering sites as a function of the vessel diameter and the curve angle in the curved vessels. Figure 6.3 (e) compares the adhesion initiation times at different sites and in the curved and straight vessels. Cell adhesion started at the inner side (positive curvature) of the curved sites in 23 out of 51 curved segments (45%) and with the shortest initiation time of 4.5 ± 0.7 (mean ± SE) minutes; started at both sides in 15 out 51 curved segments (30%) with an insignificantly longer initiation time of 5.2 ± 0.7 minutes; started at the outer side in 13 out of 51 curved segments (25%) with the longest initiation time of 8.9 ± 1.9 minutes ($p < 0.05$). Compared to the straight vessels with the initiation time of 7.0 ± 0.7 minutes, the initiation time at the inner side

(negative curvature) of the curved vessels was significantly shorter. Our results indicate that tumor cells have preference in adhering to the wall of the curved vessels and initiate at the inner side of the curved segments. Although there was no preference in cell adhesion in the size of the post-capillary venules in our range (30-50 μm diameter), there was a preference in the curve angle. Cell adhesion tended to initiate in the inner or both sides of the curved segments if the curve angle is in the middle zone of 50-150 degrees (see Fig. 6.4 for the definition of the curve angle θ). In contrast, cell adhesion tended to initiate at the outer side when the curve angle was either small or large.

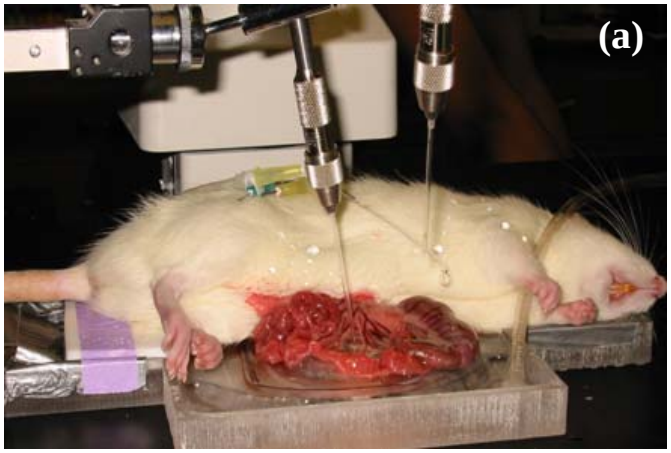

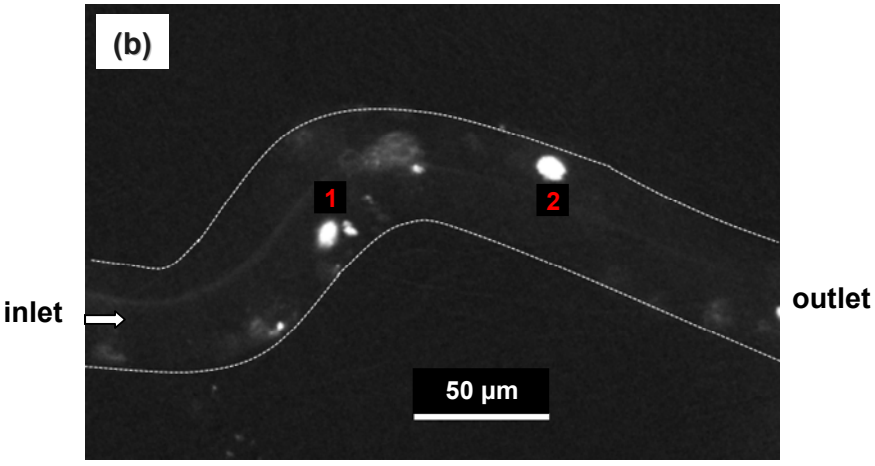

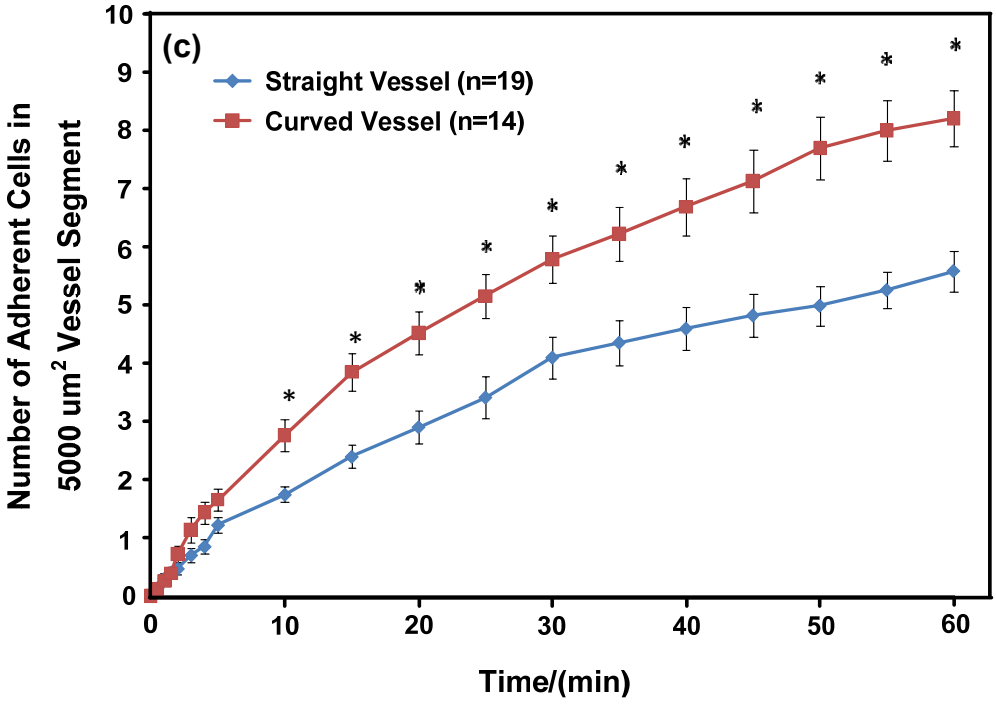
(c)
Straight Vessel (n=19)
Curved Vessel (n=14)
Number of Adherent Cells in 5000 um2 Vessel Segment
Time/(min)
0
1
2
3
4
5
6
7
8
9
10
0
10
20
30
40
50
60
*

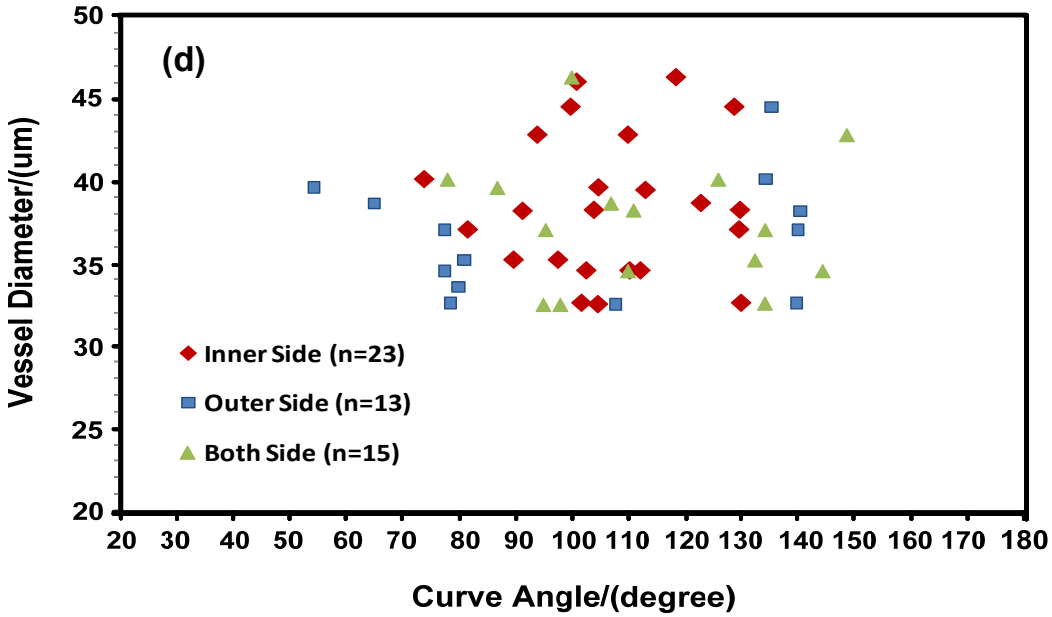
(d)
Inner Side (n=23)
Outer Side (n=13)
Both Side (n=15)
Vessel Diameter/(um)
Curve Angle/(degree)
20
25
30
35
40
45
50
20 30 40 50 60 70 80 90 100 110 120 130 140 150 160 170 180

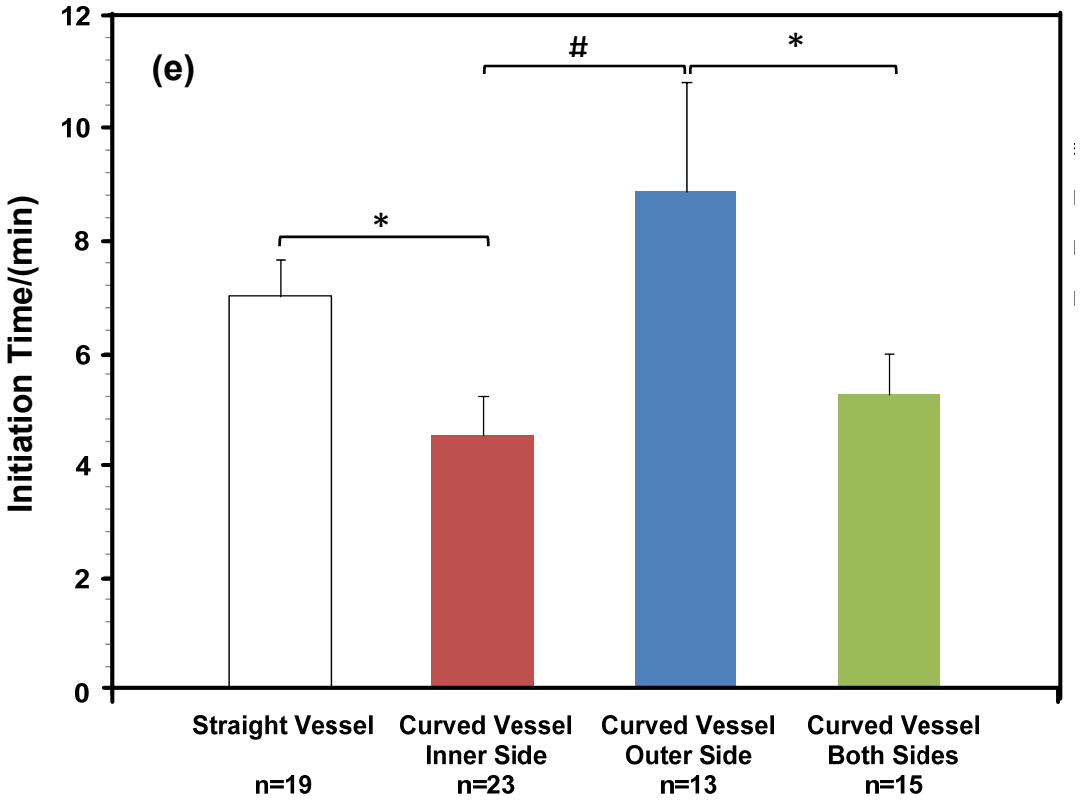

Figure 6.3 (a) Experimental installation. (b) Photomicrograph of cancer cell adhesion to a curved micro-vessel of diameter ~40 μm after ~30 minutes perfusion. The bright spots are adherent tumor cells. Flow was from left to right. (c) Comparison of tumor cell adhesion in the straight and curved vessels. Data presented are mean ± SE. *, $p < 0.03$. (d) Location of initial tumor cell adhesion in the curved vessels as a function of curve angles and vessel diameters. (e) Comparison of initiation times for tumor cell adhesion in the straight vessels, at inner, outer and both sides of curved vessels. Data presented are mean ± SE. *, $p < 0.05$; #, $p < 0.01$.

6.3 Modified Adhesive Dynamics Models

The adhesive dynamics model is coupled into the fluid dynamics and cell dynamics to take into account the effect of receptor-ligand bonds on tumor cell adhesion. The interactions between receptors and ligands are realized via the compression and expansion of the ideal adhesive springs, and the kinetic expressions for receptor-ligand bonds relate the bond association and dissociation rates. The normal bonds association and dissociation rates have been introduced in chapter 2, they are

$$k_f{}^n = 84 \tag{6.1}$$

$$k_r{}^n = k_r^0 \cdot \exp\left(\frac{\gamma f}{k_b T}\right) \tag{6.2}$$

where $k_f{}^n = 84\,\mathrm{s}^{-1}$ is a reasonable value that extensive simulations have shown can properly recreate experimental values for velocity and dynamics of rolling in the straight micro-vessels (Chang et al. 2000), k_b is the Boltzmann constant, T is the temperature, k_r^0 is the unstressed dissociation rate, γ is the reactive compliance, and f is the spring force of each bond calculated from the Hooke's law: $f = \sigma(\chi - \lambda)$, where σ is the spring constant, χ is the distance between receptor and ligand, and λ is the equilibrium bond length.

From the analysis of above experiments, it is found that the tumor cell adhesion usually occurs at the conjunction of curvatures in which the wall shear stress and its gradient vary significantly. That more cell adhesion occurs at the conjunction indicates that more ligands are activated there, i.e., the wall shear

stress and its gradient would promote the activation of ligands by increasing the bond association rate and decreasing the dissociation rate. Therefore, we modify the Bell's model and take into account the effect of wall shear stress on bond association/dissociation rates:

$$k_f = {k_f}^n \cdot \left(\frac{\tau}{\tau_0} \right)^{k_1} \tag{6.3}$$

$$k_r = {k_r}^n \cdot \left(\frac{\tau}{\tau_0} \right)^{k_2} \tag{6.4}$$

and the effect of wall shear stress gradient on bond association/dissociation rates:

$$k_f = {k_f}^n \cdot \exp\left(k_3 \frac{d\tau}{dl} \right) \tag{6.5}$$

$$k_r = {k_r}^n \cdot \exp\left(k_4 \frac{d\tau}{dl} \right) \tag{6.6}$$

where τ and τ_0 are the wall shear stress along the curved vessel and along the straight part of curved vessel, and $d\tau/dl$ is the wall shear stress gradient along the curved vessel. k_1, k_2 and k_3, k_4 are coefficients that represent the sensitivity of wall shear stress and its gradient to bond association/dissociation rates, respectively. The modified two adhesive dynamics models can reduce to the Bell's model at $k_1 = k_2 = 0$ and $k_3 = k_4 = 0$ which mean that the bond reaction rates have no dependence on wall shear stress and its gradient, of which has been studied in our previous work (Yan et al. 2010a). In the current simulations, we assume k_1, k_2 and k_3, k_4 to be 1.0, -5.0 and 1.0 μm/Pa, -50.0 μm/Pa, respectively, to match the experimental observations.

In this modified model, we consider three cases:

Case 1: The association/dissociation rates of the receptor-ligand bonds follow equations (6.3)-(6.4), which continuously vary with the ratio of wall shear stresses τ/τ_0;

Case 2: The association/dissociation rates of the receptor-ligand binding follow equations (6.5)-(6.6), which continuously change with the wall shear stress gradient $d\tau/dl$;

Case 3: Only the jumps or drops in the wall shear stress gradient can trigger the change of bond association/dissociation rates. Once triggered, the bond association/dissociation rates will keep the maximum/minimum value as calculated by equations (6.5)-(6.6) until the next wall shear stress gradient jump or drop occurs.

If the numerical results that based on these two modified adhesive dynamics models agree well with the in vivo experimental observations, we can deem our assumptions that the dependences of tumor cell adhesion on local wall shear stress and its gradient in the curved vessels are rational in the real biophysical situations.

6.4 Wall Shear Stress Distributions in the Curved Micro-vessel

From our new experiments described above, we can find that tumor cells preferred to adhere to the curved vessels and initiate at the inner side of the curved sites. To explore the mechanics of this phenomenon, a curved micro-vessel with both positive and negative curvature is designed. Fig. 6.4 shows the schematic view of the 2-D curved vessel, which is similar to our previous model geometry in chapter 5 (Yan et al. 2010a) except different dimensions. The vessel of diameter

$D = 40\ \mu$m starts with a straight segment and then a negatively bent segment of $\theta = \pi/3$ bending angle, with the inner curvature radius of 80 μm and the outer radius of 120 μm, following with a positively curved segment with the inner and outer radii of 50 and 90 μm, respectively. The right half of the vessel is symmetric to the left half with the total vessel length $L = 420\ \mu$m. Here, we used a cell of radius $R_c = 5\ \mu$m, a typical size of a circulating leukocyte or tumor cell. A_u, B_u, C_u, D_u and A_b, B_b, C_b, D_b are the conjunction of positive and negative segments, respectively. The cell is driven by a pressure difference Δp between the inlet and outlet, and the simulation parameters and their values have been listed in Table 6.1.

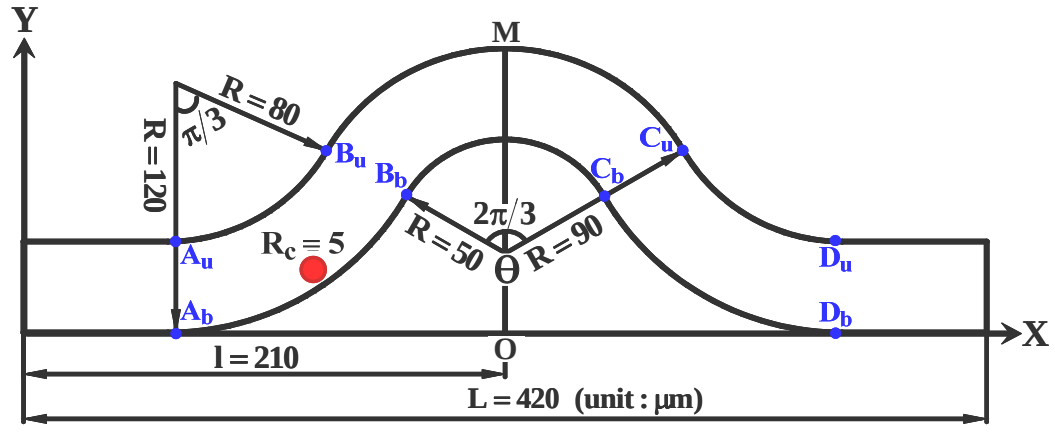

Figure 6.4 Schematic view of the curved micro-vessel

In our modified adhesive dynamics models, the wall shear stress and its gradient are the stimulus for changing the bond association/dissociation rates, therefore it is crucial to quantify the wall shear stress distribution. The flow field is firstly simulated to get the distributions of wall shear stress and their gradients.

Here, the pressure drop Δp is set as 10 Pa. Fig 6.5 (a) shows the wall shear stress distribution along both the upper and bottom vessel walls, and Figs. 6.5(b)-(c) show the corresponding shear stress gradient distributions, which are almost symmetric to $x = 210\,\mu$m. There are jumps (sudden increase) and drops (sudden decrease) in the wall shear stress and shear stress gradient at the conjunctions of the curved parts. Compares to the shear stress in the straight part of the curved vessel, the wall shear stress jumps occur at [A_u, B_u] and [C_u, D_u] while the drop occurs between B_u and C_u along the upper wall; along the bottom wall, the jump occurs between B_b and C_b while the drops happen at [A_b, B_b] and [C_b, D_b]. As to the wall shear stress gradient, the jumps occur at A_u and C_u while the drops occur at B_u and D_u along the upper wall, and the jumps occur at B_b and D_b while the drops occur at A_u and C_u along the bottom wall. The wall shear stress gradient jump is quite high at C_u of upper wall and at B_b of bottom wall, where the preferred locations of tumor cell adhesion observed in our above experiments. If the modified adhesive dynamics models are capable of describing the effect of the wall shear stress, the calculated tumor cell adhesion would most likely occur at these two locations.

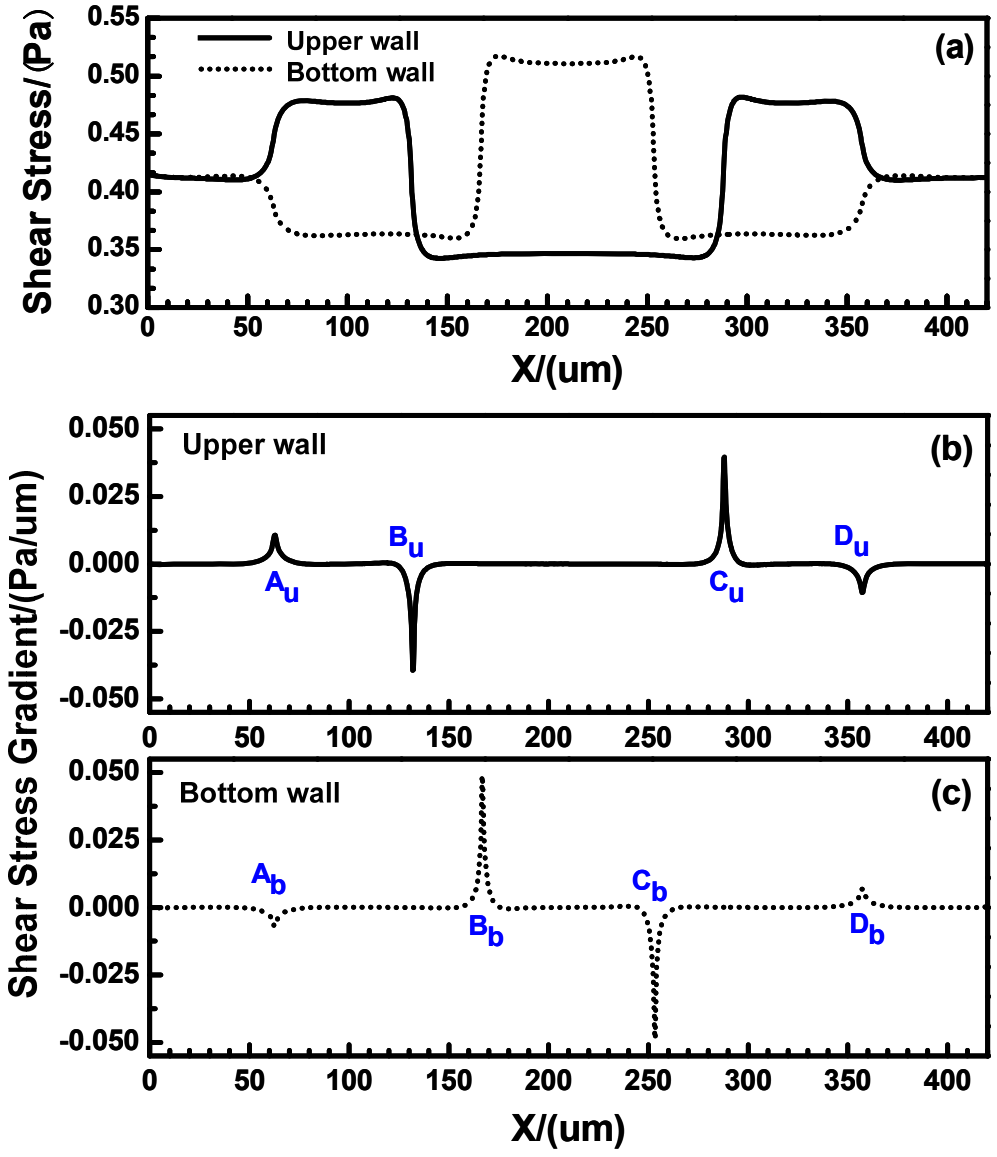

Figure 6.5 Wall shear stress distributions in the curved micro-vessel: (a) shear stress distributions along the upper/bottom walls, (b) shear stress gradient along upper wall, and (c) shear stress gradient along bottom wall

6.5 Modified Adhesive Dynamics Model: case 1

Firstly, the tumor cell adhesion with the modified adhesive dynamics model under the assumptions of case 1 is carried out by the LBM. Since the curvature would affect the trajectory of the cell, to assure the cell would roll over the conjunctions, the cell is released near either the upper or the bottom wall at the entrance.

Fig. 6.6 shows the history of tumor cell adhesion and migration when the cell is released near bottom wall. Fig. 6.6(a) shows the cell trajectory with constant time step. The denser trajectory occurs between A_b and B_b due to the centrifugal effect (Yan et al. 2010a); and the coarser trajectory happens between C_b and D_b, indicating a faster cell motion there due to the decrease in k_f and increase in k_r, both of which result from the drop of wall shear stress there. From Fig. 6.6(a), it can be found that the cell not only translates but also rotates, with which the rotation angle is about 20π clockwise in whole the journey. The corresponding cell velocity and angular velocity are illustrated in Figs. 6.6(b)-(c), respectively. The cell speed fluctuates between 50 and 750 μm/s from t = 0 to 1.3 s, and it suddenly increases from 750 to more than 1200 μm/s when the cell passes D_b and enters into the straight part of the curved vessel. The angular velocity of the cell mostly vibrates between -75 and -10 rad/s, and it fluctuates more strongly in the positive curvature vessel between B_b and C_b, which varies between -105 and -25 rad/s. Fig. 6.6(d) shows the history of bonds number at each location. The higher number of bonds means the larger opportunity of the cell arrested at the vessel wall. From A_b to B_b, the number of bonds fluctuates between 0 and 14, and the

number of bonds becomes less at [B_b, C_b], where the most bond number fluctuates between 0 and 8, although there is an increase in k_f and decrease in k_r that resulted from the jump of shear stress, which indicating that not the shear stress but the curvature effect on cell adhesion is dominant in this positive curvature vessel. Since $x \approx 288.0$ μm, the number of bonds stay zero, which suggesting that there is no cell adhesion at all and the cell moves freely in the curved vessel.

When the tumor cell is released near the upper wall, the cell trajectory is shown in Fig. 6.7(a). It can be found that the denser trajectory happens between C_u and D_u, indicating that there is stronger cell adhesion in the positive curvature where the local wall shear stress significantly increase. This can further be proved by the number of bonds which is displayed in Fig. 6.7(d). The number of bonds between C_u and D_u increases rapidly, and it fluctuates between 6 and 24, much larger than that of any other locations where the bonds number only oscillates between 0 and 16. Figs. 6.6 and 6.7 indicate that under the assumptions of case 1 that the bond association and dissociation rates continuously change with the wall shear stress, the most likely locations for tumor cell adhesion are between C_u and D_u, where the jump in the wall shear stress occurs. However, the shear stress effect on tumor cell adhesion is not as significant as that seen in the experiments in the positive curvature between B_b and C_b.

6.6 Modified Adhesive Dynamics Model: case 2

Now, the tumor cell adhesion with the refined adhesive dynamics model whose bond association/dissociation rates significantly depends on the wall shear stress gradient is carried out in the curved micro-vessel.

Fig. 6.8 shows the history of tumor cell motion when the cell is released near bottom wall. From the cell trajectory in Fig. 6.8(a), the denser trajectory occurs near the conjunction B_b ($x \approx 163.0$ μm), indicating a slower cell motion there due to the stronger adhesive effect caused by the large jump in the wall shear stress gradient at B_b. Another denser trajectory happens near the conjunction C_b ($x \approx 256.0$ μm) where the shear stress gradient has a sudden drop. This slower cell motion is not due to the adhesive effect but due to the centrifugal effect (Yan et al. 2010a). The coarser trajectory exists in the positive curvature vessel (between B_b and C_b), indicating a faster cell motion due to the centrifugal effect. The corresponding velocity history can be found in Fig. 6.8(b). As shown in Fig. 6.8(c), the variation of angular velocity is very similar to that of velocity. It fluctuates between -20 and -90 rad/s with an average value of about -40 rad/s, and it is larger in the positive curvature vessel than that at other locations. During the journey, the cell rotates more than 25π as shown in Fig. 6.8(a). The history of bonds number at each location is shown in Fig. 6.8(d). The maximum bonds number occurs near the conjunction B_b, although it is not distinctively higher than that at other locations.

When the tumor cell is released near the upper wall, as shown in Fig. 6.9(d),

the number of bonds near the conjunction C_u also increases but the increase is not as high as that near B_b because the jump in the wall shear stress gradient near C_u is less than that near B_b (Figs. 6.5(b)-(c)). Figs. 6.8 and 6.9 indicate that under the assumptions in case 2 that the association/dissociation rates of receptor-ligand binding continuously change with the wall shear stress gradient, the most likely locations for tumor cell adhesion are near B_b and C_u where the jumps in the wall shear stress gradient occur, although this shear effect is not as significant as seen in the experiments.

6.7 Modified Adhesive Dynamics Model: case 3

Under real physiological conditions, the association/dissociation rates of binding may not alter instantaneously with the variation of wall shear stress gradient. Most likely the wall shear stress gradient jump or drop, over certain threshold, is a stimulus for triggering the change in the association and dissociation rates of binding. Once triggered, these rates will stay the same values until the next jump or drop occurs. Under the assumptions of case 3, the effect of local shear stress gradient on tumor cell adhesion in a curved vessel is predicted.

Fig. 6.10 shows the cell trajectory, velocities and number of bonds when the cell is released near the bottom wall. When the cell approaches to the conjunction B_b ($x \approx 166.7\,\mu\text{m}$), the cell moves slower and slower, representing by a black band in the cell trajectory (in Fig. 6.10(a)), a flat plateau in displacement (in Fig. 6.10(b)) and a low and weak oscillation in the velocity (in Fig. 6.10(c)), which eventually goes to zero. The rotational velocity experiences the similar process.

When approaching to the conjunction B_b, the cell rolls slower and slower and eventually it stops, as shown in Figs. 6.10(d)-(e). Due to the change in the association and dissociation rates, the number of bonds increases significantly near the conjunction B_b (in Fig. 6.10 (f)).

When the tumor cell is released near the upper wall, more bonds are formed from conjunction A_u to B_u, and the number of bonds decreases from B_u to C_u (in Fig. 6.11(f)). Consequently, the cell moves/rolls slower from A_u to B_u, and then moves/rolls faster from B_u to C_u, as shown in Figs. 6.11(a)-(e). When the cell is approaching to conjunction C_u, the number of bonds increases suddenly, and consequently the cell slows down and eventually stops, indicating that the strong tumor cell adhesion occurs near C_u. Figs. 6.10-6.11 suggest that under the assumptions in case 3 that the bond association/dissociation rates vary with the jumps or drops of wall shear stress gradient, the firm adhesion of tumor cell occurs at positive curvature in both the upper and bottom vessel walls, which is in agreement with the *in vivo* experimental observation.

We have presented the tumor cell adhesion with two modified adhesive dynamics models under the assumptions of three different cases. In case 1, the bond reaction rates are assumed to continuously vary with the wall shear stress. When the tumor cell is released near the bottom wall, the larger adhesion probabilities take place between the conjunctions A_b and B_b at the outer side of vessel with a curved angle $\theta = 60$ degree, which agree unanimously with the experimental results in Fig. 6.3(d) that tumor cell adhesion prefer to occur at the

outer side when the curved angle is about 60 degree. When the tumor cell is released near the upper wall, the most likely locations for tumor cell adhesion is found between C_u and D_u at the inner side of curved vessel, owing to the signficant increase of wall shear stress there. This result approximates the obervastion in Fig. 6.3(b) (location 2), as well as that in Fig. 6.3(d) when θ is about 70 degree.

Under the assumptions in case 2 that the bond association/dissociation rates continuously change with the wall shear stress gradient, the larger adhesion probabilities are found near B_b and C_u where the jumps of wall shear stress gradient occur, nevertheless, this influence is quite weak, indicating that the effect of transient shear stress gradient on tumor cell adhesion can be neglected unless the wall shear stress gradient is over a critical value in the curved vessels. The tendencies of simulation results in this case are similar to the in vivo observations at locations 1 and 2 in Fig. 6.3(b).

As far as case 3 is concerned, the association/dissociation rates of receptor-ligand binding alter with the jumps or drops of wall shear stress gradient. In this case, the tumor cell is found to be firmly arrested by the vessel wall at the inner side of curved vessels when the tumor cell is released from both the bottom and upper walls. When the tumor cell is released near bottom wall, the tumor cell finally stops in the middle zones of [B_b, C_b], which are the most typical adhesion locations that seen in the experiments when the curved angle of vessel is around 120 degree. When the tumor cell is released near upper wall, the tumor cell is

eventually caught by the curved vessel in the middle zones of [C_u, D_u]. The predications of tumor cell adhesion along bottom and upper walls under the assumptions of case 3 are identical to the experimental observations in Fig. 6.3(b), in which the firm adhesion occurred at locations 1 and 2. It is realized that only the firm adhesion of tumor cells can effectively contribute to cancer metastasis in the microcirculation.

In all three simulation cases corresponding to the in vivo single vessel tumor cell perfusion experiments, we have demonstrated that tumor cells adhere more easily in the curved vessel than in the straight vessel, which is in agreement with the experimental observations summarized in Fig. 6.3. Overall, the present revised models are capable of simulating the tumor cell adhesion phenomena in the curved micro-vessel by activating or inactivating cell adhesion molecules that located at the surfaces of tumor cells and endothelial cells to form receptor-ligand bonds, whose association/disassociation rates would be enhanced or weakened by the shear stresses/gradients along the vessel walls. However, to simplify the conditions, we neither considered the contribution from the circulating blood cells in the simulation, nor in the experiment. We will incorporate the effect of circulating blood cells on tumor cell adhesion in the future study.

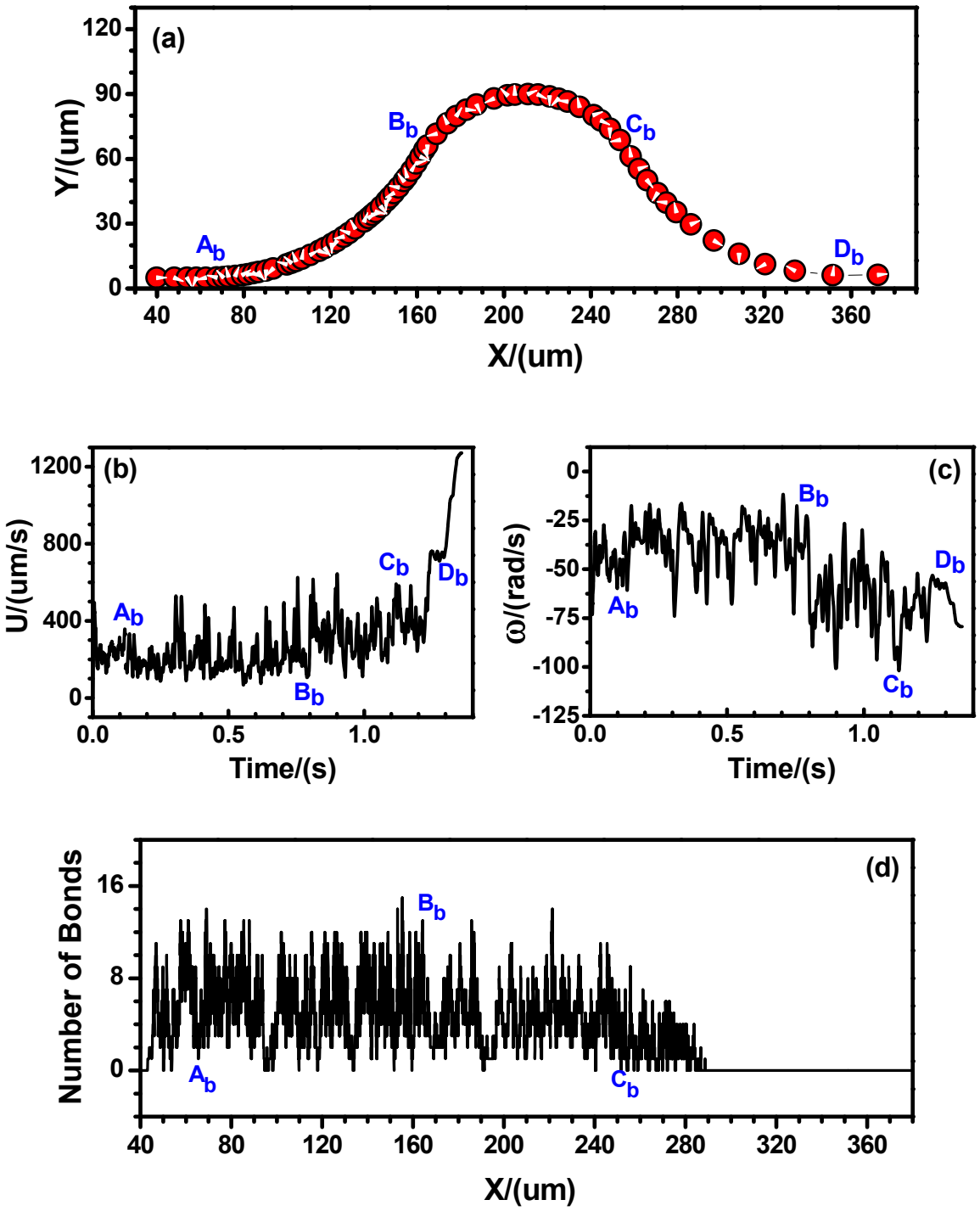

Figure 6.6 Case 1: the history of the cell released near the bottom wall: (a) trajectory, (b) velocity, (c) angular velocity, and (d) number of bonds.

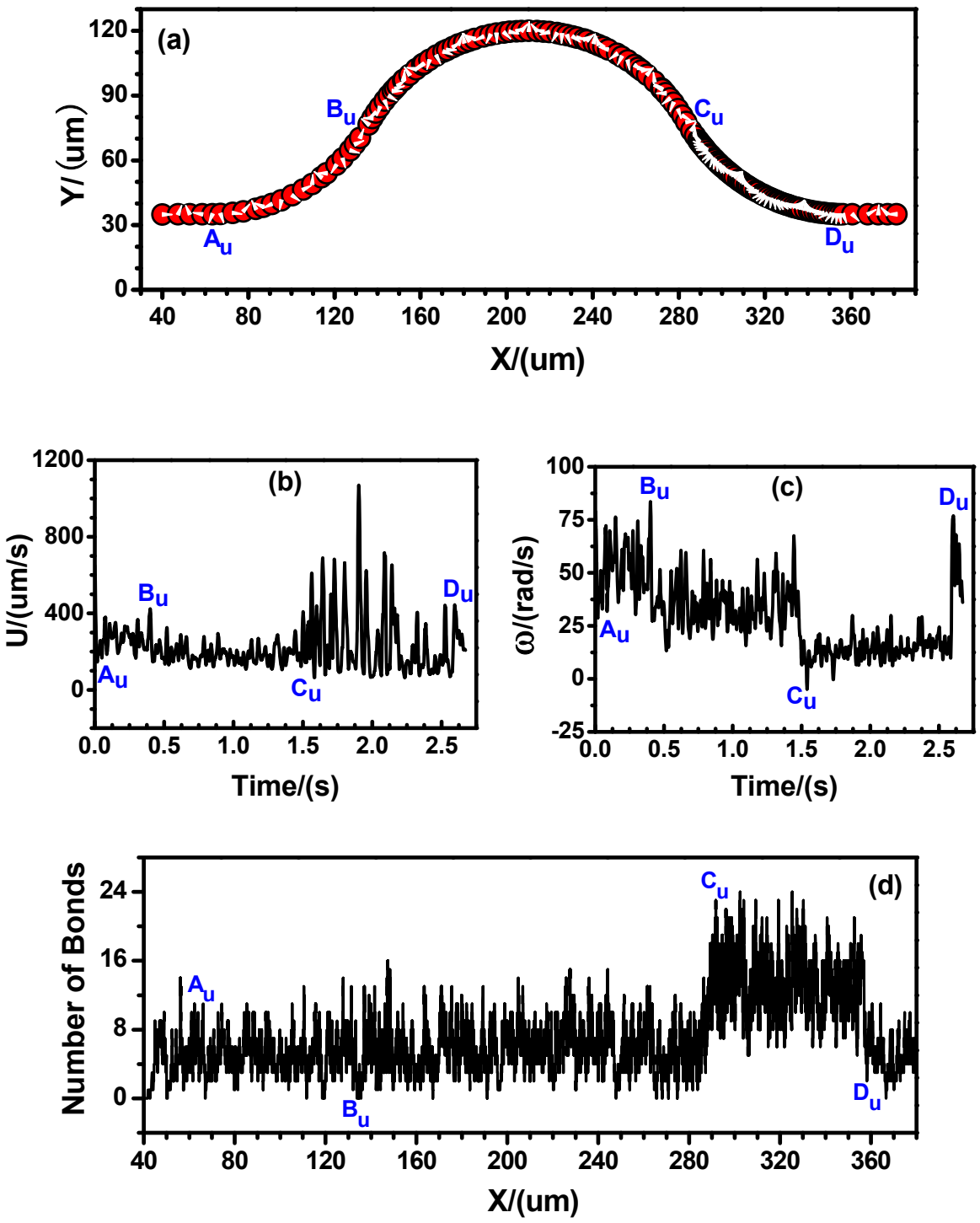

Figure 6.7 Case 1: the history of the cell released near the upper wall: (a) trajectory, (b) velocity, (c) angular velocity, and (d) number of bonds.

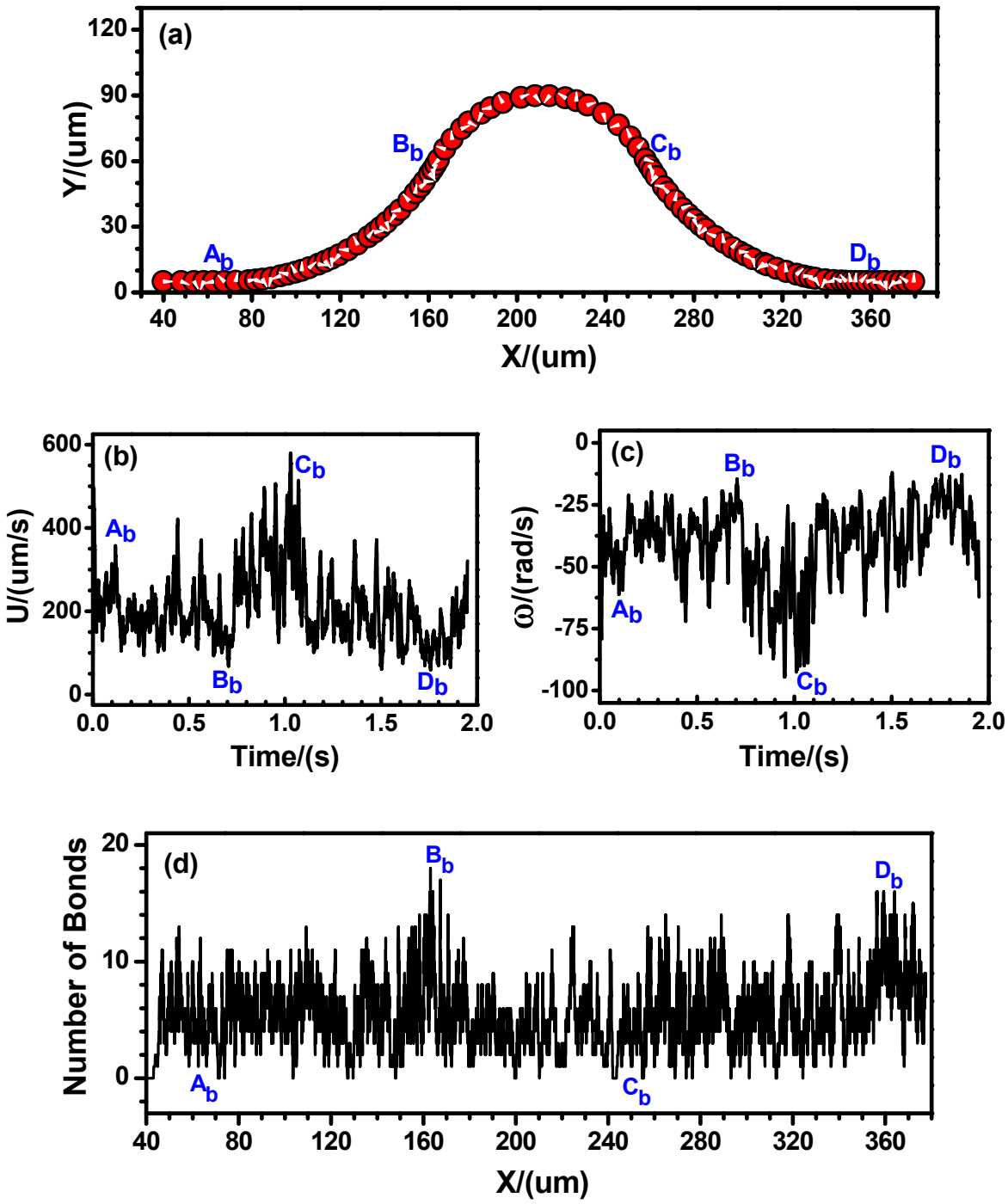

Figure 6.8 Case 2: the history of the cell released near the bottom wall: (a) trajectory, (b) velocity, (c) angular velocity, and (d) number of bonds

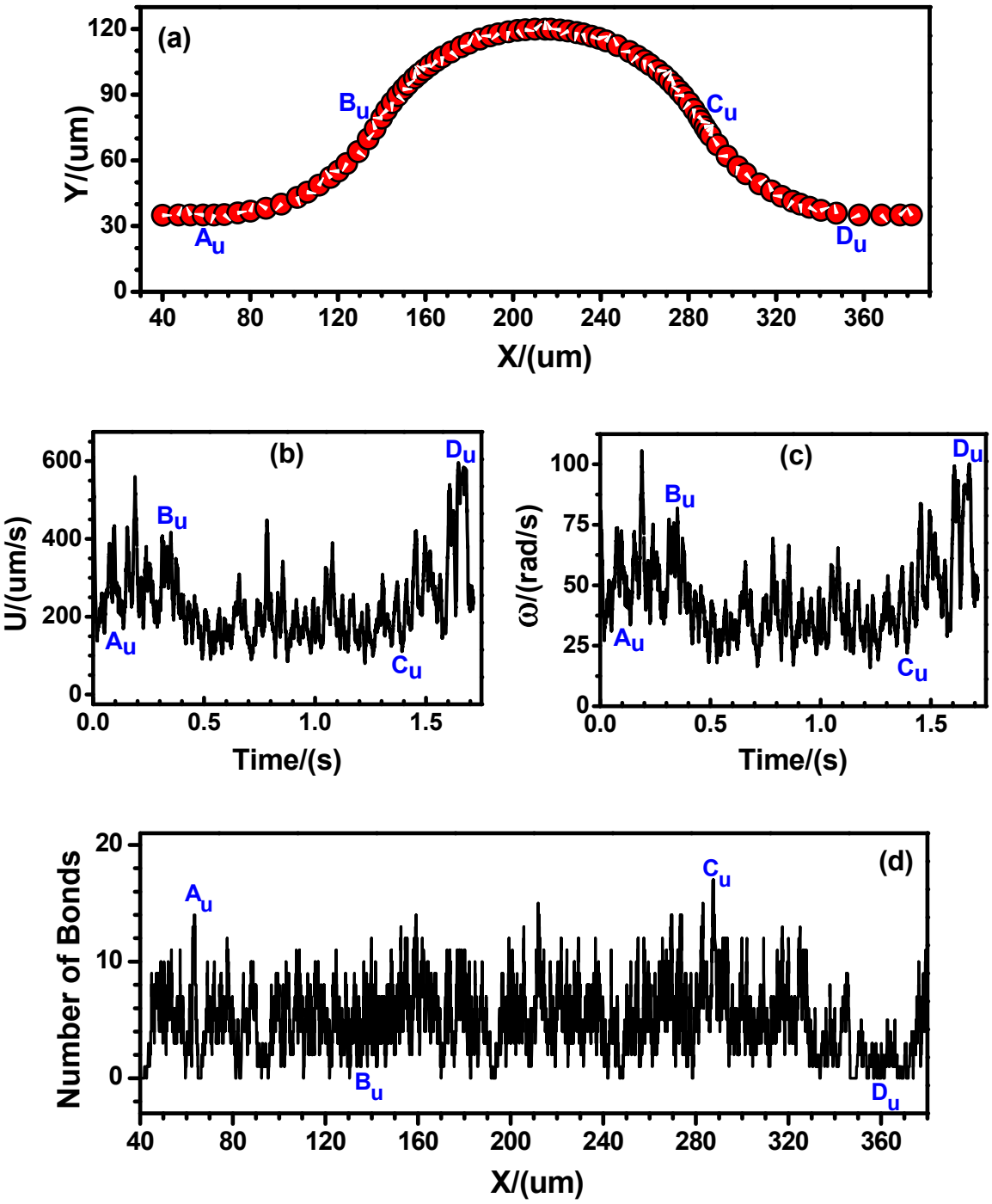

Figure 6.9 Case 2: the history of cell released near the upper wall: (a) trajectory, (b) velocity, (c) angular velocity, and (d) number of bonds.

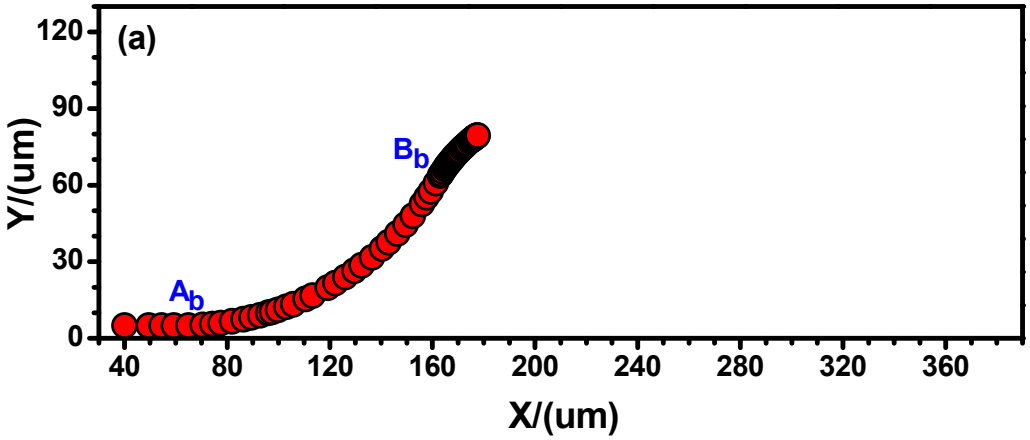
(a)
Y/(um)
X/(um)
A_b
B_b

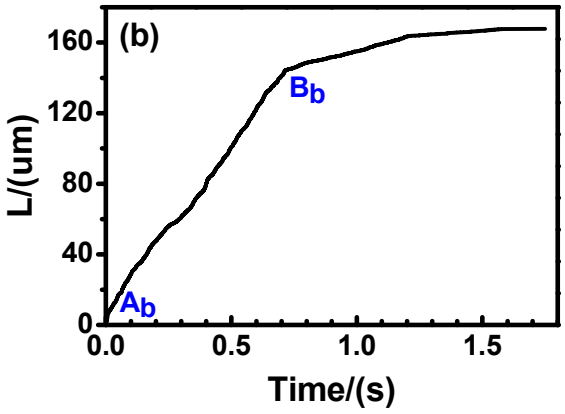
(b)
L/(um)
Time/(s)
A_b
B_b

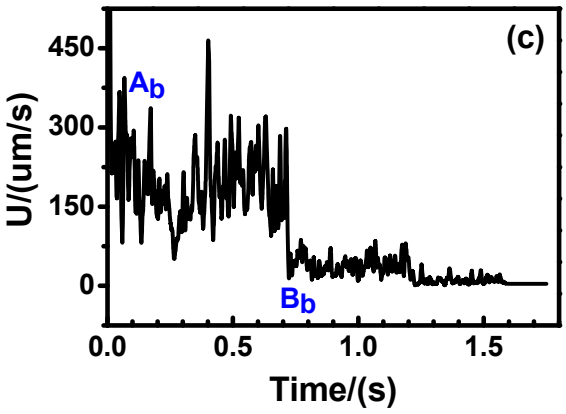
(c)
U/(um/s)
Time/(s)
A_b
B_b

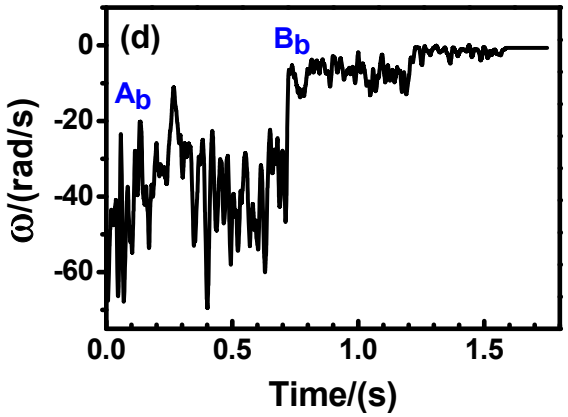
(d)
ω/(rad/s)
Time/(s)
A_b
B_b

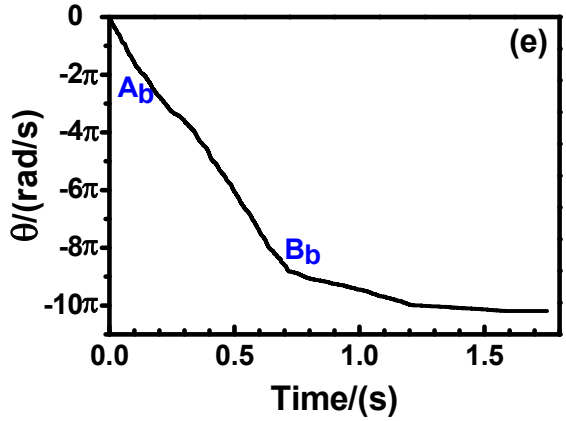
(e)
θ/(rad/s)
Time/(s)
A_b
B_b

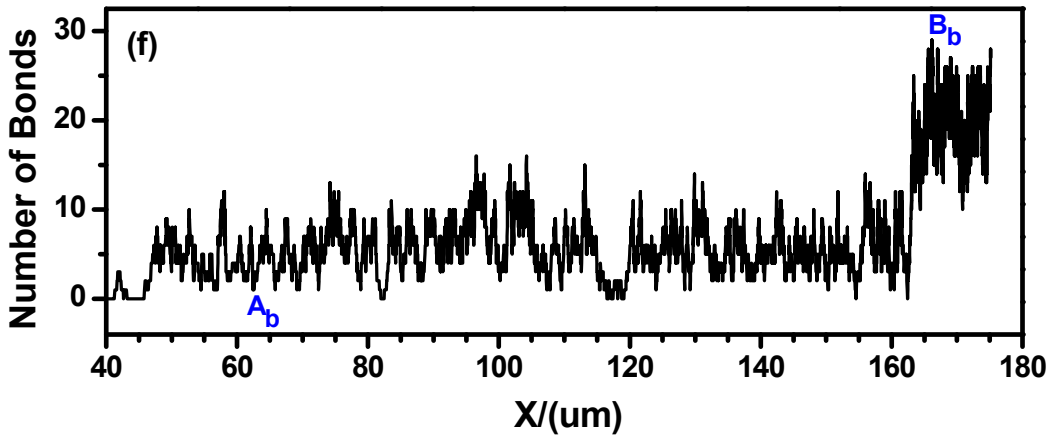

Figure 6.10 Case 3: the history of cell released near the bottom wall: (a) trajectory, (b) displacement, (c) velocity, (d) angular velocity, (e) angle, and (f) number of bonds

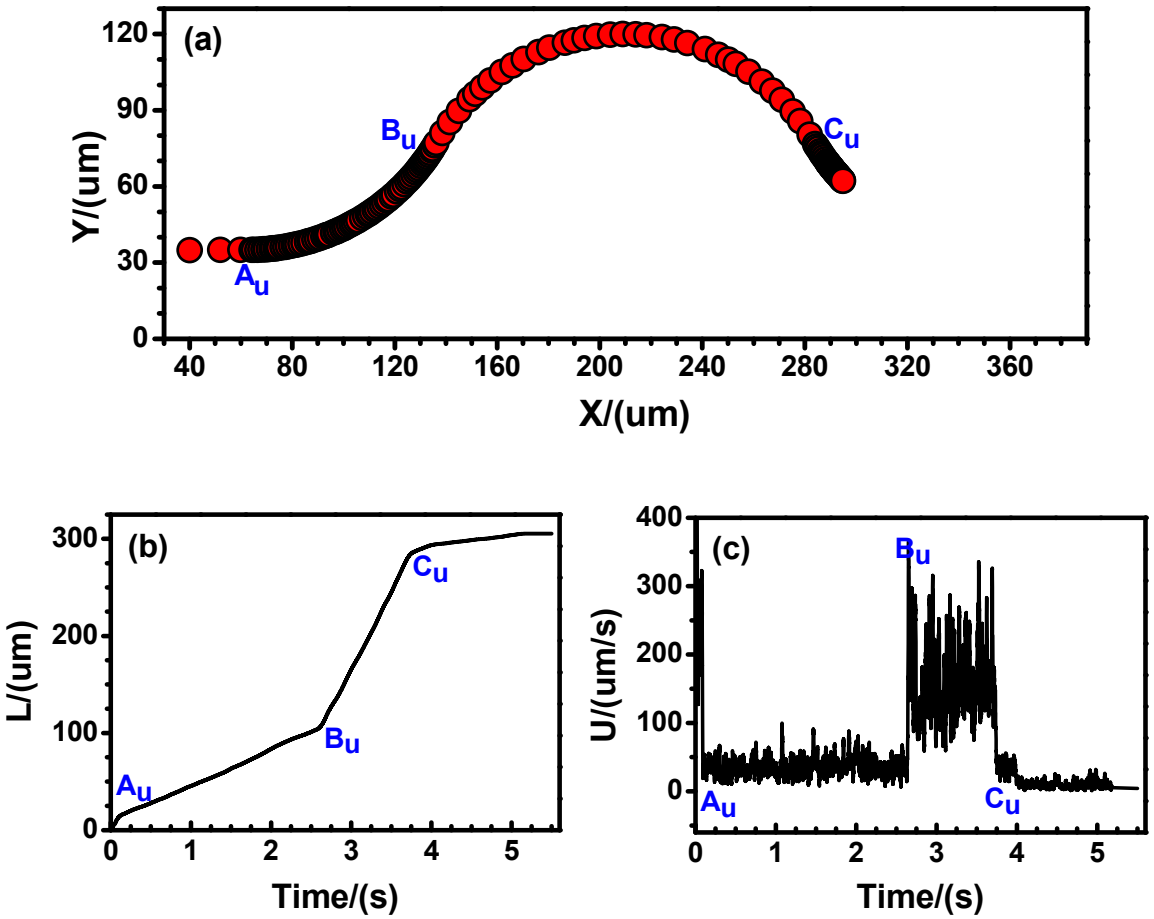

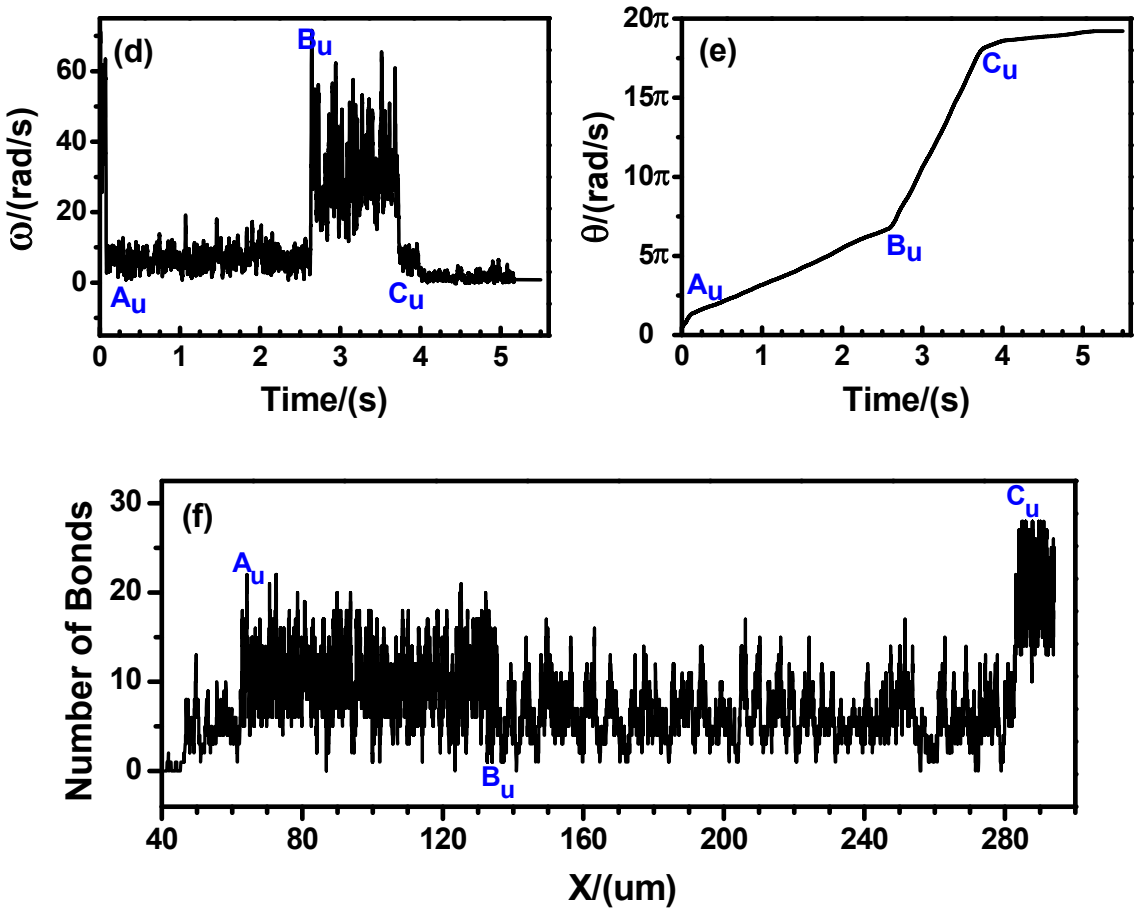

Figure 6.11 Case 3: the history of cell released near the upper wall. (a) trajectory, (b) displacement, (c) velocity, (d) angular velocity, (e) angle, and (f) number of bonds

6.8 Summary

The effects of the local wall shear stress and its gradient on tumor cell adhesion in the curved micro-vessel has been numerically studied by the LBM. A modified adhesive dynamics model was proposed to take into the consideration of the wall shear stress and its gradient in the receptor-ligand binding. Both cases when the tumor cell is released near the bottom wall and near the upper wall in a curved micro-vessel have been investigated. Combined with the observations from the in vivo tumor cell adhesion experiments which satisfied the simulation conditions

(e.g., negligible cell-cell interaction between tumor cells due to a controlled tumor cell perfusion rate of about one cell per second in the vessel), the simulation results lead to the following conclusions:

(1) The present numerical scheme that coupled the adhesive dynamics model into the LBM is capable of simulating different adhesion behavior states of the cell in the straight micro-vessels.

(2) The tumor cell adhesion requires a critical wall shear stress and its gradient in the curved micro-vessel. Once the wall shear stress and its gradient are superior to the critical value, it would trigger the bond association/dissociation rates to change; otherwise, the effect of wall shear stress/gradient on tumor cell adhesion can be neglected.

(3) The present revised models are capable of simulating the tumor cell adhesion phenomenon in the curved micro-vessel. From a physiological point of view, it can be deemed that the binding affinity of cell adhesion molecules would be enhanced or weakened by the variation of wall shear stress. If the wall shear stress and its gradient are positive and reach some threshold, the ECs lining the vessel wall and tumor cells would be activated to form more adhesive bonds. On the contrary, they would be inactivated by the negative wall shear stress and its gradient to weaken the capability of bond formation or accelerate the breakage of the previously formed bonds.

Chapter 7

Effect of Divalent Cations on Cell Adhesion between Human Neutrophil and Endothelial Ligand VCAM-1

The circulating blood cells, including neutrophils, are more likely adherent to the curved micro-vessels than the straight ones (Liu et al. 2008). Our previous work, which has been introduced in chapter 5 and chapter 6, indicated that the vessel curvature, cell-cell interaction, and wall shear stress/gradient would greatly affect this preferential adhesion in the curved micro-vessels. In addition, it has been found that the conformation affinity of integrins on neutrophils surfaces would be influenced by different divalent cations in extracelluar medium (Masumoto and Hemler 1993; Bazzoni et al. 1998), which provides an opportunity to explore the particular importance of integrins activation for neutrophils adhesion. In this chapter, we aim at numerically studying the effect of divalent cations, i.e. Mn^{2+}, Mg^{2+} plus EGTA, and Ca^{2+}, on VLA-4/VCAM-1 adhesion under blood flow conditions in both the straight and curved micro-vessels by the LBM.

In this work, the length of the straight micro-vessel is $L = 420\,\mu$m and the width is $D = 40\,\mu$m. The dimensions of the curved vessel are designed to be the same as that in chapter 6 (see Fig. 6.4). Where A, B, C and D (corresponding to A_b, B_b, C_b and D_b in Fig. 6.4) are the conjunctions of positive and negative curvatures. The simulation methods adopted here are the same as those in our previous studies (Yan et al. 2010ab). Likewise, the fluid dynamics was carried out by the LBM, and the cell dynamics was governed by the Newton's law of

translation and rotation. However, a special and complex adhesive dynamics model was used to consider the effect of VLA-4/VCAM-1 bonds on cell adhesion. This new model also involved the influence of wall shear stress gradient on receptor-ligand bonds based on the Dembo et al.'s model (1988) and the Bell's model (1978) of forward/reverse reaction rates. Here, we also used the cell of radius $R_c = 5.0\,\mu\text{m}$, a typical size of a traveling neutrophil in the blood vessels. The cell was driven by a pressure difference $\Delta p = 8.75$ Pa for the straight vessel and $\Delta p = 10.0$ Pa for the curved vessel, with which the pressure drop of both cases was about 0.02 $\text{Pa}/\mu\text{m}$. The simulation parameters and their values are tabulated in Table 7.1.

7.1 Neutrophil Adhesive Dynamics Models

An important contribution of integrins is their ability to mediate the adhesive states of neutrophils (Dustin and Springer 1991; Diamond and Springer 1994). In this study, we mainly consider two types of integrin-mediated neutrophil adhesion: (1) LFA-1/ICAM-1 adhesion; and (2) VLA-4/VCAM-1 adhesion. The chemical reaction between LFA-1 and ICAM-1 is the same as the general cell adhesion, which involves a single step reversible reaction of integrin binding to ICAM-1 (Chesla et al. 1998; Lomakina and Waugh 2004). However, there exists two steps leading to the formation of bonds for VLA-4/VCAM-1 adhesion (Waugh and Lomakina 2009; Lomakina and Waugh 2009). The first step involves the formation of a reaction zone, and the second step is the binding reaction itself. The adhesion process of VLA-4/VCAM-1 bonds is much more complex than that

of LFA-1/ICAM-1 bonds, which has been shown in Fig. 2.2 and discussed detailedly in chapter 2.

The adhesive dynamics models are integrated to take into account the effect of stochastic bonds on neutrophil adhesion. In adhesive dynamics models, the integrins on neutrophil surface are defined as receptors, and the adhesion molecules on endothelial substrate are defined as ligands. Once the distance between a receptor and an endothelial ligand ICAM-1 or VCAM-1 is smaller than the critical length H_c, there is a chance to form receptor-ligand bonds. In VLA-4/VCAM-1 adhesion, the kinetics of binding involves five coefficients: k^+ and k^- govern the formation of reaction zones from potential reaction zones, k_f and k_r represent the kinetics of forming or breaking a bond with a reaction zone, and k^-_{BI} characterizes the transition of a bond to the inactive zone. Based on the Dembo et al.'s model (1988) and Bell's model (1978), the refined reaction rates k_f and k_r that considered the wall shear stress gradient effect on neutrophils adhesion in the curved micro-vessels (Yan et al. 2010b) are,

$$k_f = k_f{}^0 \exp\left[-\frac{\sigma_{ts}(\chi-\lambda)^2}{2k_bT}\right]\cdot\exp\left(k_1\frac{d\tau}{dl}\right) \tag{7.1}$$

$$k_r = k_r^0 \exp\left[\frac{\gamma\sigma(\chi-\lambda)}{k_bT}\right]\cdot\exp\left(-k_2\frac{d\tau}{dl}\right) \tag{7.2}$$

where k_f^0 and k_r^0 are the unstressed association and dissociation rates, respectively. σ and σ_{ts} are the spring constant and transition state spring constant, respectively. k_b is the Boltzmann constant, T is the temperature, γ is the reactive

compliance, χ is the distance between a receptor and a ligand, and λ is the equilibrium bond length. $d\tau/dl$ is the wall shear stress gradient, and k_1 and k_2 are two parameters that represent the sensitivity of wall shear stress gradient to bond association and dissociation rates, respectively. This improved adhesive dynamics model reduces to the general Dembo et al.'s model and Bell's model in the straight vessels at $d\tau/dl = 0$. In addition, k^+, k^- and k^-_{BI} would also be regulated by the wall shear stress gradient in the curved vessels,

$$k^+ = k_0^+ \cdot \exp\left(k_1 \frac{d\tau}{dl} \right) \tag{7.3}$$

$$k^- = k_0^- \cdot \exp\left(-k_2 \frac{d\tau}{dl} \right) \tag{7.4}$$

$$k_{BI}^- = k_{BI0}^- \cdot \exp\left(-k_2 \frac{d\tau}{dl} \right) \tag{7.5}$$

where k_0^+, k_0^- and k_{BI0}^- are the kinetic coefficients in the straight vessels. Equations (7.3)-(7.5) mean that the wall shear stress gradient has sensitivity to the affinity state of integrin and the breakage of receptor-ligand bonds in the curved vessels. We assume that only the jumps or drops in the wall shear stress gradient can trigger the change of the kinetic coefficients. Once triggered, the reaction rates will keep the maximum/minimum value as calculated by equations (7.1)-(7.5) until the next wall shear stress gradient jump or drop occurs. The probabilities P_f, P_r, P^+, P^- and P^-_{BI} for reaction rates k_f, k_r, k^+, k^- and k^-_{BI} follows equations (2.6)-(2.10), respectively.

Table 7.1 Simulation parameters and their values

Parameter	Definition	Value (reference)
H_c	Critical length for formation	40 nm (Ref. [1])
ρ_f	Plasma density	1.03 g/cm^3 (Ref. [2])
ν	Plasma kinetic viscosity	1.2×10^{-6} m^2/s (Ref. [2]))
γ	Reactive compliance	4.0 Å (Ref. [3])
σ	Spring constant	2×10^{-3} N/m (Ref. [4])
σ_{ts}	Transition state spring constant	1×10^{-3} N/m (Ref. [4])
λ	Equilibrium bond length	20 nm (Ref. [4])
k_b	Boltzmann constant	1.38×10^{-23} J/K
T	Temperature	310 K (Ref. [4])
ρ_{LFA-1}	Density of LFA-1	50.0 /μm^2 (Ref. [5])
ρ_{VLA-4}	Density of VLA-4	5.0 /μm^2 (Ref. [6])
ρ_{ICAM-1}	Density of ICAM-1	290 /μm^2 (Ref. [5])
ρ_{VCAM-1}	Density of VCAM-1	200 /μm^2 (Ref. [6])
k_1	Sensitivity of wall shear stress gradient to association rate	1.0 μm /Pa (Ref. [7])
k_2	Sensitivity of wall shear stress gradient to dissociation rate	50.0 μm /Pa (Ref. [7])

Ref. [1]: Chang et al. 2000

Ref. [2]: Skalak and Chien 1987

Ref. [3]: Bell 1978

Ref. [4]: Chang and Hammer 1996

Ref. [5]: Lomakina and Waugh 2004.

Ref. [6]: Waugh and Lomakina 2009.

Ref. [7]: Yan et al. 2010b

7.2 LFA-1/ICAM-1 Adhesion in Mg^{2+} in the Straight Micro-vessel

The experimental studies of cell adhesion on immobilized neutrophils and endothelial substrate provide only part of what is needed to understand the dynamics and regulation of the adhesiveness of the cells for substrate. Therefore, we aim at studying adhesion between a circulating neutrophil and immobilized endothelial substrate. Since LFA-1 is the primary integrin on neutrophils surface and the fundamental endothelial ligand of LFA-1 is ICAM-1, we firstly simulate the LFA-1/ICAM-1 adhesion in the presence of Mg^{2+} plus EGTA under flow conditions. The choice of using Mg^{2+} plus EGTA to stimulate the high affinity form of LFA-1 is based on the fact that LFA-1 but not Mac-1 undergoes a marked increase in affinity for ICAM-1 under this condition (Altieri 1991; Diamond and Springer 1993). The forward and reverse reaction rates of LFA-1/ICAM-1 adhesion in Mg^{2+} plus EGTA have been quantified to be $k_f^{'0} = 3.4 \times 10^{-6}\,\mu\text{m}^2 \cdot \text{s}^{-1}$ and $k_r^0 = 0.07\text{s}^{-1}$ (Lomakina and Waugh 2004), and the unstressed association rate can be obtained by $k_f^0 = k_f^{'0} \times [\text{SUB}]$, where SUB is the density of ligand on the endothelial substrate. To observe LFA-1/ICAM-1 adhesion clearly, k_f^0 was normalized to be $84\,\text{s}^{-1}$, which is a reasonable value that can properly recreate experimental values for velocity and dynamics of rolling (Chang et al. 2000). The LFA-1/ICAM-1 adhesion in Mg^{2+} plus EGTA is carried out in the straight micro-vessel.

To form receptor-ligand bonds easily, the neutrophil is initially placed near the vessel wall with the nearest distance is 30 nm, which is within the range of

equilibrium bond length λ and critical length H_c. Figure 7.1 shows the history of LFA-1/ICAM adhesion in Mg^{2+} plus EGTA in the straight micro-vessel. Since cell adhesion is a stochastic process, the trajectory of the traveling neutrophil vibrates between 5.016 and 5.028 μm, which is illustrated in Fig. 7.1(a). It can be found that the cell never oscillates beyond the critical length, indicating that it always has the chance to create new bonds. Moreover, the cell never approaches to the vessel wall within 5.016 μm, owing to the strong repulsive van der Waals force induced by two surfaces in near contact. Figs. 7.1(b)-(c) show the cell velocity and angular velocity, both of which oscillate strongly during cell migration. The cell speed fluctuates between 0 and 800 μm/s, suggesting that the cell experiences a process with alternate "move" and "stop". The variation of the angular velocity is similar to that of the velocity. The large velocity and angular velocity indicate that the cell is in the state of "strong rolling". On the contrary, the small velocity and angular velocity mean that the cell is in the transient state of "firm adhesion". The total rotation angle of the cell is more than 20 π clockwise, which is shown in Fig. 7.1(d). Figure 7.1(e) displays the history of bonds number of the cell during the whole journey. It can be found that the number of receptor-ligand bonds varies greatly with the range from 0 to 25. The higher number of bonds means there is higher opportunity for the cell to be arrested by the vessel wall. The number of bonds highly depends on the cell trajectory, because it is the function of distance between the LFA-1 and endothelial ICAM-1.

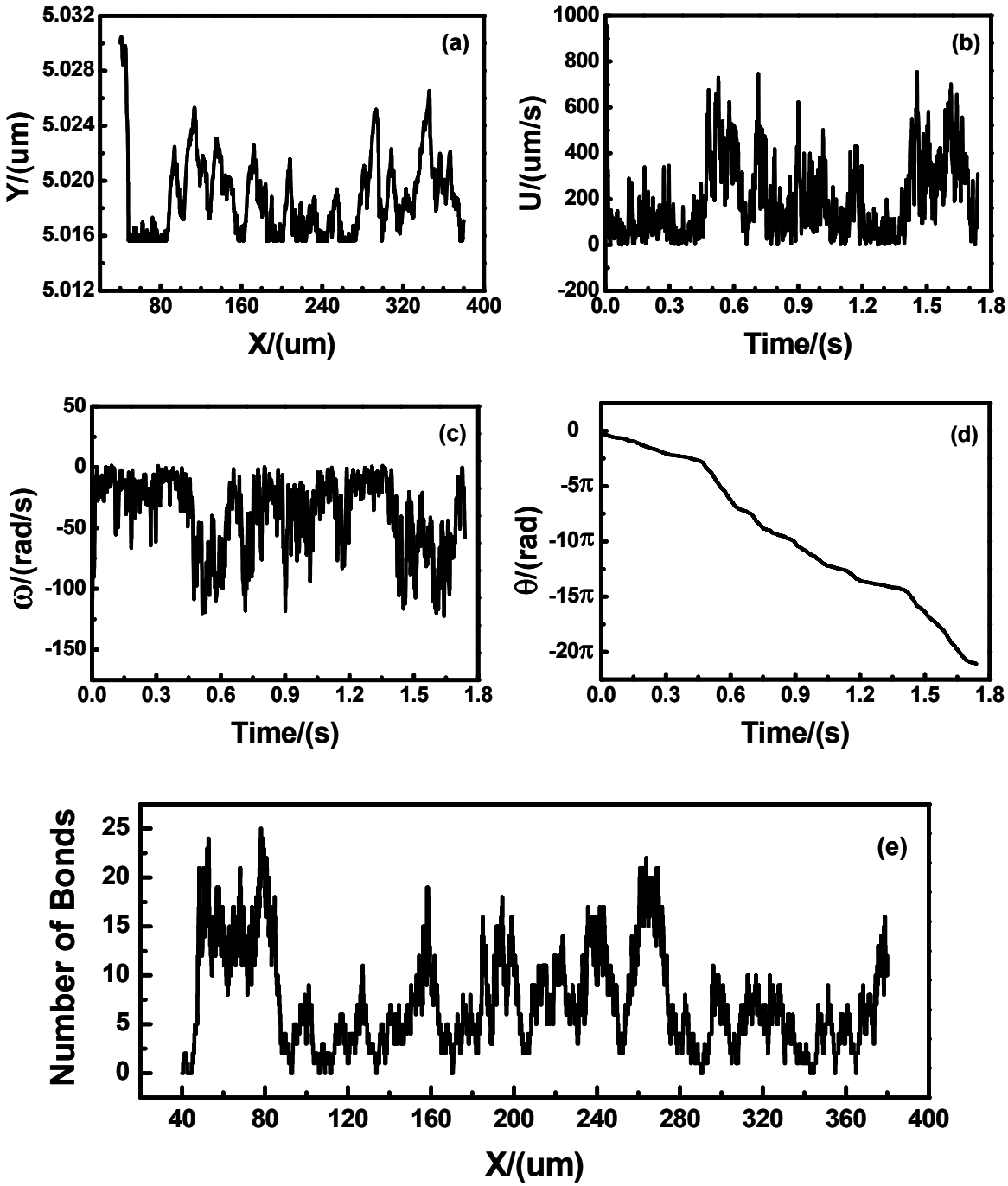

Figure 7.1 The history of LFA-1/ICAM adhesion in Mg^{2+} plus EGTA in the straight micro-vessel: (a) trajectory, (b) velocity, (c) angular velocity, (d) angle, and (e) number of bonds.

The adhesion between LFA-1 and ICAM-1 plays an important role in neutrophils adhesion. By comparing to LFA-1/ICAM-1 adhesion, we can predict the role of VLA-4/VCAM-1 bonds that plays in mediating neutrophils adhesion. In the next, we continue to discuss the effect of different divalent cations on VLA-4/VCAM-1 adhesion in both the straight and curved micro-vessel.

7.3 Effect of Divalent Cations on VLA-4/VCAM-1 Adhesion in the Straight Micro-vessel

It has been well known that the integrins affinity behaves differently in different divalent cations (Masumoto and Hemler 1993; Bazzoni et al. 1998). This feature provides a chance to study the particular importance of integrins activation for neutrophils adhesion in the absence of general activation of the cells (Lomakina and Waugh 2004). The divalent cations of Mg^{2+} plus EGTA, Mn^{2+}, and Ca^{2+} are often used to investigate neutrophils adhesion, owing to their significant abilities in changing integrins affinity for endothelial liangds. The mechanism for affinity modulation involves a conformational change of the VLA-4 receptor by the high concentrations of these divalent cations, and the enhanced adhesions are also association with the structural rearrangement of VLA-4 from a bent state (inactive state) to an extended conformer (active state). In the so-called switchable model, integrin activation augments VLA-4/VCAM-1 adhesion by increasing the effective density of VLA-4 on the neutrophils surface. The novel adhesive dynamic model for VLA-4/VCAM-1 adhesion and its kinetic coefficients in these divalent cations have been experimentally investigated (Waugh and Lomakina

2009; Lomakina and Waugh 2009). The kinetic coefficients and their values are tabulated in Table 7.2. Since k^- in Ca^{2+} was too large to be measured by the experiments, we use a comparative large value $k^- = 1000 s^{-1}$ in our simulations.

The history of VLA-4/VCAM-1 adhesion in the presence of Mg^{2+} plus EGTA, Mn^{2+} and Ca^{2+} in the straight vessel is shown in Fig. 7.2. From Fig. 7.2(a), it can be found that the neutrophil is translating and rotating along the vessel wall in Mn^{2+}, and the trajectories of cell in the other two divalent cations (not be shown) are similar to that in Mn^{2+}. Figs. 7.2(b)-(c) show the velocity and angular velocity of the cell in different divalent cations, respectively. It can be found that the cell speed in Mn^{2+} almost oscillates between 350 and 700 $\mu m/s$, and the variation in Ca^{2+} is much larger than that in Mn^{2+} which ranges from 350 to 1000 $\mu m/s$. The largest change of velocity occurs in Mg^{2+} plus EGTA which fluctuates between 200 and 1000 $\mu m/s$. There are also fluctuations in angular velocity of the cell with the range from -120 to 70 rad/s in Mn^{2+} and from -130 to -70 rad/s in Ca^{2+}. Like that in Ca^{2+}, the most angular velocity in Mg^{2+} plus EGTA oscillates between -130 and -70 rad/s, and very few even reaches to -50 rad/s due to the strong cell adhesion that result from the comparatively small k^-_{BI}, which would significantly influence the breakage of bonds. The difference profiles in cell speed and angular speed are caused by the different abilities of divalent cations in changing affinity form of integrins for their liangds. The total rotation angle of the cell is illustrated in Fig. 7.2(d). For the same displacement, the cell rotation angle in Ca^{2+} and Mg^{2+} plus EGTA is about 16π clockwise, and the larger angle occurs

in Mn^{2+} with approximately 21π clockwise due to more obvious cell adhesion in this situation.

The number of bonds in these divalent cations is shown in Fig. 7.2(e). It can be clearly found that most of the number of bonds in Mn^{2+} fluctuates between 0 to 4, and few reaches up to 5. The bonds number in Ca^{2+} is comparatively thinner, and the maximum value of bonds number is only 3, owing to the larger k^+ and lower k^- in Mn^{2+}. k^+ and k^- should be the most important coefficients that determine the formation of active reaction zones, which are the prerequisite for bond formation to occur. Compare to that in Ca^+, the number of bonds in Mg^{2+} is much thinner which means the less ability in creating new bonds in this situation. Since the k^-_{BI} in Mg^{2+} is considerably less than that in Ca^+, the maximum bonds number in Mg^{2+} can reach up to 4. From the above discussions, it can be concluded that the Mn^{2+} has the highest ability in changing affinity state of VLA-4 for their endothelial ligand VCAM-1 under flow condition, and the higher integrin activation capability occurs in the presence of Mg^{2+}, which is a little stronger than that in Ca^{+2}.

Table 7.2 Kinetic coefficients of VLA-4/VCAM-1 adhesion in different divalent cations

Parameter	Definition	Value (reference)		
		Mn^{2+}	Mg^{2+}	Ca^{2+}
k_0^+	Reaction rate from PRZ to RZ	1.3×10^{-2} s^{-1} Ref. [1]	1.2×10^{-3} s^{-1} Ref. [1,2]	2.7×10^{-3} s^{-1} Ref. [1]
k_0^-	Reaction rate from RZ to PRZ	1.65 s^{-1} Ref. [1]	0.25 s^{-1} Ref. [1, 2]	too large to be measured. Ref.[1]
$k_f^{'0}$	Unstressed association rate	$0.0051\mu m^2\cdot s^{-1}$ Ref. [1, 2]	$0.0051\mu m^2\cdot s^{-1}$ Ref. [1, 2]	$0.0051\mu m^2\cdot s^{-1}$ Ref. [1, 2]
k_r^0	Unstressed dissociation rate	0.13 s^{-1} Ref. [2, 3]	0.13 s^{-1} Ref. [2, 3]	0.13 s^{-1} Ref. [2, 3]
k^-_{BI0}	Reaction rate from ZB to PRZ	0.30 s^{-1} Ref. [1]	0.066 s^{-1} Ref. [1, 2]	0.43 s^{-1} Ref. [1]

Ref. [1] Lomakina and Waugh 2009.

Ref. [2] Waugh and Lomakina 2009.

Ref. [3] Zhang et al. 2004.

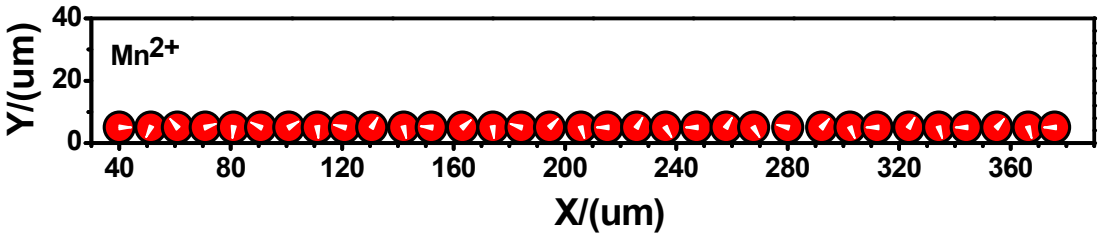
Mn2+
Y/(um)
X/(um)
40
20
0
40
80
120
160
200
240
280
320
360

(a)

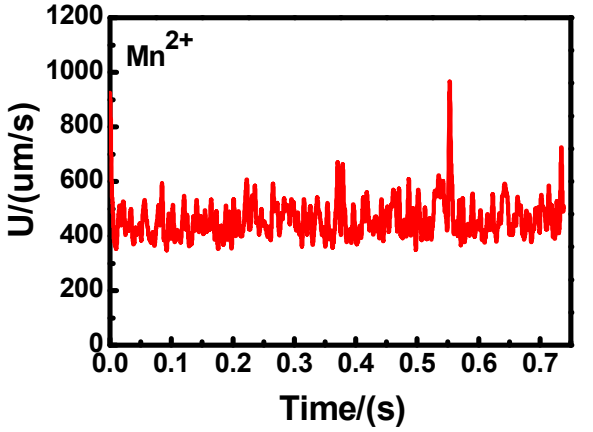
Mn2+
U/(um/s)
Time/(s)
1200
1000
800
600
400
200
0
0.0
0.1
0.2
0.3
0.4
0.5
0.6
0.7

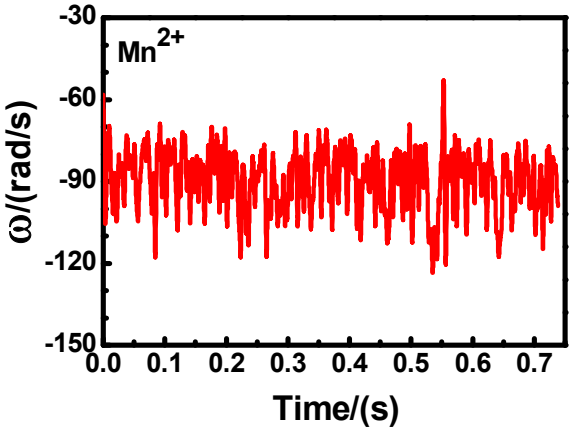
Mn2+
ω/(rad/s)
Time/(s)
-30
-60
-90
-120
-150
0.0
0.1
0.2
0.3
0.4
0.5
0.6
0.7

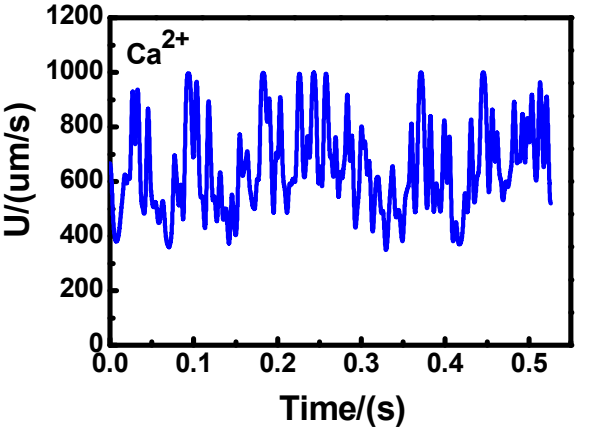
Ca2+
U/(um/s)
Time/(s)
1200
1000
800
600
400
200
0
0.0
0.1
0.2
0.3
0.4
0.5

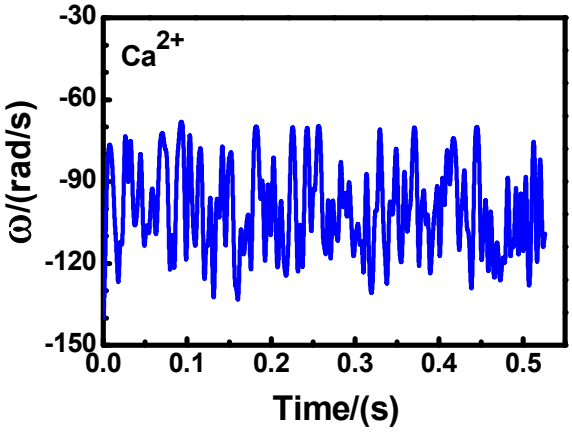
Ca2+
ω/(rad/s)
Time/(s)
-30
-60
-90
-120
-150
0.0
0.1
0.2
0.3
0.4
0.5

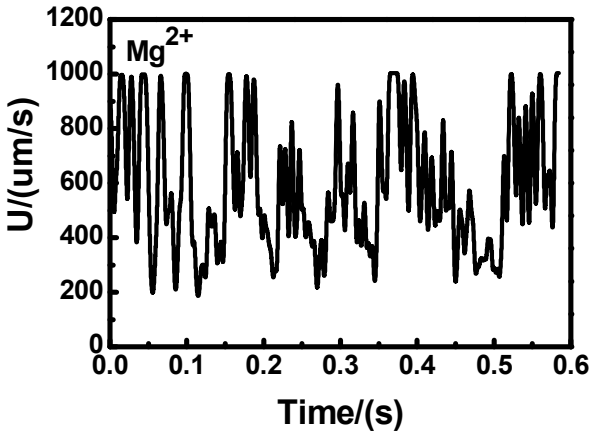
Mg2+
U/(um/s)
Time/(s)
1200
1000
800
600
400
200
0
0.0
0.1
0.2
0.3
0.4
0.5
0.6

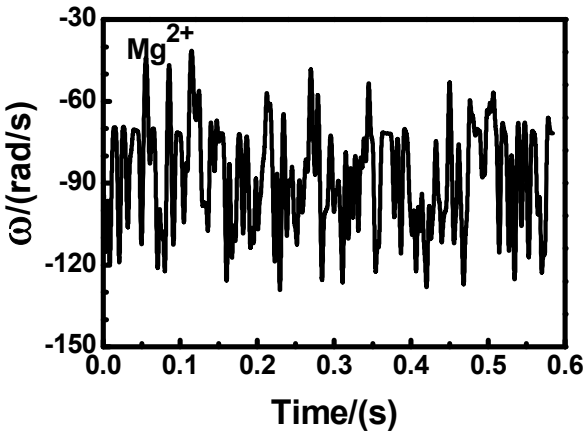
Mg2+
ω/(rad/s)
Time/(s)
-30
-60
-90
-120
-150
0.0
0.1
0.2
0.3
0.4
0.5
0.6

(b)

(c)

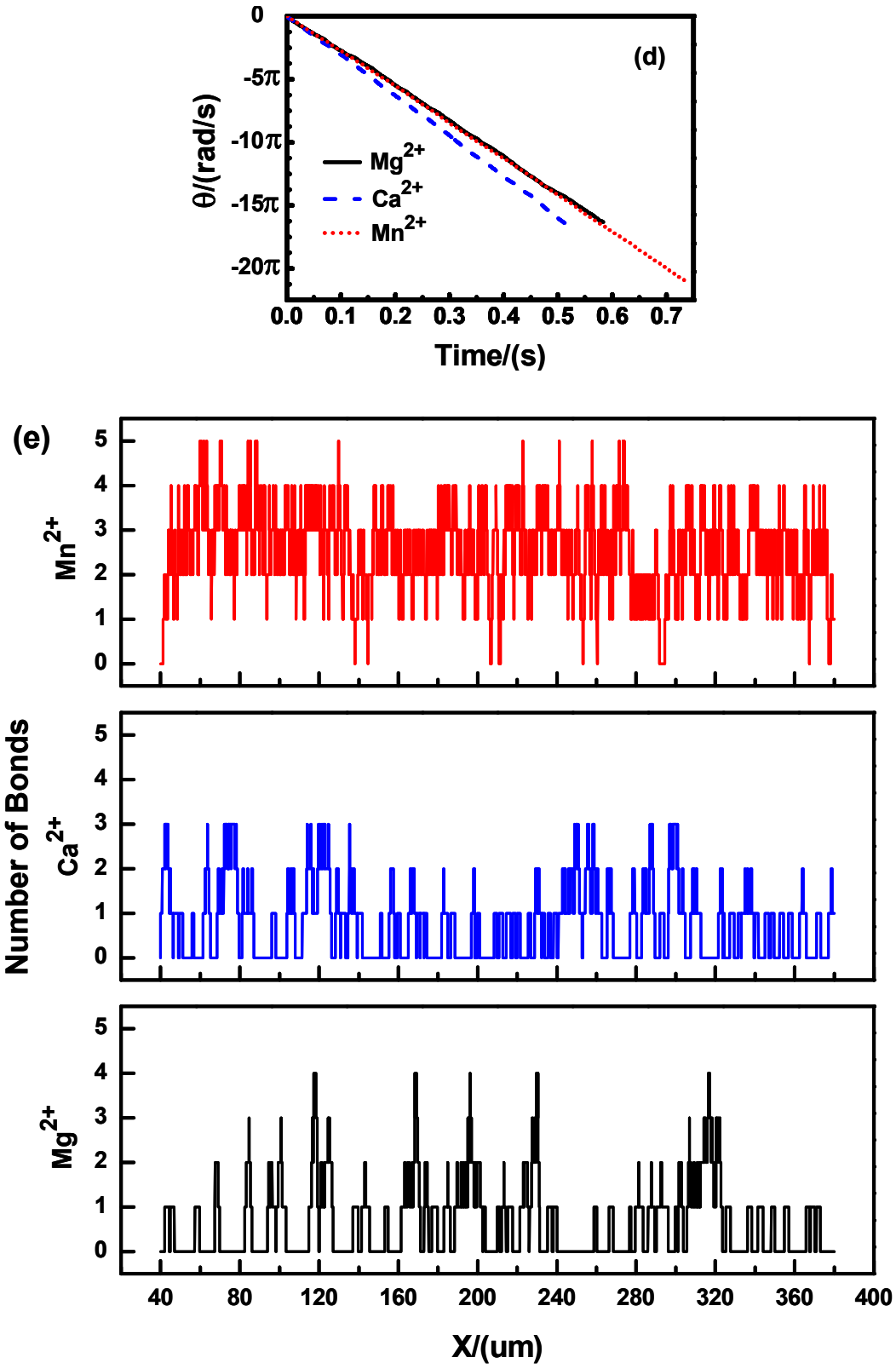

Figure 7.2 The history of VLA-4/VCAM-1 adhesion in different divalent cations in the straight micro-vessel: (a) trajectory, (b) velocity, (c) angular velocity, (d) angle, and (e) number of bonds

7.4 Effect of Divalent Cations on VLA-4/VCAM-1 Adhesion in the Curved Micro-vessel

In real physiological conditions, neutrophils adhesion always occurs in the curved blood vessels. The neutrophils adhesive dynamics model, which is taken into account the integrated effects of vessel curvature, wall shear stress gradient, and divalent cations, will much more comprehensive to reflect the stochastic and complicated biophysical process of cell adhesion in real situations. In the next, the influence of divalent cations on VLA-4/VCAM-1 adhesion is examined in the curved micro-vessel.

Figure 7.3 shows the history of VLA-4/VCAM-1 adhesion under the effect of different divalent cations in the curved micro-vessel. Figure 7.3(a) illustrates the trajectory of neutrophil with both translation and rotation in Mn^{2+}, from which one can found that the apparent cell adhesion occurs once the cell passes the conjunction B. More obvious cell adhesion takes place between the conjunctions A and B due to the great effect of vessel curvature there. The cell trajectories (not be shown) in other two divalent cations are roughly similar to that in Mn^{2+}. There are strong oscillations in both cell velocity and angular velocity, which are shown in Figs. 7.3(b)-(c). In Mn^{2+}, both of the velocity and angular velocity vary greatly at the conjunctions B and C, owing to the significant changes of bonds reaction rates there. In Ca^{2+}, the strong vibrations occur from t = 0 to 0.08 s, and then following comparatively smooth velocity and angular velocity, indicating that the cell leaves the vessel wall and becomes a free cell. The velocity and angular

velocity in Mg^{2+} is much more complex, which firstly fluctuate strongly between 0 and 1000 μm / s and between 0 and -100 rad/s from t = 0 to 0.65 s and then become much smoother since there is no cell adhesion at all. Figure 7.3(d) illustrates the rotation angle of the migrating cell. It can be found that the cell rotates approximately 10 π clockwise in Ca^{2+}, 13 π clockwise in Mg^{2+}, and 21 π clockwise in Mn^{2+}.

Figure 7.3(e) shows the history of bonds number of the cell in three divalent cations. It can be easily found that the most obvious cell adhesion occurs in Mn^{2+}, and the comparative evident cell adhesion happens in Mg^{2+} plus EGTA, which is much superior to that in Ca^{2+}. In Mn^{2+}, the number of bonds between the conjunctions A and B is almost oscillating between 1 and 4, and few reaches to 5 due to the strong vessel curvature effect there. Between B and C, lots of bonds number arrives at 5, suggesting that there will be very large probability of cell arrest caused by the great jump of wall shear stress gradient there. Once the cell gets to C, the number of bonds decreases and vibrates between 0 and 4, owing to the significant drop of wall shear stress gradient there. The cell finally becomes free and there is no cell adhesion. The number of bonds in Mg^{2+} plus EGTA varies between 0 and 5, and it keeps zero since $x \approx 190.0\ \mu$m . The cell adhesion in Ca^{2+} is rather weak, it only maintains from 40 to 90 μm , and then all the old bonds are broken and no new bond is created.

The statistical average physical quantities for both LFA-1/ICAM-1 and VLA-4/VCAM-1 adhesions in different divalent cations in both the straight and

curved micro-vessel are tabulated in Table 7.3. The adhesion probability is defined as the number of contacts for which adhesion occurred divided by the total number of contacts. From the data, one can found that the average bonds number of LFA-1/ICAM-1 adhesion is about 11.15, which is highly larger than that of VLA-4/VCAM-1 adhesion with 2.65 in Mn^{2+}, 1.22 in Mg^{2+}, and 1.15 in Ca^{2+} in the straight vessels. However, the adhesion probability of VLA-4/VCAM-1 adhesion is 44.14% in Mn^{2+}, 20.26% in Mg^{2+}, and 19.13% in Ca^{2+}, all of which is superior to that of VLA-4/VCAM-1 adhesion with 18.58% in Mg^{2+} in the straight micro-vessel. It can also be found that the highest affinity state of VLA-4 to VCAM-1 occurs in Mn^{2+}, and following that are Mg^{2+} plus EGTA and Ca^{2+} for both the straight and curved micro-vessels. Surprisingly, the adhesion probabilities in Mn^{2+} and Ca^{2+} in the curved micro-vessel are less than these in the straight micro-vessel, this is result from the variation of shear stress gradient which enforce the cell to leave the vessel wall and become a free cell without adhesion.

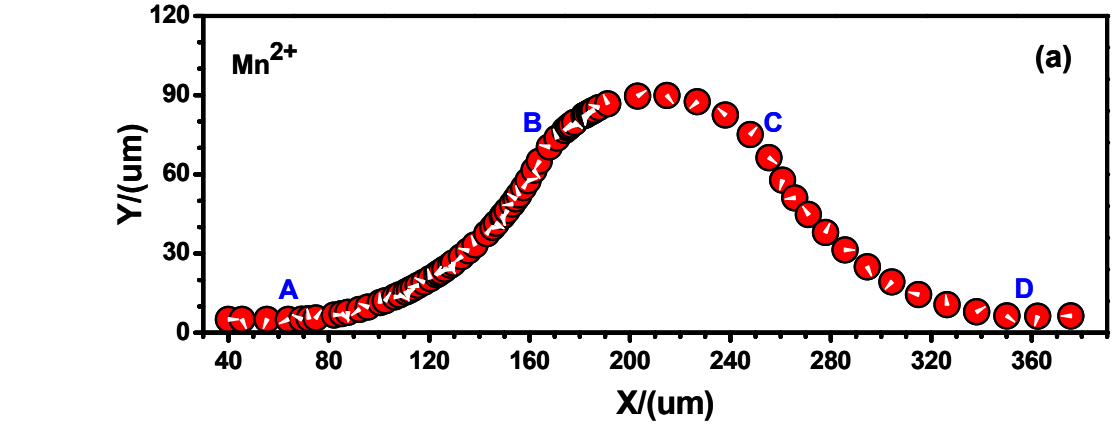
Mn2+
(a)
A
B
C
D
Y/(um)
X/(um)

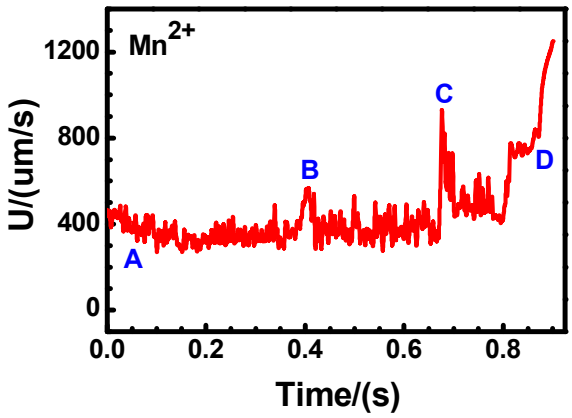
Mn2+
A
B
C
D
U/(um/s)
Time/(s)

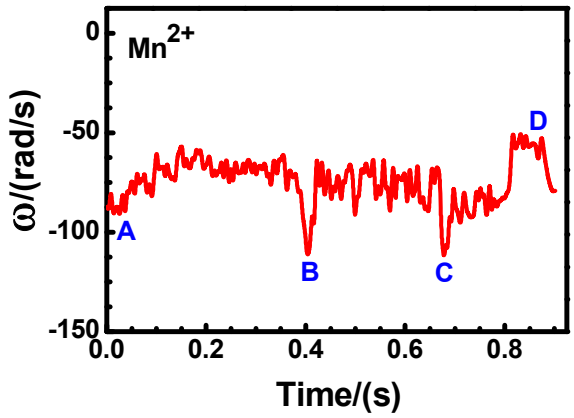
Mn2+
A
B
C
D
ω/(rad/s)
Time/(s)

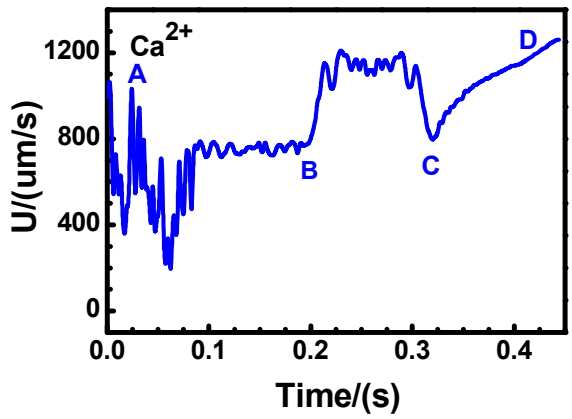
Ca2+
A
B
C
D
U/(um/s)
Time/(s)

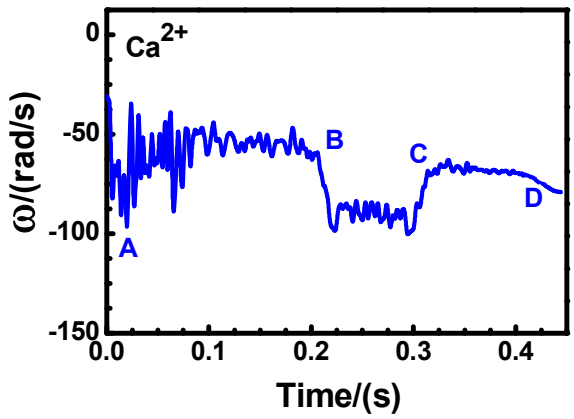
Ca2+
A
B
C
D
ω/(rad/s)
Time/(s)

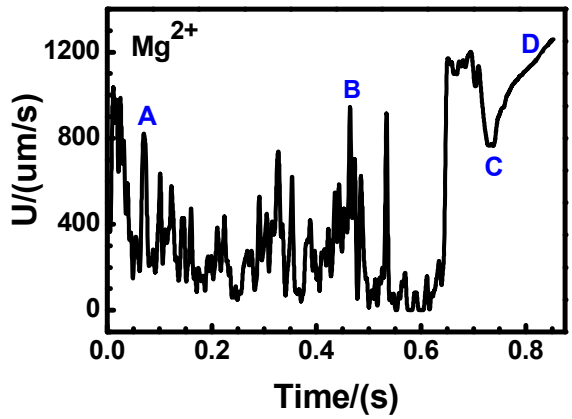
Mg2+
A
B
C
D
U/(um/s)
Time/(s)

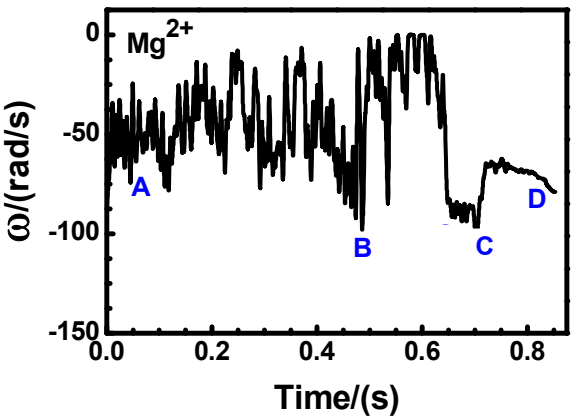
Mg2+
A
B
C
D
ω/(rad/s)
Time/(s)

(b) (c)

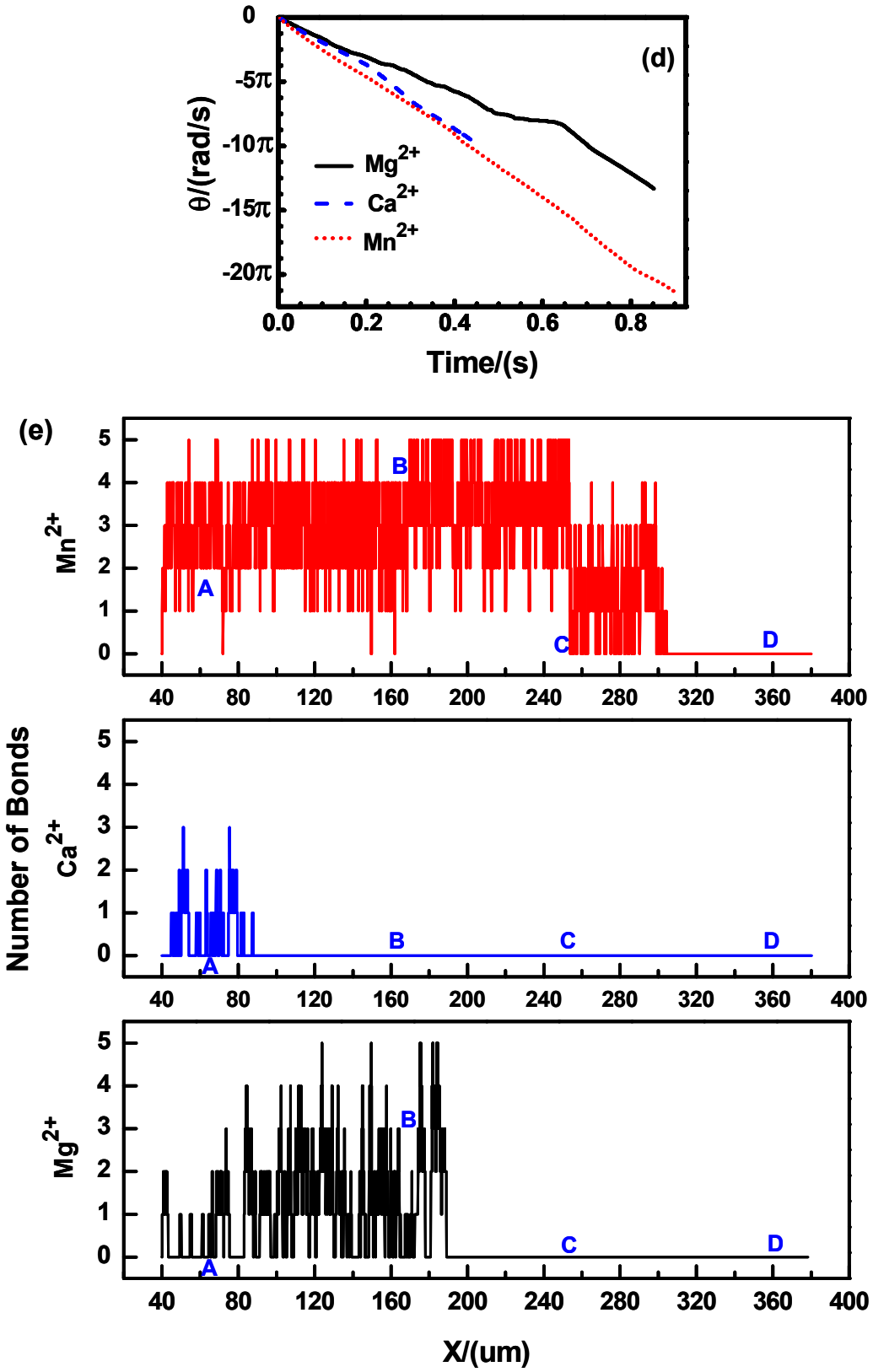

Figure 7.3 The history of VLA-4/VCAM-1 adhesion in different divalent cations in the curved micro-vessel: (a) trajectory, (b) velocity, (c) angular velocity, (d) angle, and (e) number of bonds

Table 7.3 Comparisons between LFA-1/ICAM-1 and VLA-4/VCAM-1 adhesions in different divalent cations in the straight/curved micro-vessels

Average physical quantity	**LFA-1/ICAM**	**VLA-4/VCAM-1**					
	Mg^{2+}	Mn^{2+}		Mg^{2+}		Ca^{2+}	
	straight	straight	curved	straight	curved	straight	curved
Number of bonds	11.15	2.65	2.56	1.22	1.46	1.15	0.17
Adhesion probability	18.58%	44.14%	42.6%	20.26%	26.7%	19.13%	2.8%

7.5 Summary

The integrin-mediated neutrophils adhesion under hydrodynamic flow conditions has been numerically studied by the LBM. Specially, the LFA-1/ICAM-1 adhesion in Mg^{2+} plus EGTA in the straight vessel and the VLA-4/VCAM-1 adhesion in different divalent cations in both the straight and curved vessels have been examined. The normal dynamic model was adopted to simulate LFA-1/ICAM-1 adhesion, and the novel dynamic model was applied to model VLA-4/VCAM-1 adhesion. The effect of wall shear stress gradient on VLA-4/VCAM-1 adhesion was also taken into account in the curved vessel. The simulation results lead to the following conclusions:

(1) Divalent cations, i.e. Mn^{2+}, Mg^{2+} plus EGTA and Ca^{2+}, significantly influence the neutrophils adhesion under blood flow conditions. Among them, Mn^{2+} has the largest capability in stimulating the affinity state of VLA-4 to endothelial

ligand VCAM-1, and the larger ability of that occurs in Mg^{2+} plus EGTA, which is superior to that in Ca^{2+}. This result agrees well with the experimental outcomes that performed on immobilized integrins of neutrophils and their liangds without blood flowing.

(2) Compare to the LFA-1/ICAM-1 adhesion, the VLA-4/VCAM-1 adhesion is weaker in neutrophils adhesion due to the comparative thinner distribution of VLA-4 on neutrophils surface. However, the adhesion probability of VLA-4/VCAM-1 bonds, especially in the presence of Mn^{2+}, would be larger than that of LFA-1/ICAM-1 bonds under blood flow conditions.

(3) Neutrophils adhesion is a rather complex process, which involves numerous factors, i.e. divalent cations, vessel curvature and wall shear stress gradient, to regulate its functions under flow conditions. The present results would be helpful to understand the neutrophils adhesion under real physiological situations.

Chapter 8 Conclusion and Future Work

8.1 Conclusion

Cell adhesion is one of the most fascinating aspects of cell function in the microcirculation of biological systems. It is of significant importance to investigate the mechanical mechanisms of cell adhesion under hydrodynamic conditions. The LBM effectively connects macroscopic and microscopic scales, and thereby suitable to solve the biophysical modeling of cell adhesion from the micrometer down to the molecular level. A comprehensive biophysical description of cell adhesion in microcirculation would allow development of new treatment strategies for many diseases, such as thrombosis, atherosclerosis, arthritis, and cancer. In this thesis, several critical factors, i.e. vessel curvature, cell-cell interaction, wall shear stress variation and divalent cations, for cell adhesion have been numerically studied and detailedly discussed. The fluid dynamics is carried out by the LBM, the cells dynamics is solved by the Newton's law of translation and rotation, and the adhesive dynamics models are involved to consider the effects of stochastic receptor-ligand bonds on cell adhesion.

Firstly, the effects of vessel curvature and cell-cell interaction on cell adhesion in both the straight and curved micro-vessels have been numerically studied. The numerical results lead to the following conclusions:

(1) The local geometry or the vessel curvature has significant influence on bond formation between the traveling cells and endothelium at the vessel wall. Usually, the simultaneous bond number would increase in a curved vessel,

and consequently the probability of cell adhesion is increased as well.

(2) The interaction between the traveling cells is significant, and the cell-2 (rear) would experience higher wallward force, which would enhance the receptor-ligand binding, consequently, this interaction would increase the cell adhesion probabilities.

(3) From a physiological point of view, most of the micro-vessels are either curved or bifurcated and there are always multiple cells traveling in the same vessel. The above conclusions indicate that the study of the single cell adhesion in a straight vessel may underestimate the capability of cell adhesion in the micro-vessels under real physiological and pathological conditions.

This work would be helpful to explain the mechanical mechanism of the strange biological phenomena why the circulating blood cells and tumor cells are more easily gathering near the bent of vessels.

Secondly, the effect of vessel wall shear stress gradient on cell adhesion in the curved micro-vessels with very low Reynolds number laminar flow has been both experimentally and numerically investigated. We also develop a novel adhesive dynamics model that coupled the effect of wall shear stress gradient on receptor-ligand bindings, in which the positive shear stress gradient jump would stimulate cell adhesion while the negative shear stress gradient jump would weaken cell adhesion. The numerical results lead to the following conclusions:

(1) The present numerical scheme that coupled the general adhesive dynamics

model into the LBM is capable of simulating different adhesion behavior states of the cell in the straight micro-vessels.

(2) There would be a critical wall shear stress gradient in the curved micro-vessels. Once the wall shear stress gradient is superior to the critical value, it would trigger the bonds association and dissociation rates to change; otherwise, the effect of wall shear stress gradient on cell adhesion can be neglected.

(3) The present revised model is capable of simulating the cell adhesion phenomenon in the curved micro-vessels. From a physiological point of view, it can be deemed that the adhesion molecules would be stimulated or weakened by the variation of wall shear stress. If the wall shear stress gradient is positive and reaches up to some threshold, the adhesion molecules will be activated to prepare more receptors or ligands to form bonds. On the contrary, the adhesion molecules will be inactivated by the negative wall shear stress gradient to weaken the capability of bonds formation or accelerate the breakage of the previously formed bonds.

This work not only would help us to understand the quantitative relationship between wall shear stress and tumor cell adhesion, but also elucidate why the tumor cell adhesion always occurs at the positive curvature in the curved vessels.

Finally, the effect of divalent cations on cell adhesion between the human neutrophil and endothelial ligand VCAM-1 in both the straight and curved micro-vessels has been numerically analyzed. The numerical calculations lead to the following conclusions:

(1) The divalent cations, i.e. Mn^{2+}, Mg^{2+} plus EGTA and Ca^{2+}, significantly influence the neutrophils adhesion under hydrodynamic conditions. Among them, the larger ability of stimulating the affinity state of VLA-4 to VCAM-1 occurs in Mg^{2+} plus EGTA than that in Ca^{2+}, and the largest capability occurs in Mn^{2+}. This result agrees well with the experimental outcomes that performed on immobilized integrins of neutrophils and their ligands without fluid flowing.

(2) Compare to the LFA-1/ICAM-1 adhesion, the VLA-4/VCAM-1 adhesion is much weaker in neutrophils adhesion due to the comparative thinner distribution of VLA-4 on the neutrophils surface. However, the adhesion probability of VLA-4/VCAM-1 bonds, especially in Mn^{2+}, would be larger than that of LFA-1/ICAM-1 bonds.

(3) Neutrophils adhesion is a rather complex process, which involves numerous factors, i.e. divalent cations, vessel curvature and wall shear stress gradient, to regulate its functions under flow conditions. The present results would be helpful to understand the neutrophils adhesion under real physiological situations.

This would help us to understand the mechanical mechanisms of integrin-mediated neutrophils adhesion in the presence of different divalent cations under dynamic flow conditions.

8.2 Future Work

Cell adhesion is a rather complicated process in the microcirculation of biological systems. Our work is only the tip of the iceberg, which provides only part of what is needed to understand the comprehensive cell adhesion in the real physiological and pathological situations. New developments and improvements are imperative for studying the cell adhesion in both the experiments and numerical models. As to the experimental aspects, we will continue keeping good cooperation with the research group of Prof. Fu Bingmei, who are at the Department of Biomedical Engineering, The City College of the City University of New York. As to the numerical models, we will mainly focus on the following aspects:

(1) To design complex bifurcated 3-D blood vessels.

In the real physiological conditions, the blood vessels are curved, bifurcated and three dimensional. It has been known that the breast tumor cell prefers to arrest in the lung microvasculature with lots of bends and branches. Therefore, bifurcations would play important roles in cell adhesion, and thereby it is necessary to design complex 3-D blood vessels with bifurcations for studying cell adhesion.

(2) To consider the effect of cell deformation on cell adhesion.

In the real physiological conditions, both the circulating blood cells and tumor cells are deformable. It is a limitation in our work that we idealize the traveling cells to be rigid. The immersed boundary condition method will be adopted to solve the deformable and elastic boundary of the cells, and then take into

account the effect of cell deformation on cell adhesion.

(3) To develop novel adhesive dynamics models for cell adhesion in different physiological and pathological situations.

The generalized adhesive dynamics models are widely accepted and applied by the researchers for the general phenomena of cell adhesion. However, new unknown pathologies will be found, and therefore, new adhesive dynamics models which can precisely reflect the mechanisms of these pathologies are needed. For example, we recently have focused on a strange phenomenon that the haematopoietic stem cells release is regulated by circadian oscillations. Obviously, the generalized adhesive dynamics models are not available for this phenomenon of cell adhesion.

Reference

Agresar G. 1996. A computational environment for the study of circulating cell mechanics and adhesion, Ph.D thesis, The University of Michigan

Aidun C.K., Lu Y. and Ding E.J. 1998. Direct analysis of particulate suspensions with inertia using the discrete Boltzmann equation, J. Fluid Mech., 373, 287-311

Allen M.P. and Tildesley D.J. 1987. Computer Simulation of Liquid, Clarendonn.

Alon R., Hammer D.A. and Springer T.A. 1995. Lifetime of the P-selectin-carbohydrate bond and its response to tensile force in hydrodynamic flow, Nature, 374, 539-542

Alon R., Kassner P.D., Carr M.W., Finger E.B., Hemler M.E. and Springer T.A. 1995. The integrin VLA-4 supports tethering and rolling in flow on VCAM-1. J. Cell Biol., 128, 1243-1253

Altieri D.C. 1991. Occupancy of CD11b/CD18 (Mac-1) divalent ion binding site(s) induces leukocyte adhesion. J. Immunol., 147, 1891-1898

Batchelor G.K. 1970. An introduction to fluid dynamics, Cambridge, University Press, New York

Bazzoni G., Ma L., Blue M.L. and Hemler M.E. 1998. Divalent cations and ligands induce conformational changes that are highly divergent among beta1 integrins. J. Biol. Chem., 273, 6670-6678

Bell G.I. 1978. Models for the specific adhesion of cells to cells. Science, 200, 618-627

Bhatnagar P.L., Gross E. P. and Krook M. 1954. A model for collision processes in gases. I. Small amplitude processes in charged and neutral one component systems, Phys. Rev., 94, 511-525

Blackshear P.L., Forstrom R.J., Dorman F.D. and Voss G.O. 1971. Effect of flow on cells near walls, Fed. Proc., 30, 1600-1611

Bongrand P. and Bell G. I. 1984. Cell-cell adhesion: parameters and possible mechanisms. In Cell Surface Dynamics: Concepts and Models. A. Perelson, C. DeLisi, F.W. Wiegel, Editor: Marcel Dekker, New York

Bouzidi M., Firdaouss M. and Lallemand P. 2001. Momentum transfer of a lattice Boltzmann fluid with boundaries. Phys. Fluids, 13, 11, 3452-3459.

Brunk D.K. and Hammer D.A. 1997. Quantifying rolling adhesion with a cell free assay: E-selectin and its carbohydrate ligands, Biophys. J., 72, 2820-2833

Butcher E.C. 1991. Leukocyte-endothelial cell recognition: three (or more) steps to specificity and diversity. Cell, 67, 1033-1036

Caputo K.E. and Hammer D.A. 2005. Effect of microvillus deformability on leukocyte adhesion explored using adhesive dynamics simulations, Biophys. J., 89, 187-200

Chang K.C. and Hammer D.A. 1996. Influence of direction and type of applied force on the detachment of macromolecularly-bound particles from surfaces, Langmuir, 12, 2271-2282.

Chang K.C., Tees D.F.J. and Hammer D.A., 2000. The state diagram for cell adhesion under flow: leukocyte rolling and firm adhesion. PNAS, 12, 2271-

2282

Chapman G.B. and Cokelet G.R. 1997. Model studies of leukocyte endothelium-blood interaction. Biorheology, 34, 37-56

Chen H., Chen S. and Matthaeus W.H. 1992. Recovery of the Navier-Stokes equation using a lattice-gas Boltzmann method, Phys. Rev. A. 45, R5339

Chen S., Chen H., Martinez D.O. and Matthaeus W.H. 1991. Lattice Boltzmann model for simulating of magnetohydrodynamics, Phys. Rev. Lett., 67, 3776.

Chen S. and Doolen G.D. 1998. Lattice Boltzmann method for fluid flows. Annu. Rev. Fluid Mech., 30, 329-364

Chen S., Martinez D. and Mei R.W. 1996. On boundary conditions in lattice Boltzmann method, Phys. Fluids, 8, 2527

Chesla S.E., Selvaraj P. and Zhu C. 1998. Measuring two-dimensional receptor-ligand binding kinetics by micropipette. Biophys. J., 75, 1553-1572

Chigaev A., Zwartz G., Graves S.W., Dwyer D.C., Tsuji H., Foutz T.D., Edwards B.S., Prossnitz E.R., Larson R.S. and Sklar L.A. 2003. $\alpha_4\beta_1$ integrin affinity changes govern cell adhesion. J. Biol. Chem., 278, 38174-38182

Cornubert R., d'Humi`eres D. and Levermore D. 1991. A Knudsen layer theory for lattice gases. Physica D, 47, 241-59

Darrell B. O'Quinn. 2005. The roles of leukocyte cell adhesion molecules in mucosal inflammation, Ph.D thesis, The University of Alabama at Birmingham

Dembo M., Torney D.C., Saxman K. and Hammer D.A. 1988. The reaction-

limited kinetics of membrane-to-surface adhesion and detachment, Proc. R. Soc. Lond. B. Biol. Sci., 234, 55-83

Diamond M.S. and Springer T.A. 1993. A subpopulation of Mac-1 (CD11b/CD18) molecules mediates neutrophil adhesion to ICAM-1 and fibrinogen. J. Cell Biol., 120, 545-556

Diamond M.S. and Springer T.A. 1994. The dynamic regulation of integrin adhesiveness. Curr. Biol., 4 (6), 506-517.

Dong C., Cao J., Struble E.J. and Lipowksy H.H. 1999. Mechanics of leukocyte deformation and adhesion to endothelium in shear flow, Ann. Biomed. Eng., 27, 298-312

Dong C., Slattery M. and Liang S.L. 2005. Micromechanics of tumor cell adhesion and migration under dynamic flow conditions, Frontiers in Bioscience, 10, 379-384.

Dransfield I., Cabanas C., Craig A. and Hogg N. 1992. Divalent cation regulation of the function of the leukocyte integrin LFA-1. J. Cell Biol., 116, 219-226.

Durlofsky L., Brady J.F. and Bossis G. 1987. Dynamic simulation of hydro-dynamically interacting particles, J. Fluid Mech., 180, 21

Dustin M.L. and Spring T.A., 1991, Role of lymphocyte adhesion receptors in transient interactions and cell locomotion. Annu. Rev. Immunol.,9, 27-66.

Filippova O. and Hänel D. 1997. Lattice-Boltzmann simulation of gas-particle flow in filters, Comput. Fluids. 26, 697

Frisch U., d'Humi´eres D., Hasslacher B., Lallemand P., Pomeau Y. and Rivet J.P.

1987. Lattice gas hydrodynamics in two and three dimensions, Complex Syst., 1, 649-707

Fu B.M. and Shen S. 2004. Acute VEGF effect on solute permeability of mammalian microvessels in vivo. Microvascular Research, 68, 51-62

Fu B. M., Adamson R.H. and Curry F.E. 2005. Determination of Microvessel Permeability and Tissue Diffusion Coefficient by Laser Scanning Confocal Microscopy, ASME J. Biomech. Eng., 127, 2, 270-278

Fu B.M. 2006. Microvessel permeability, Encyclopedia of Biomedical Engineering, Editor: Metin Akay, Wiley-Interscience, ISBN0-471-24967-X

Gallivan M.A., Noble D.R., Georgiadis J.G. and Buckius R.O. 1997. An evaluation of the Bounce-back boundary condition for lattice Boltzmann simulations, Int. J. Numer. Meth. Fluids, 25, 3, 249-263

Ginzbourg I. and Adler P.M. 1994. Boundary flow condition analysis for the three-dimensional lattice Boltzmann, model. J. Phys. II 4,191-214

Goldman A.J., Cox R.G. and Brenner H. 1967. Slow viscous motion of a sphere parallel to a plane wall-II Couette flow. Chem. Eng. Sci., 22, 653-660

Graver D.P. and Kute S.M. 1998. A theoretical study of the influence of fluid stresses on a cell adhering to a microchannel wall. Biophys. J., 75, 721-733.

Guo Z.L., Zheng C.G. and Shi B.C. 2002. An extrapolation method for boundary conditions in lattice Boltzmann method, Phys. of Fluids, 14, 2007-2010

Haier J. and Nicolson G.L. 2001. Tumor cell adhesion under hydrodynamic conditions of fluid flow, APMIS, 109, 241-262

Hammer D.A. and Apte S.M. 1992. Simulation of cell rolling and adhesion on surfaces in shear flow: general results and analysis of selectin-mediated neutrophil adhesion, Biophys. J., 63, 35-57

Hamaker H.C. 1937. The London-Van der Waals attraction between spherical particles, Physica, 4, 10, 1058-1072

He X.Y. and Luo L.S. 1997. Theory of the lattice Boltzmann method: From the Boltzmann equation to the lattice Boltzmann equation, Phys. Rev. E., 56, 6, 6811-5817

He X.Y. and Luo L.S. 1997. A priori derivation of the lattice Boltzmann equation, Phys. Rev. E., 55, Part A, R6333-R6336

He X. and Doolen G.D. 1997. Lattice Boltzmann method on curvilinear coordinates system: Flow around a circular cylinder, J. Comput. Phys., 134, 306-315

He P., Zeng M. and Curry F.E. 1998. cGMP modulates basal and activated micro-vessel permeability independent of $[Ca2+]_i$. American Journal of Physiology: Heart and Circulatory Physiology, 274, H1865-H1874

Hogg N., Harvey J., Cabanas C. and Landis R.C. 1993. Control of leukocyte integrin activation. Am. Rev. Respir. Dis., 148, S55-S59

Kaplanski G., Farnarier C., Tissot O., Pierres A., Benoliel A.M., Alessi M.C., Kaplanski S. and Bongrand P. 1993. Granulocyte-endothelium initial adhesion. Analysis of transient binding events mediated by E-selectin in a laminar shear flow, Biophys. J., 64, 1922-1933

King M.R. and Hammer D.A. 2001a. Multi-particle adhesive dynamics: Hydrodynamic recruitment of rolling leukocytes, PNAS, 98, 14919-14924.

King M.R. and Hammer D.A. 2001b. Multi-particle adhesive dynamics: Interactions between stably rolling cells, Biophys. J., 81, 799-813

Labadia M.E., Jeanfavre D.D., Caviness G.O., Morelock M.M., 1998. Molecular regulation of the interaction between leukocyte function-associated antigen-1 and soluble ICAM-1 by divalent metal cations. J. Immunol., 161, 836-842

Ladd A.C.J. 1994. Numerical simulation of particulate suspensions via a discretized Boltzmann equation: Part 1. Theoretical foundation, J. Fluid Mech., 271, 285-309

Ladd A.J.C. 1997. Sedimentation of homogeneous suspensions of non-Brownian spheres, Phys. Fluids, 9, 491-499

Lallemand P. and Luo L.S. 2003. Lattice Boltzmann method for moving boundaries. J. Comp. Phys., 184, 406-421

Lawrence M.B., Smith C.W., Eskin S.G. and McIntire L.V. 1990. Effect of venous shear stress on CD18-mediated neutrophil adhesion to cultured endothelium. Blood, 75, 227-237

Li H.B., Fang H.P., Lin Z.F., Xu S.X. and Chen Y.Y. 2004. Lattice Boltzmann simulation on particle suspensions in a two-dimensional symmetric stenotic artery. Phys. Rev. E, 69, 031919

Liu Q., Mirc D. and Fu B.M. 2008. Mechanical Mechanisms of Thrombosis in bent microvessels of rat mesentery. J. Biomech., 41, 12, 2726-2734

Lollo B.A., Chan K.W., Hanson E.M., Moy V.T. and Brian A.A., 1993. Direct evidence for two affinity states for lymphocyte functionassociated antigen 1 on activated T cells, J. Biol. Chem., 268, 21693-21700

Lomakina E.B. and Waugh R.E. 2004. Micromechanical Tests of Adhesion Dynamics between Neutrophils and Immobilized ICAM-1. Biophys. J., 86, 1223-1233

Lomakina E.B. and Waugh R.E. 2009. Adhesion between human neutrophils and immobilized endothelial ligand VCAM-1: divalent ion effects, Biophys. J., 96, 276-284

Lum A.F., Green C.E., Lee G.R., Staunton D.E. and Simon S.I. 2002. Dynamic regulation of LFA-1 activation and neutrophil arrest on intercellular adhesion molecule 1 (ICAM-1) in shear flow, J. Biol. Chem., 277, 20660-20670

Luscinskas F.W., Kansas G.S., Ding H., Pizcueta P., Schleiffenbaum B.E., Tedder T.F. and Gimbrone M.A. Jr. 1994. Monocyte rolling, arrest and spreading on IL-4-activated vascular endothelium under flow is mediated via sequential action of L-selectin, β_1-integrins, and β_2-integrins, J. Cell Biol., 125, 1417-1427

Lv Y., Zeng M., Pepe, A., Giancotti F. and Fu B.M. 2007. The Role of Integrin Beta4 Signaling in Mammary Tumor Cell Adhesion to Microvascular Wall in vivo, WACBE Congress on Bioengineering, Bangkok, Thailand

Marshall B.T., Long M., Piper J.W., Yago T., McEver R.P. and Zhu C. 2003. Direct observation of catch bonds involving cell-adhesion molecules, Nature,

423, 180-193

Marshall B.T., Sarangapani K.K., Lou J.Z., McEver R.P. and Zhu C. 2005. Force history dependence of receptor-ligand dissociation, Biophys. J., 88, 1458-1466

Marshall B.T., Sarangapani K.K., Wu J.H., Lawrence M.B., McEver R.P. and Zhu C. 2006. Measuring molecular elasticity by atomic force microscope cantilever fluctuations, Biophys. J., 90, 681-692

Masumoto A. and Hemler M.E. 1993. Mutation of putative divalent cation sites in the α_4 subunit of the integrin VLA-4: distinct effects on adhesion to CS1/fibronectin, VCAM-1, and invasion, J. Cell Biol., 123, 245-253

McNamara G.R. and Zametti G. 1988. Use of the Boltzmann equation to simulate lattice-gas automana, Phys. Rev. Lett., 61, 2332

Mei R.W., Luo L.S. and Shyy W. 1999. An accurate curved boundary treatment in the lattice Boltzmann method, J. Comput. Phys., 155, 307

Mei R.W., Yu D.Z., Wei S.Y. and Luo L.S. 2002. Force evaluation in the lattice Boltzmann method involving curved geometry, Phys. Rev. E., 65, 041203

Migliorini C., Qian Y.H., Chen H.D., Brown E.B., Jain R.K. and Munn L.L. 2002. Red blood cells augment leukocyte rolling in a virtual blood vessel, Biophys. J., 83, 1834-1841

Munn L.L., Melder R.J., and Jain R.K. 1996. Role of erythrocytes in leukocyte-endothelial interactions: mathematical model and experimental validation. Biophys. J., 71, 466-478

Noble D.R., Chen S., Georgiadis L.G. and Buckius R.O. 1995. A Consistent Hydrodynamic Boundary-Condition for the Lattice Boltzmann Method, Phys. Fluids, 7, 1, 203-209

Osborn L., Hession C., Tizard R., Vassallo C., Luhowskyj S., Chi-Rosso G. and Lobb R. 1989. Direct expression cloning of vascular cell adhesion molecule 1, a cytokine-induced endothelial protein that binds to lymphocytes, Cell, 59, 1203-1211

Pauli B.U. Augustinvoss H.G., Elsabban M.E., Johnson R.C. and Hammer D.A. 1990. Organ-preference of metastasis–the role of endothelial-cell adhesion molecules, Cancer and Metastasis Reviews, 9, 175-189

Qian Y.H. 1990. Lattice gas and lattice Kinetic theory applied to the Navier-Stokes equation, Ph.D thesis, Ecole Normale Superieure University de Paris

Qian Y. H., d' Humieres D. and Lallemand P. 1992. Lattice BGK models for Navier-Stokes equation, Europhys. Lett., 17, 479-484

Reinhardt P.H., Elliott J.F. and Kubes P. 1997. Neutrophils can adhere via $\alpha_4\beta_1$-integrin under flow conditions, Blood, 89, 3837-3846

Reinhardt P.H. and Kubes P. 1998. Differential leukocyte recruitment from whole blood via endothelial adhesion molecules under shear conditions. Blood, 92, 4691-4699

Rice G.E. and Bevilacqua M.P. 1989. An inducible endothelial-cell surface glycoprotein mediates melanoma adhesion, Science, 246, 1303-1306

Ruoslahti E., Noble, N.A., Kagami S. and Border W.A. 1994. Integrins. Kidney

Int., 45 (Suppl. 44), S17-S22

Segré G. and Silberberg A. 1961. Radial particle displacements in Poiseuille flow of suspensions, Nature, 189, 219

Shao J.Y. and Xu G. 2007. The adhesion between a microvillus-bearing cell and a ligand-coated substrate: a Monte Carlo study, Annals of Biomedical Engineering, 35, 397-407

Shen S., Fan J., Cai B., Lv Y., Zeng M., Hao Y., Giancotti F. and Fu B.M. 2010. "Vascular Endothelial Growth Factor Enhances Mammary Cancer Cell Adhesion to Endothelium in vivo, J. Exp. Physiology, 95, 369-379

Skalak R. and Chien S. 1987. Handbook of Bioengineering. McGraw-Hill, New York

Springer T.A. 1994. Traffic signals for lymphocyte recirculation and leukocyte emigration: the multistep paradigm. Cell, 76, 301-314

Sun C.H., Migliorini C. and Munn L.L. 2003. Red blood cells initiate leukocyte rolling in postcapillary expansions: A lattice Boltzmann analysis, Biophys. J., 85, 208-222

Sun C.H. and Munn L.L. 2006. Influence of erythrocyte aggregation on leukocyte margination in postcapillary expansions: A lattice Boltzmann analysis, Physica A, 362, 191-196.

Wang J.K., Slattery M.J., Hoskins M.H., Liang S.L., Dong C. and Du Q. 2006. Monte Carlo simulation of heterotypic cell aggregation in nonlinear shear flow, Mathematical Biosciences and Engineering, 3, 683-696

Waugh R.E. and Lomakina E.B. 2009. Active site formation, not bond kinetics, limits adhesion rate between human neutrophils and immobilized vascular cell adhesion molecule 1, Biophsy. J., 96, 268-275

Weiss L. 1990. Matastatic inefficiency, Advanced Cancer Research, 54, 159-211

Weiss L. 1992. Biomechanical interactions of cancer-cells with the microvasculature during hematogenous metastasis, Cancer Metastasis Rev., 11, 227-235

Woodside D.G., Liu S. and Ginsberg M.H. 2001. Integrin Activation. Thromb. Haemost., 86, 316-323

Yan W.W., Liu Y. and Fu B.M. 2010a. Effects of curvature and cell-cell interaction on cell adhesion in micro-vessels. Biomech. Model. Mechanobiol., 9 (5), 629-640

Yan W.W., Liu Y. and Fu B.M. 2010b. Effect of wall shear stress gradient on cell adhesion in curved micro-vessels, Biomech. Model. Mechanobiol., submitted

Yednock T.A., Cannon C., Vandevert C., Goldbach E.G., Shaw G., Ellis D.K., Liaw C., Fritz C.L. and Tabber L.I. 1995. $\alpha_4\beta_1$ integrin-dependent cell adhesion is regulated by a low affinity receptor pool that is conformationally responsive to ligand. J. Biol. Chem., 270, 28740-28750

Yuan X.F. and Ball R.C. 1994. Rheology of hydrodynamically interacting concentrated hard disks, J. Chem. Phys., 101, 9016

Zhang X., Craig S.E., Kirby H., Humphries M.J. and Moy. V.T. 2004. Molecular basis for the dynamic strength of the integrin $\alpha_4\beta_1$ /VCAM-1 interaction,

Biophys. J., 87, 3470-3478

Ziegler D.P. 1993. Boundary conditions for lattice Boltzmann simulations. J. Stat. Phys., 71, 1171-1177

Zhu C. 2000. Kinetics and mechanics of cell adhesion, J. Biomech., 33, 23-33.

Zhu C., Bao G. and Wang N. 2000. Cell mechanics: Mechanical response, cell adhesion, and molecular deformation, Annu. Rev. Biomed. Eng., 2, 189-226

Zou Q.S. and He X.Y. 1997. On pressure and velocity boundary conditions for the lattice Boltzmann BGK model, Phys. Fluids, 9, 1591-1598